A PHOTOMETRIC MODEL OF THE INCLINED F RING OF SATURN

A Dissertation

Presented to the Faculty of the Graduate School

of Cornell University

in Partial Fulfillment of the Requirements for the Degree of

Doctor of Philosophy

by

Britt Rebecca Scharringhausen

January 2007

A PHOTOMETRIC MODEL OF THE INCLINED F RING OF SATURN

Britt Rebecca Scharringhausen, Ph.D.

Cornell University 2007

Observations by Hubble Space Telescope (HST) of the rings of Saturn during the 1995 ring-plane crossing revealed a surprising asymmetry in the brightness of the east and west ansae. As in historical observations, the ring brightness was nonzero at the time that the rings are observed edge-on. We create a photometric model of the ring system with the F ring inclined to the main ring plane which reproduces the observed brightness of the rings and the asymmetry in ring brightness after the ring-plane crossing.

The F ring is modeled as "ribbon" 60 km tall, of indeterminate radial width, with a gaussian profile of optical depth as a function of height with an equivalent depth of D=10±4 km and a full width at half maximum of 13±7 km. This is the first estimate of the physical vertical thickness of the F ring, which we find is $\sim 10^3$ times greater than the main ring thickness.

The model shows that as the Earth crosses the main ring plane, the F ring dominates the brightness of the system, and that the asymmetry in ring brightness after the ring-plane crossing is caused by asymmetric absorption of light from the main rings by the front of the F ring.

The model gives post-crossing asymmetries in good agreement with the HST data, but fails to reproduce the small asymmetries in ring brightness observed before the ring-plane crossing. The model profiles of ring brightness plotted vs.

horizontal distance from the center of Saturn show many of the features observed in the HST profiles. However, the F ring in this model is longitudinally symmetric, and does not include the many clumps or arcs that have been observed in the real F ring. It therefore cannot reproduce many of the small-scale variations seen in the HST profiles. It may be that these small features are responsible for the asymmetries observed before the ring-plane crossing.

BIOGRAPHICAL SKETCH

Britt Scharringhausen was born in Dubuque, Iowa on June 22, 1974, and raised by her parents, Ernst and Julie Scharringhausen, along with her sister, Gretchen. She attended the University of Iowa in Iowa City, Iowa, which is where she met her husband-to-be, Jason Dettman. She earned a BS in Physics and Astronomy in 1996 and came to Ithaca, New York to attend graduate school in the Department of Astronomy at Cornell University, pursuing research in rings and satellites of Saturn. She and Jason were married on June 19, 1999. In the Spring of 2003, she was given the opportunity to teach physics and astronomy in the Department of Physics at Ithaca College, and taught there through the Spring of 2006.

In the Fall of 2006, she moved to Beloit, Wisconsin to join the faculty of the Beloit College Department of Physics and Astronomy.

For J.

ACKNOWLEDGMENTS

The NASA Planetary Data System Rings Node was indispensable in this research, and special thanks are due to Mitch Gordon for help with the 28 Sgr occultation datasets. The NASA Astrophysics Database System Bibliographic Services were also used extensively in the preparation of this document. This document was prepared using the `cornell` document class for LaTeX 2_ε, which worked like a dream, and I am indebted to those who created and maintained this extemely useful tool. Thanks to Howard Sanders, Matthew Hedman and Matthew Tiscareno for reviewing passages. Thank you to my committee for their helpful comments.

I am also thankful to my parents and grandparents for getting me here, and to Profs. Mutel, Rodgers, Spangler, and Molnar of the University of Iowa. Thanks also to my fellow Cornell grad students, an extraordinary group of people who I will never forget. My deepest gratitude is due to my colleagues at the Department of Physics at Ithaca College for their advice, support and good cheer. I must also give special thanks to Beth Clark-Joseph, my mentor, for encouraging me to find my way forward.

For keeping me sane, I am grateful to my husband, the Kung Fu Justice Squad, the Cornell Society for Strategic Simulations and the CSSS Ladies' Knitting Auxiliary.

TABLE OF CONTENTS

LIST OF FIGURES

LIST OF TABLES

Chapter 1

Introduction

The Sun crosses the ring-plane of Saturn during the equinoxes of Saturn. Since the orbital period of Saturn is 29.4 years, this occurs about every 15 years. Saturn's semimajor axis is 9.58 AU, and its mean orbital speed is 9.69 km/s, compared to 29.8 km/s for the Earth. As Saturn's ring plane sweeps through the inner Solar System, Earth's orbital motion carries it from one side of Saturn's ring plane to the other. Each passage of the Earth or the Sun across the ring plane, and a set of crossings collectively, are referred to as a ring-plane crossing or RPX, for short. In each RPX, which takes less than 12 months, there is one solar RPX. In about half of RPXs the Earth crosses the ring plane three times, and in the other half there is only one Earth ring-plane crossing.

Ring-plane crossings present some unusual opportunities for observing the saturnian system. As the Earth crosses the ring-plane, Earth-based observers are able to see the rings edge-on. The main rings are greatly reduced in brightness, allowing observations of faint moons that are usually lost in scattered light from the rings. Also, during two periods in the sequence of triple Earth ring-plane crossings, the Earth and Sun are on opposite sides of the ring-plane, allowing the dark side of the rings to be observed, rather than the lit side which is usually visible to Earth.

Historically, an Earth RPX has been seen as an opportunity to measure the vertical thickness of the rings as they are seen edge-on. It is impossible to directly measure the physical thickness of the rings from Earth during an RPX. The projected height of the rings on the sky is small enough that the rings are vertically unresolved for weeks before and after the ring-plane crossing. However,

observers have measured the brightness of the rings, expressed as a *photometric thickness*, and used radiative transfer theory to interpret this to determine the physical thickness of the rings.

The earliest estimate comes from William Herschel, who observed the RPX of 1789, and determined that the rings were no more than 500 km thick. Unaware of the transparency of some ring regions, William and George Bond assumed that the nonzero brightness of the rings on the dark side was due to light reflected from the edge of the rings, and estimated their thickness as 60 km based on data from the RPX of 1848–1849. When astronomers realized that much of the brightness of the dark side rings was due to light transmitted through optically thinner regions of the rings, such as the C ring, they turned to measuring the residual brightness of the rings at the moment of the RPX to determine the rings' thickness. Henry Norris Russell used the observations of E. E. Barnard at the 12-inch refractor at Lick Observatory in 1889 to further constrain the thickness of the rings to 21 km (Alexander, 1962).

In the modern age, more precise measurements of the vertical photometric thickness of the rings have been made using photographic plates, electronographic cameras, and, for the 1995 RPX, CCDs. These have revised the photometric thickness down to just a few kilometers. (See Section 3.1.1 for details.)

These measurements, however, are at odds with measurements of the physical thickness of the rings from the Voyager missions. A stellar occultation observed by Voyager 2 places an upper limit of 200 m on the thickness of the main rings (Lane et al., 1982) while a radio occultation of Voyager 1 implies a thickness of only a few tens of meters (Zebker and Tyler, 1984). Dynamical models of the behavior of ring particles also tend to favor this smaller estimate (e.g. Esposito et al. (1984); Cuzzi

et al. (1979a,b)), with some suggesting that the rings may consist of a monolayer or near-monolayer of particles (Goldreich and Tremaine, 1978; Salo and Karjalainen, 2003).

Profiles of the brightness of the rings during the Earth RPX of 10–11 August 1995 show that, near RPX, the ring brightness is relatively constant with distance from Saturn, dropping sharply not at the edge of the A ring (136,800 km), but rather at the F ring (140,200 km), showing that the F ring dominates the edge-on thickness. HST images of the dark side of the rings in November 1995 reveal that the brightness of the rings on the dark side is due to sunlight transmitted through the C ring, the Cassini Division, and also the F ring. These images also show the F ring disappearing into the main rings' shadow, demonstrating that it is inclined to the main ring plane (Bosh et al., 2002; Nicholson et al., 1996).

The most surprising result from the HST observations, though, was an asymmetry in brightness between the east and west ansae observed within a few hours of the RPX. Asymmetries had been reported in some historical observations, but this is the first modern, precise measurement of this phenomenon. Because of its inclination, the F ring was suspected of playing a role in these asymmetries.

Since its discovery in 1979, the F ring of Saturn has attracted a share of attention disproportionate to its small mass, its narrow width, and its usually dim contribution to the brightness of Saturn's ring system. Found just outside the A ring, the F ring has a radial extent of only a few hundred kilometers, but within those narrow confines its structure is complex, stranded, kinked and braided (Smith et al., 1981, 1982). The F ring's appearance not only varies with longitude, but also with time, as mysterious clumps appear and disappear in and near the F ring over periods of weeks and months (Showalter, 2004; McGhee et al., 2001).

The moons Prometheus and Pandora, orbiting just inside and outside the F ring, respectively, are the prototypical "shepherd moons," pairs of moons which confine narrow rings through gravitational interactions. This phenomenon is also observed in the ring systems of Uranus and Neptune. However, Showalter and Burns (1982) questioned whether Pandora and Prometheus actually serve to confine the F ring. As the system was studied more extensively, there was little evidence that shepherding played an important role in shaping the F ring. Indeed, it seems that Prometheus is more of a disruptive influence on the F ring system. Images from the Cassini spacecraft show that when Prometheus is near the apoapse of its eccentric orbit, its close proximity to the F ring allows it to pull material from the F ring, creating structures called "channels" and disrupting the structure of the strands (Murray et al., 2005).

The origins of the strands of the F ring are more obscure. It has been proposed that the F ring consists mainly of large ($\sim$100 m) moonlets that are themselves difficult to detect, but a very large meteoroid impact on one of these bodies, or even mutual collisions between the bodies themselves, could liberate enough regolith to form the visible F ring (Cuzzi and Burns, 1988). It is thought that smaller meteoroid collisions (Showalter, 1998) and mutual collisions between moonlets are responsible for the appearance of temporary clumps and arcs in the F ring, as well (Showalter, 2004; Barbara and Esposito, 2002; Poulet et al., 2000b). Over time, smaller particles are lost from the ring because of drag forces due to radiation and electromagnetic effects, but much of the debris would be expected to reaccrete onto the large parent bodies.

The fact that the F ring is just outside the Roche limit for icy bodies makes it an ideal laboratory for the study of accretion and collisional disruption, potentially

shedding light not only on the formation of rings and satellites in our Solar System, but on the process of planetary formation in general.

In the current work, we use HST observations of Saturn's ring system, seen edge-on as the Earth crossed the ring plane in August 1995, to probe the vertical structure of the F ring for the first time. Because mutual collisions between parent bodies in the F ring and meteoroid collisions seem to be an important process, and because these should impart vertical as well as radial velocities to ring particles, a characterization of the ring's vertical thickness provides a useful constraint on the processes that drive the F ring's evolution. In addition, putative large parent bodies in the F ring's core may scatter other particles vertically, so that the thickness may put limits on a population of large parent bodies in the ring.

We will begin this thesis with a discussion of I/F, a quantity expressing the brightness of the rings as a reflectivity. Chapter 2 is intended to synthesize the definition and common uses of I/F, particularly by the rings community, and thus to serve as an introduction to the subject for novices, or as a reference.

Chapter 3 picks up where this Introduction leaves off to provide a more in-depth survey of modern observations of Saturn ring-plane crossings and of the F ring. The HST observations are discussed in detail in Section 3.1.2, and we present previously unpublished profiles of the brightness of the rings as a function of horizontal distance from the center of Saturn. The only previous photometric model of the F ring, by Poulet et al. (2000a), is discussed in Section 3.3.

We detail the construction of the present model in Chapter 4, including the geometry and photometric parameters of the main rings and the F ring.

The results of the model are presented and compared with the HST data in Chapter 5.

In Appendix A, we give a detailed description of the calculation of the brightness of saturnshine, sunlight scattered off the planet onto the rings. Although we find that saturnshine is negligible compared to sunlight directly scattered by the rings in the 10 August 1995 geometry, we demonstrate that it is the source of the asymmetry in brightness between the east and west ansae observed on 21 November 1995.

In Appendix B, we evaluate the effect of changing the F-ring orbital elements used to determine the geometry of the model. We confirm that the orbit determined by Bosh et al. (2002) is consistent with the observed asymmetries, but find that the RPX data do not have the sensitivity required to further refine the measurement of the F ring's ascending node and inclination.

Chapter 2

An I/F Primer

In planetary astronomy, and particularly within the planetary rings community, it is common to express reflectance in terms of I/F. The subtleties of this quantity confound and bedevil both beginners and expert photometrists alike. This chapter is intended to review the definition of I/F and some related quantities, examine some of I/F's applications, and contribute to an intuitive understanding of I/F in some common situations.

2.1 The Definition of I/F

Understanding the definition of I/F, we must first understand intensity and flux. We will attempt, not only to provide a lucid introduction to the basic concepts of flux and intensity, for the beginner, but also to clarify some common variations in the definitions of these quantities that can so easily lead to confusion.

2.1.1 Flux and Intensity

For most who approach the study of photometry, radiant flux is a familiar quantity. The net radiant flux, $\mathcal{F}$, is defined by the following expression:

$$dE = \mathcal{F} dA dt. \tag{2.1}$$

dE is the energy per unit area per unit time that crosses some surface of area dA in a time dt.

Intensity can be more difficult than flux to understand intuitively. Intensity is the amount of energy per unit area per unit solid angle passing through a surface

in a certain direction. The surface could be the physical surface of a planet, the boundary between two different layers within a star, a detector such as a CCD chip, or any imaginary surface you choose to define.

There are two important differences between flux and intensity. One is that intensity is defined per unit solid angle. Another is that intensity is directional. The total emitted flux is the energy emitted by a source in *all* directions, over all angles θ and also all azimuthal angles, ϕ, while emitted intensity is only the energy that travels in a certain direction away from the source. Consider some small area element dA of a source. To specify a direction, we choose a "radiation pencil" which is oriented at some angle θ to the normal of dA and has a size given by the solid angle $d\Omega$. The term "pencil" serves to indicate that we have selected a very narrow solid angle, infinitesimal, chosen so that intensity in the cone is uniform, and the rays of light in the cone are essentially parallel to one another. The solid angle, $d\Omega$, describes the size of some other area element, as seen from the position of the area element where we are calculating the intensity. For example, we may wish to know how much light from the Sun will fall on a moon. In that case, dA could be an area element of the moon, and $d\Omega$ will specify the angular size of Sun as seen from the moon. Alternately, $d\Omega$ could give the angular size of a region of the moon as seen from the Sun, and dA could be the size of the Sun.

The intensity, $I(\theta)$, describes the energy dE passing through an dA_n perpendicular to the ray and within a solid angle $d\Omega$ in a time dt:

$$dE = I(\theta, \phi, t) dA_n d\Omega dt \tag{2.2}$$

$$= I(\theta, \phi, t) \cos\theta dA d\Omega dt. \tag{2.3}$$

Note that, unlike flux, the area required is the *projected* area measured with respect to the normal of the ray. For surfaces that are not perpendicular to the direction

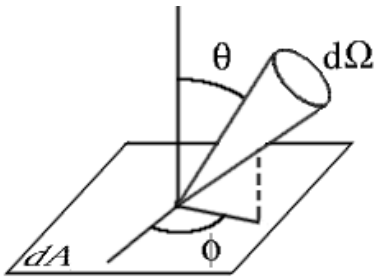

Figure 2.1: Geometry for radiation pencil $d\Omega$ incident upon, or emanating from, a surface element of area dA at an angle of θ to a normal to the surface.

of the light's travel, as in Fig. 2.1, if the ray is oriented at an angle θ to the normal of a surface with area dA, then the projected area is:

$$dA_n = \cos\theta dA = \mu dA, \tag{2.4}$$

where we have written the direction cosine, $\cos\theta$, as μ.

By combining Eqs. 2.1 and 2.3 we find that the relationship between intensity and net flux is

$$\mathcal{F} = \int I\mu d\Omega, \tag{2.5}$$

where the integral is taken over all angles.

As a simple example, let us calculate the flux from a Lambert surface, which scatters all the light incident on the surface equally at all angles. A sheet of white paper is a common example. The reflected intensity of the surface is $I(\theta) = I$ where I is a constant. To find the reflected flux we integrate over all angles into which light is scattered, i.e., all angles above the surface:

$$\mathcal{F} = I\int \cos\theta d\Omega \tag{2.6}$$

$$= I\int_0^{2\pi}\int_0^{\pi/2} \cos\theta\sin\theta d\theta d\phi \tag{2.7}$$

$$= \pi I \tag{2.8}$$

$$I = \mathcal{F}/\pi. \tag{2.9}$$

Now consider how the light travels through space. The received flux is the amount of energy received per unit time per unit area normal to the ray from a source. Conservation of energy and the definition of flux in Eq. 2.1 show that the received flux follows an inverse square law. Consider a constant isotropic source of light that is surrounded by two spherical surfaces, each centered on the source, with radii r_1 and r_2 . As the source emits light, the same amount of energy must pass through each surface in a given time dt:

$$E_1 = E_2 \tag{2.10}$$

$$\mathcal{F}_1 4\pi r_1^2 dt = \mathcal{F}_2 4\pi r_2^2 dt \tag{2.11}$$

$$\frac{\mathcal{F}_1}{\mathcal{F}_2} = \frac{r_2^2}{r_1^2}. \tag{2.12}$$

Intensity, by contrast, is constant as long as light travels through a vacuum, no matter the distance from the source. The dependence of the flux on the square of the distance is canceled by the fact that intensity is defined per unit solid angle, since the solid angle of the source or the receiver is also dependent on the distance squared: $d\Omega = A/r^2$.

To picture this, consider the intensity emitted from some source. The "point" of the radiation pencil is located at the source. As the distance from the source increases, intuitively we might expect the intensity to decrease as the rays diverge. However, this is a matter of confusing flux with intensity. As the distance from the source increases, the solid angle $d\Omega$ (remaining constant itself), encompasses a greater and greater area, and the flux decreases at the same rate, so the amount of energy passing through the radiation pencil is the same at any distance from

the source. In other words, although the rays diverge, no rays leave the radiation pencil.

Conversely, consider the intensity received from a source. In this case, we are interested in energy arriving along a radiation pencil whose point is located at the receiver. The greater the distance to the source, the larger the surface area of the source that is covered by the end of the pencil, and thus the larger the power emitted into the pencil. (Remember that we can always choose the solid angle of the pencil $d\Omega$ to be small enough that it covers a uniform region of the source, or else we can take into account that the end of the pencil is averaging over a certain area of the source.)

Thus we have the somewhat startling result that we do not need to make a distinction between the emitted intensity and the received intensity. The invariability of intensity as light travels through a vacuum can be shown analytically by considering the intensity of a ray of light that passes through two area elements dA_1 and dA_2 which are both perpendicular to the ray and separated by a distance of r. Let the intensity of the ray as it passes through dA_1 be I_1, and the intensity of the ray as it passes through dA_2 be I_2. We shall choose the size of the elements so that all the light that passes through dA_1 also passes through dA_2, i.e., $dE_1 = dE_2$. Using the definition of intensity from Eq.2.3:

$$I_1 dA_1 d\Omega_1 dt = I_2 dA_2 d\Omega_2 dt. \tag{2.13}$$

Consider the solid angles carefully. $d\Omega_1$ is the angle into which dA_1 emits light. All this light passes through dA_2, so $d\Omega_1 = dA_2/r^2$. Similarly, to account for all of the light striking dA_2, we must be sure to include the light coming from dA_1, so

$d\Omega_2 = dA_1/r^2$. Substituting these solid angles into Eq. 2.13:

$$I_1 dA_1 \frac{dA_2}{r^2} dt = I_2 dA_2 \frac{dA_1}{r^2} dt. \tag{2.14}$$

Thus $I_1 = I_2$. The received intensity is the same as the emitted intensity.

2.1.2 Optical Depth

As light passes through a medium, rather than empty space, the intensity is not constant, because some of the radiation can be scattered out of the ray or absorbed by the medium. The mass absorption coefficient, κ, characterizes the rate at which energy that is lost from the ray.

If light of intensity I travels a distance ds through a medium and penetrates to a depth dz, and its path makes an angle θ with a normal to the surface of the medium, then the pathlength traveled through the medium is $ds = dz/\mu$ where $\mu = cos\theta$. Note that here we define μ to always be positive, whether the light is traveling upward or downward. If the light propagates through a uniform medium with mass absorption coefficient κ and mass density ρ, the light loses intensity at the rate

$$\frac{dI}{ds} = -\kappa\rho I, \tag{2.15}$$

or

$$dI \frac{\mu}{dz} = -\kappa\rho I. \tag{2.16}$$

If we integrate from the point where the ray enters the medium ($z = 0$) to a depth z,

$$\int_0^z \frac{dI}{I} = -\int_0^z \kappa\rho \frac{dz}{\mu}, \tag{2.17}$$

and thus

$$I(z) = I(0)e^{-\tau(z)/\mu}, \tag{2.18}$$

where

$$\tau(z) = \int_0^z \kappa\rho dz \tag{2.19}$$

is the normal optical depth, a dimensionless measure of opacity. As we move to increasing physical depth, z, the optical depth τ also increases.

We have defined the optical depth along a normal to the surface, but it is sometimes defined as the optical depth along the ray. See, for example, Eq. 1.50 of Chandrasekhar (1960), who also refers to optical depth as optical thickness. The two terms are interchangeable, though *optical depth* is preferred in the ring literature.

If $\tau \ll 1$ the medium is said to be optically thin. When looking at a thicker medium, we generally see down to an optical depth of $\tau \sim 1$, so when we look at light scattered by a slab with $\tau \gg 1$, the exact value of τ becomes irrelevant because most of the light is scattered or absorbed before reaching the lower levels, and the system is said to be optically thick. In this case, it is difficult to measure the true optical depth of the medium using scattered light alone.

Equivalent Depth of Narrow Rings

The F ring's optical depth has been measured in several stellar occultations. (See section 3.2.2 for details.) As the star's path passes behind the ring, the occultation probes the profile of the optical depth of the F ring. These occultations show many different shapes for the radial variation in the optical depth and also vary in their resolution. In order to compare the results of different occultations, Showalter et al. (1992) define an equivalent depth:

$$\mathrm{D} = \int \tau(a) da, \tag{2.20}$$

where a is the true radial distance from Saturn as measured in the ring plane and the integral is taken over the entire radial extent of the ring. Note that unlike optical depth, equivalent depth has units of length.

Let us consider what happens when we measure the optical depth of a ring from two different points of view. Let the ring extend radially in the ring plane from $a = r_0$ to $a = r_1$, a distance z_0 above and below the ring plane. Let the ring's absorption coefficient be described by some function $\kappa(a, z)$, while its mass density is $\rho(a, z)$.

We will begin by looking straight down onto the ring and measuring the brightness of the source as it passes behind the ring from our point of view. We can measure the attenuation of the object's intensity as given by Eq 2.18, and find the a vertical optical depth τ_v which is a function of radius, a. According to Eq. 2.19:

$$\tau_v(a) = \int_{-z_0}^{z_0} \kappa(a, z)\rho(a, z)dz. \tag{2.21}$$

We refer to this as the radial profile of the ring's optical depth. If we wish to know the equivalent depth of the ring, we use Eq. 2.20 and integrate over our radial profile of optical depth:

$$\mathrm{D} = \int_{a_0}^{a_1} \tau_v(a)da, \tag{2.22}$$

or, substituting the expression for τ_v in Eq. 2.21:

$$\mathrm{D} = \int_{a_0}^{a_1} \int_{-z_0}^{z_0} \kappa(a, z)\rho(a, z)dzda. \tag{2.23}$$

Note that if the ring's mass absorption coefficient is uniform (i.e., it is made of the same material throughout) then D is just

$$\mathrm{D} = \kappa \int_{a_0}^{a_1} \int_{-z_0}^{z_0} \rho(a, z)dzda \tag{2.24}$$

$$= \kappa\sigma, \tag{2.25}$$

where σ is the total mass per unit arc length of the ring.

Now, let us look radially inward at the ring from a position in the ring plane, and measure the decrease in intensity of some other source that passes behind the rings in order to measure the radial optical depth, $\tau_r(z)$ instead. If we integrate along the line of sight to the star, which is now radial,

$$\tau_r(z) = \int_{a_0}^{a_1} \kappa(a,z)\rho(a,z)da. \tag{2.26}$$

Let us now integrate over this vertical profile of optical depth in order to calculate the vertical analog to equivalent depth:

$$\mathrm{D}' = \int_{-z_0}^{z_0} \tau_r(z)dz. \tag{2.27}$$

But when we substitute using Eq. 2.26, we find:

$$\mathrm{D}' = \int_{-z_0}^{z_0}\int_{a_0}^{a_1} \kappa(a,z)\rho(a,z)dadz = \mathrm{D}. \tag{2.28}$$

We can see that these equivalent depth measurements are directly comparable. If κ is again uniform, then, just as with the vertical optical depth profile,

$$\mathrm{D}' = \kappa \int_{-z_0}^{z_0}\int_{a_0}^{a_1} \rho(a,z)dzda \tag{2.29}$$

$$= \kappa\sigma. \tag{2.30}$$

If the ring is optically thick (i.e., $\tau/\mu \gg 1$) then when we attempt to measure the attenuated intensity, we will simply find that I approaches 0, and we will only be able to determine a lower limit for τ, and thus D, based on the limit of sensitivity of our detector.

On the other hand, if in all our observations the ring is optically thin (i.e., $\tau/\mu < 1$), when we measure the optical depth profile, we will always be able to measure some intensity and can calculate the true value of τ. Whenever we are looking at the same piece of ring, we will calculate the same D whether we view the ring from above, or the side, or any intermediate angle.

2.1.3 Redefining Flux

As described in 2.1.1, flux is the energy per unit area per unit time that crosses some area element. However, there are two ways to define the flux. In Eq. 2.1, the flux was the total energy crossing an area dA, regardless of the direction that the light travels. This definition is commonly used when the light we are interested in is traveling in all directions, such as light emitted by a blackbody surface.

As we study the scattering properties of different media, though, we are primarily interested in light that is traveling in a specific direction, e.g., sunlight incident in parallel rays on the rings or the surface of a planet, or light scattered toward a specific observer. In this case, the flux is still defined as the energy per unit time per unit area crossing some area element, but the element is defined to be perpendicular to the ray of light, denoted by dA_n, as in the definition of the intensity.

In this work, flux defined relative to an area dA of any orientation will always be represented by $\mathcal{F}$, while the flux defined relative to an area dA_n normal to the ray as πF, but this is not a standard convention, and indeed some authors may use the same symbol for both fluxes, and use different definitions in different contexts. The inclusion of the factor of π follows the convention of Chandrasekhar (1960). Other authors define the flux without this factor of π. Because of these variations, when using measurements of flux or expressions involving flux taken from different resources, care should always be taken to understand the definition of flux in each context.

2.1.4 Reflectance

The reflectance, I/F, is the intensity of sunlight scattered by a medium divided by F, where the flux of incident sunlight normal to the ray is πF. In the definition I/F, the incident flux is always measured normal to the ray and the factor of π is always included.

When working with I/F, F is essentially a scaling factor. The important part is I, which is what is measured by a detector. I/F behaves like an intensity and it is best to think of it as such.

Dividing by the flux of incident sunlight simplifies the interpretation and analysis of observations by removing from consideration the varying distance from the Sun to the object. Dividing by F also removes the solar spectrum, which is useful when comparing observed spectra to laboratory spectra or when observing at different wavelengths.

A useful standard for comparison of measured reflectance is the Lambert scatterer introduced in Section 2.1.1. Consider a surface of area A upon which a flux πF is incident with an incidence cosine $\mu_0 = \cos i$, where i is the angle at which light is incident on the surface, measured from the normal to the surface. The power received per unit time by the surface, according to Eq. 2.1, is

$$L = \frac{dE}{dt} = \pi F \mu_0 A. \tag{2.31}$$

The emitted power must be equal, because a Lambert surface will scatter *all* the incident radiation. Because a Lambert surface scatters equal intensity in all directions, $I(\epsilon) = I$. The scattered power is found by integrating Eq. 2.3 over the hemisphere into which light is scattered from the surface:

$$L = I \int_0^{2\pi} \int_0^{\pi/2} \mu A \sin\epsilon d\epsilon d\phi. \tag{2.32}$$

Notice that in Eq. 2.31,

$$A_n = \mu A = \cos i A, \tag{2.33}$$

because the area element required is projected area, perpendicular to the ray. This can also be thought of as the area seen by the emitter. In Eq. 2.32,

$$A_n = \mu A = \cos \epsilon A \tag{2.34}$$

is the projected as seen by the recipient of the radiation, i.e., an observer located at some angle ϵ from the normal to the area element A.

Integrating:

$$L = \pi I A, \tag{2.35}$$

and since the received power must equal the scattered power, we can set Eq. 2.31 equal to Eq. 2.35:

$$I = F \mu_0, \tag{2.36}$$

so the I/F of the Lambert surface is simply

$$\text{I/F} = \mu_0. \tag{2.37}$$

Imagine that we are viewing a Lambert surface, such as a sheet of white paper, illuminated by the Sun. If the surface is held at a fixed angle to the incoming sunlight, then no matter where we move to, its I/F will remain the same and the sheet will have the same brightness, because the emission cosine is irrelevant. However, the incidence cosine is still important because the greater the incidence angle of the sunlight, the greater the area the incident sunlight is spread over, so if we change the orientation of the paper relative to the Sun, its reflected brightness will change.

2.2 Single Scattering

When modeling radiative transfer through a diffuse medium, it is a common approximation to assume that each photon encounters at most one particle before leaving the medium, i.e. that the medium is single-scattering.

2.2.1 Equations of Radiative Transfer for Single Scattering

As we saw in Section 2.1.2, light traveling through a medium can be absorbed and scattered. Chandrasekhar (1960) derives the intensity of light scattered by a diffuse, plane-parallel single-scattering medium.

We will refer to light scattered toward an observer on the same side of the plane as the source of illumination as *reflected light*. The expression for the I/F of singly scattered reflected light is:

$$\mathrm{I/F} = \frac{1}{4} P(\alpha) \varpi_0 \frac{\mu_0}{\mu + \mu_0} \left(1 - e^{-\tau(1/\mu + 1/\mu_0)}\right). \tag{2.38}$$

while the light transmitted through the medium to an observer on the opposite side from the illumination source is given by:

$$\mathrm{I/F} = \frac{1}{4} P(\alpha) \varpi_0 \frac{\mu_0}{\mu - \mu_0} \left(e^{-\tau/\mu} - e^{-\tau/\mu_0}\right). \tag{2.39}$$

Again, πF is the incident flux, and τ is the normal optical depth of the medium. ϖ_0 is the single-scattering albedo, the fraction of the incident light that a single ring-particle scatters in all directions. The phase angle, α, is the angle between the direction of the source of the light and the direction to the observer as seen by the scattering particle. The phase function, $P(\alpha)$, describes how the intensity of the scattered light varies with the phase angle. The phase function is normalized so that $\int P(\alpha) d\Omega = 4\pi$. For an isotropic scatterer, $P(\alpha) = 1$.

Chandrasekhar (1960) includes the phase function in the definition of the albedo for single scattering, $\varpi_0(\alpha)$. However, most authors separate the phase function from the single-scattering albedo, which is then independent of the phase angle. We have followed the latter convention by writing the two factors explicitly as $\varpi_0 \cdot P(\alpha)$.

The incidence cosine is $\mu_0 = \cos(i)$, where i is the incidence angle, the angle between the incoming light ray and the normal to the medium's surface. If ϵ is the emission angle, the angle between the normal to the surface and the direction of the observer, then $\mu = \cos(\epsilon)$. Because i and ϵ are always taken to be between 0 and 90°, μ_0 and μ are always between 0 and 1. (Other conventions are possible. For example, Cooke (1991) defines $\mu < 0$ for transmitted light.)

The labeling conventions for the direction cosines for incident and scattered light vary. For example, some (e.g., Poulet et al. (2000a)) use μ' for the incident light and μ for the scattered light. When working with ring ephemerides, it's useful to note that for a flat ring observed from Earth, $\mu_0 = |\sin B_s|$ and $\mu = |\sin B_e|$, where B_s and B_e are the ring-opening angles to the Sun and Earth, respectively. This is because B_s is the angle of the Sun above or below the ring plane, and for a flat ring i is the angle from the normal of the ring plane for incoming light from the Sun. Similarly, B_e and ϵ are also complementary angles.

2.2.2 Limiting Cases

It is notoriously difficult to develop an intuitive understanding of single-scattering I/F. This is in no small part due to the variety of different media which it is used to describe, and the wide variation in illumination and viewing angles between different observations. For example, considering only Saturn's rings, observations

from Earth include everything from ring-plane crossing to Saturn's solstices, while the Voyager 1 and 2 flybys and Cassini's extensive observations include an even wider variety of emission angles and phase angles—not to mention the range of different albedoes and optical depths found in the ring system.

Let us consider several limiting cases where Chandrasekhar's formulae collapse down to simpler expressions, and the situations where they apply. In each case we will consider a uniform slab whose total normal optical depth is τ.

Optically thin case: $\tau \ll 1$ For both reflected light and transmitted light, when τ is much less than μ and μ_0:

$$\mathrm{I/F} \approx \frac{1}{4} P(\alpha) \varpi_0 \frac{\tau}{\mu}. \tag{2.40}$$

In this case, μ_0 is unimportant, since the incident light is able to penetrate throughout the slab and fully illuminate all particles. In fact, aside from the factor $P(\alpha)$, it doesn't even matter whether the light source is on the same side of the slab as the observer or the opposite side, since the expressions for reflected and transmitted singly-scattered light collapse down to the same expression.

However, I/F remains sensitive to both τ and μ. As long as the medium remains optically thin, the greater τ is, the more material is present to scatter light. To understand the effect of μ, recall that τ is the *normal* optical depth. When we observe the slab at a large emission angle, we are seeing a greater pathlength through the material, increasing the effective optical depth, and thus the number of scatterers, along the line of sight. Fig. 2.2 shows this relationship.

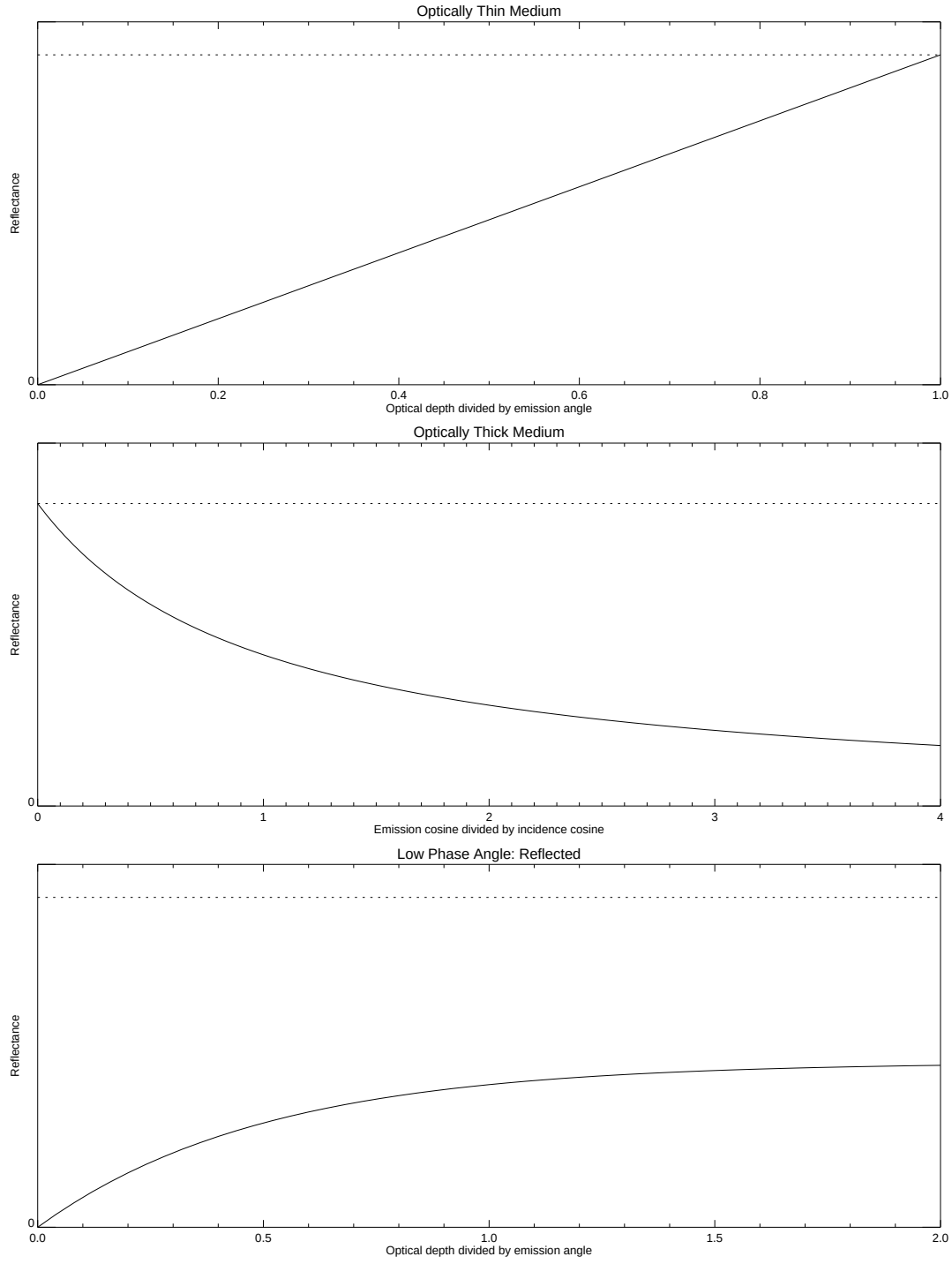

Figure 2.2: Reflectance as a function of relevant optical and geometrical parameters for various limiting cases. The dashed line indicates a value of $\frac{1}{4}P(\alpha)\varpi_0$.

Optically thick case: $\tau \gg 1$ In this case, there is no transmitted light, and the expression for reflected light reduces to:

$$\text{I/F} \approx \frac{1}{4} P(\alpha) \varpi_0 \frac{\mu_0}{\mu + \mu_0} \tag{2.41}$$

$$\approx \frac{1}{4} P(\alpha) \varpi_0 \frac{1}{\mu/\mu_0 + 1} \tag{2.42}$$

Note that the exact value of τ is irrelevant. When τ is large, the medium is simply optically thick, with little light penetrating beyond a depth of $\tau/\mu_0 \sim 1$.

Fig. 2.2 shows qualitatively how the reflectance depends on the ratio μ/μ_0. When μ/μ_0 is small ($\epsilon \gg i$ or $B_e \ll B_s$), the reflectance is greater. When μ/μ_0 is large ($\epsilon \ll i$ or $B_e \gg B_s$), the reflectance is lower.

Low phase angle: $\alpha \sim 0$ When observing an object in the outer Solar System from Earth, the phase angle is always very low. For example, for Jupiter, the maximum phase angle is about 11°, while for Saturn it is about 6°. In addition, observations are most often made when the planet is near opposition when the planet is highest in the nighttime sky, so $\alpha \approx 0$. If you were on that planet looking inward, the Earth and Sun would be very close in the sky. Thus, $\mu \approx \mu_0$, so for reflected light:

$$\text{I/F} \approx \frac{1}{8} P(\alpha) \varpi_0 (1 - e^{-2\tau/\mu}). \tag{2.43}$$

As the factor τ/μ increases (that is, for a more optically thick ring, or for a higher incidence and emission angle), the ring scatters a greater intensity, asymptotically approaching a maximum value of $\frac{1}{8} P(\alpha) \varpi_0$, i.e., the optically thick case of Eq. 2.42 in the limit that $\mu = \mu_0$.

2.3 Measuring I/F

In different observations different quantities related to the reflectance can be measured depending on whether the object is resolved.

2.3.1 Area-Averaged and Area-Integrated I/F ($\langle$I/F$\rangle$ and AIF)

Consider an object whose surface emits a uniform intensity I toward a detector of area A_d. Let the distance to the object be r and let A_o be the projected area of the object perpendicular to the line of sight to the observer, i.e., its projected area on the sky. We can compute the energy received by the detector in a time dt in two equivalent ways using Eq. 2.3. One way is to consider the energy emitted by the object in the direction of the detector. In that case, the area of interest is the emitting area of the object, $dA = A_o$, and the solid angle is the size of the detector as seen by the object, $d\Omega = A_d/r^2$. (The wise observer orients the detector perpendicular to the incoming light, so the distinction between πF and $\mathcal{F}$ is unimportant.) Plugging these into Eq. 2.3,

$$dE = I \cdot A_o \frac{A_d}{r^2} dt. \tag{2.44}$$

Equivalently, consider the object as seen by the detector. In this case, $dA = A_d$ and $d\Omega$ is the solid angle of the object on the sky, A_o/r^2. Because the light from the object is traveling through a vacuum, the intensity received by the detector is the same as the intensity emitted by the object. When we plug these expressions into Eq. 2.3, we find that the energy, as expected, is the same:

$$dE = I \cdot A_d \frac{A_o}{r^2} dt. \tag{2.45}$$

Solving Eq. 2.1 for the observed flux $\mathcal{F}_{obs}$ and plugging in our expression for dE, the flux received by the detector is

$$\mathcal{F}_{obs} = \frac{dE}{A_d dt} = \frac{IA_o}{r^2}. \tag{2.46}$$

Unresolved Objects

When observing an unresolved object, e.g., a star or a moon of Saturn as viewed from an Earth-based telescope, while the object's intensity may vary over its surface, we can only measure the total flux received by our detector. In an image, any unresolved object appears starlike. Using the technique of aperture photometry, we sum the total counts per pixel per second, DN, in the pixels that contain any measurable signal from the object, and take whatever measures are necessary to subtract DNs from other sources. To find the observed flux,

$$\mathcal{F}_{obs} = \gamma \sum_{x,y} DN. \tag{2.47}$$

we require a calibration factor γ. This figure may be known for a particular instrument, but if not, it can be determined by measuring the brightness of a source (e.g a star) with a known flux.

A detector is typically oriented so that it is perpendicular to the incoming rays of light, so $\mu = 1$. Then according to Eq. 2.5 the flux received is

$$\mathcal{F}_{obs} = \int I d\Omega, \tag{2.48}$$

where the integral is taken over the entire object. The intensity can be expressed in terms of the object's reflectance:

$$\mathcal{F}_{obs} = \int \mathrm{I/F} \cdot F_{\odot} d\Omega. \tag{2.49}$$

where $\pi F_\odot$ is the solar flux at the distance of the object from the Sun. Typically the size of the object is much less than its distance to the Sun, so $F_\odot$ varies little over the object. Recall that the flux is measured perpendicular to the ray of sunlight, and at a large distance from the Sun the rays can be considered parallel. All variation in the incident angle of sunlight due to curvature in the surface of the object is accounted for in the variation of I/F over the object. We can thus pull $F_\odot$ out of the integral, so

$$\mathcal{F}_{obs} = F_\odot \int \mathrm{I/F} d\Omega. \tag{2.50}$$

Since the object is unresolved, we have no information from this observation to describe how I/F varies over its surface, and we can only find the I/F averaged over the entire projected area of the object:

$$\mathcal{F}_{obs} = F_\odot \langle \mathrm{I/F} \rangle \Omega_o = F_\odot \langle \mathrm{I/F} \rangle \frac{A_o}{r^2}, \tag{2.51}$$

where Ω_o is the solid angle of the object on the sky and $A_o = \Omega_o r^2$ is its projected area. The object's average reflectance is then:

$$\langle \mathrm{I/F} \rangle = \frac{\mathcal{F}_{obs} r^2}{F_\odot A_o}. \tag{2.52}$$

In planetary astronomy we usually know the object's location, so we know r and we can calculate $F_\odot$ because we know its distance from the Sun. If we also know its size and orientation, we can calculate A_o. Using this information, and our calibration for the observed flux, Eq. 2.47, we can plug in these figures to calculate the observed $\langle \mathrm{I/F} \rangle$:

$$\langle \mathrm{I/F} \rangle = \frac{r^2}{F_\odot A_o} \gamma \sum_{x,y} DN. \tag{2.53}$$

However, we sometimes do not know the object's size or orientation, so we do not know A_o or Ω_o. In that case we can only find the area-integrated reflectance:

$$AIF = \langle \mathrm{I/F} \rangle A_o = \frac{\mathcal{F}_{obs} r^2}{F_\odot} = \frac{r^2}{F_\odot} \gamma \sum_{x,y} DN. \tag{2.54}$$

Since I/F is dimensionless, AIF is measured in units of area.

Resolved Objects

When we measure the reflectance of a resolved object, such as the disk of a planet or Saturn's rings viewed at a large opening angle, then rather than summing over all pixels, we measure the DN in each pixel. The flux received by the detector is still given by Eq. 2.49 but now we are integrating over just one pixel, so, in contrast to Eq. 2.51, the observed flux, F_{pix} is the flux received by just one pixel, and the reflectance is averaged only over that pixel:

$$\pi F_{pix} = F_\odot \langle \mathrm{I/F} \rangle_{pix} \Omega_{pix} = F_\odot \langle \mathrm{I/F} \rangle_{pix} \cdot \frac{A_{pix}}{r^2}. \tag{2.55}$$

Ω_{pix} is the angular size of the pixel and $A_{pix} = \Omega_{pix} r^2$ is the projected area of the pixel in the plane of the sky at the distance of the object from the observer, r.

The observed flux for a single pixel with a count of DN is just $\pi F_{pix} = \gamma DN$, where the factor of γ is the same as for the unresolved case, so an unresolved source, such as a star of known flux or a moon of known AIF, can be used to calibrate observations of a resolved object. The average reflectance of a pixel is then

$$\langle \mathrm{I/F} \rangle_{pix} = \frac{\pi F_{pix}}{F_\odot \Omega_{pix}} = \frac{\gamma DN}{F_\odot \Omega_{pix}}. \tag{2.56}$$

If we know the distance to the object, then the brightness of the pixel can be also be expressed as an area-integrated I/F:

$$\mathrm{AIF}_{pix} = \langle \mathrm{I/F} \rangle_{pix} \cdot A_{pix} = \frac{\pi F_{pix} r^2}{F_\odot} = \frac{r^2}{F_\odot} \gamma DN. \tag{2.57}$$

2.3.2 Vertically Integrated I/F (VIF)

Consider a ring system seen nearly edge-on with the rings oriented horizontally in the image. While the rings are resolved in the horizontal direction, their physical thickness may be much less than the instrument's resolution, but because of seeing and the instrument's point-spread function, the apparent thickness of the rings in such an image is usually several pixels.

We are thus forced to integrate in the vertical direction, and we obtain the vertically integrated I/F (VIF) by integrating perpendicular to the ring plane:

$$\mathrm{VIF} = \int \mathrm{I/F dz}. \tag{2.58}$$

We can measure the VIF by summing the DN in a strip of pixels spanning the full apparent thickness of the rings in the image. Eq. 2.58 can be rewritten as:

$$\mathrm{VIF} = \sum_{\mathrm{z}} \langle \mathrm{I/F} \rangle_{\mathrm{pix}} \sigma_{\mathrm{z}}, \tag{2.59}$$

where σ_z is the vertical height of a pixel in the plane of the sky at the distance of the observed rings. Because the rings are resolved horizontally, we will use Eq. 2.56,

$$\mathrm{VIF} = \sum_{\mathrm{z}} \frac{\gamma \mathrm{DN}}{\mathrm{F}_{\odot} \Omega_{\mathrm{pix}}} \sigma_{\mathrm{z}}. \tag{2.60}$$

Recall that $\Omega_{pix} = A_{pix}/r^2$. If $A_{pix} = \sigma_x \sigma_z$ where σ_x is the projected width of a pixel, then

$$\mathrm{VIF} = \frac{\gamma \mathrm{r}^2}{\mathrm{F}_{\odot} \sigma_{\mathrm{x}}.} \sum_{\mathrm{z}} \mathrm{DN}. \tag{2.61}$$

If the AIF of the pixels have already been measured, then

$$VIF = \frac{1}{\sigma_x} \sum_{z} AIF_{pix}. \tag{2.62}$$

Note also that $\sum_z AIF$ is simply the total AIF of the strip of pixels.

The VIF has units of length. As with AIF, the interpretation of the VIF depends on the assumptions made about the geometry of the rings. The VIF can be thought of as the projected thickness on the plane of the sky of an equivalent Lambert scatterer. This can give a sense of physical scale for unresolved rings viewed edge-on, which is helpful if the true thickness of the ring is unknown.

2.3.3 Radially Integrated I/F (Equivalent Width, W)

In their analysis of Voyager images of the narrow F ring, Showalter et al. (1992) calculate an equivalent width:

$$\mathrm{W} = \int \mathrm{I/F} da, \tag{2.63}$$

where a is the true radial distance from the center of Saturn.

If a ring is imaged from a large ring-opening angle so that the front and back of the ring are separate in the image, we can integrate radially at the ansa. If the image was taken or rotated so that the rings are horizontal, then we can integrate the I/F radially by summing a row of pixels just as with the VIF.

$$\begin{aligned} \mathrm{W} &= \sum_x I/F_{pix}\sigma_x & (2.64)\\ &= \frac{\gamma\sigma_x}{F_\odot \Omega_{pix}} \sum_x DN & (2.65)\\ &= \frac{\gamma r^2}{F_\odot \sigma_y} \sum_x DN & (2.66) \end{aligned}$$

The main difference between the equivalent width and the VIF is that the strip of pixels over which the sum is taken must be oriented so that σ_x must be the true radial width of the pixel in the ring plane, not the projected size in the plane of the sky.

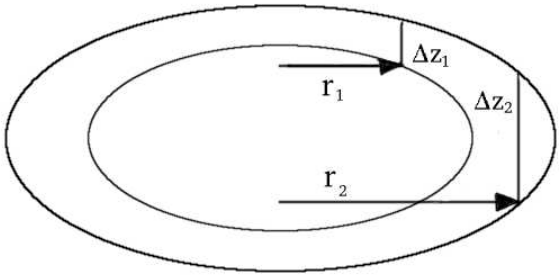

Figure 2.3: The projected height Δz of the ring on the sky varies with the horizontal distance r on the sky from the center of the planet, as shown in Eqs. 2.68 and 2.69.

Like VIF, W represents the radial width of an equivalent ring which behaves as a Lambert scatterer.

2.4 Some Typical Rings

The following simple examples illustrate the behavior of the single-scattering I/F, VIF, and W in some common types of rings.

2.4.1 A Flat Ring

Consider a uniform ring with an inner radius a_i and an outer radius a_o and negligible physical thickness, as shown in Fig. 2.3. Since the edge of a flat ring is extremely thin compared to its radial extent, the brightness is dominated by light reflected from the surface of the ring parallel to the ring plane.

When analyzing an image of such a ring, if the ring is resolved in the image we can measure the AIF and area-averaged I/F of each pixel as described in Section 2.3.1. However, if the ring is not vertically resolved, we can only sum the AIFs

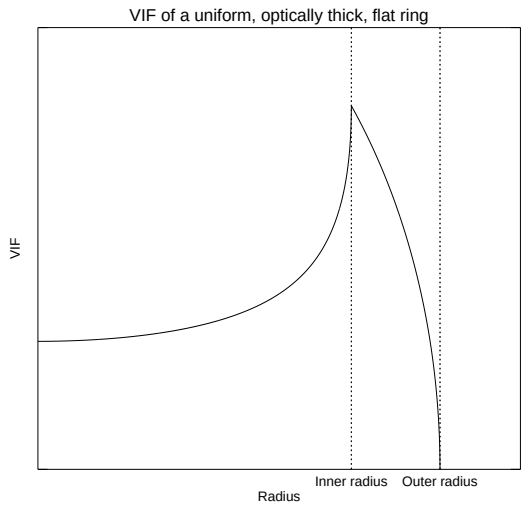

Figure 2.4: VIF(r) for a uniform, flat, optically thick ring that extends from an inner radius of a_i to an outer radius of a_o.

of a column of pixels and divide by the horizontal width of the pixel to obtain the VIF for that column as described in Section 2.3.2, Eq. 2.61.

The VIF of a uniform flat ring is simply

$$\mathrm{VIF}(r) = \mathrm{I/F}\Delta z(r), \tag{2.67}$$

where r is horizontal distance from the center of the planet in the plane of the sky and Δz is the projected vertical thickness of the ring in the plane of the sky.

Δz will vary with r and as can be seen in Fig. 2.3, the form of the expression $\Delta z(r)$ is different for radii less than or greater than the ring's inner radius, a_i. If the ring-opening angle to the observer is B so that $\mu = |\sin B|$, then the projected height of the ring at radii interior to a_i is

$$\Delta z_1 = \mu \left(\sqrt{a_o^2 - r_1^2} - \sqrt{a_i^2 - r_1^2} \right), \tag{2.68}$$

while for $a_i \leq r \leq a_o$,

$$\Delta z_2 = 2\mu \sqrt{a_o^2 - r_2^2}. \tag{2.69}$$

Δz_1 is only half the total projected height for an edge-on ring, so the total projected height for both the front and back of the ring is

$$\Delta z(r) = \begin{cases} 2\mu\left(\sqrt{a_o^2 - r^2} - \sqrt{a_i^2 - r^2}\right) & r \le a_i \\ 2\mu\sqrt{a_o^2 - r^2} & a_i \le r \le a_o. \end{cases} \tag{2.70}$$

This VIF(r) is plotted in Fig. 2.4.

Having measured a profile of VIF(r) in an image, if the dimensions and orientation of the rings are known, then we can fit Eq. 2.67 to determine the average reflectance of the ring.

If the observed ring is not uniform, one can potentially use a technique called onion-peel deconvolution (see e.g., Verbanac et al. (2005)), wherein the ring is modeled as a series of nested uniform rings. Measuring the VIF of the outermost part of the ring, where $r \approx a_o$, will reveal the $\langle$I/F$\rangle$ of only the outer region of the rings. For a smaller r, we can then use Eq. 2.67 to calculate the contribution of the outermost ring, and subtract it from the measured VIF. This yields the VIF contributed by the next ring in, allowing one to calculate its $\langle$I/F$\rangle$, and so on.

If single-scattering dominates the ring's brightness, we can interpret the I/F using Eq. 2.38 or 2.39. We typically know μ and μ_0, so we can find the product $P(\alpha)\varpi_0$. With observations at only one geometry, we cannot disentangle these two parameters, but we can assume a reasonable phase function based on other observations and thus estimate the single-scattering albedo of the ring particles, ϖ_0, or, if the single-scattering albedo is better known, estimate the phase function at the phase angle of our observations.

If instead the front and/or back of the ring are separable in the image, then we could sum pixels radially and divide by the width of the pixels to measure the

ring's equivalent width as in Section 2.3.3. Because the ring is uniform,

$$\mathrm{W} = \mathrm{I/F}(\mathrm{a_o} - \mathrm{a_i}), \tag{2.71}$$

where a_o and a_i are measured in the plane of the rings, not in the plane of the sky.

2.4.2 A Narrow, Optically Thin Ring

Consider an optically thin ring which has a narrow width in the radial direction, but has a vertical extent comparable to its width.

We can calculate its equivalent width from Eqs. 2.63 and 2.40:

$$\mathrm{W} = \frac{1}{4}\frac{\varpi_0 P(\alpha)}{\mu}\int \tau_v(a)da \tag{2.72}$$

$$= \frac{1}{4}\frac{\varpi_0 P(\alpha)}{\mu}\mathrm{D}, \tag{2.73}$$

where D is the equivalent depth of the ring as given in Eq. 2.20.

Recall that τ is the normal optical depth, measured perpendicular to the surface of the slab of scattering material. The factor μ accounts for the fact that increasing the emission angle increases the pathlength along the line of sight through the slab of scattering medium. For a flat ring, the scattering medium is a vertically thin slab in the ring plane, so the optical depth, τ_v is measured along the normal to the ring plane and $\mu = |\sin B|$ is the direction cosine to the observer if B is the ring-opening angle to the observer, as described in Section 2.2.1.

If we observe an optically and physically thin ring from a different point of view, near, but not in, the ring plane, and integrate the ring's reflectance perpendicular to the ring plane, we find

$$\mathrm{VIF} = \frac{1}{4}\frac{\varpi_0 P(\alpha')}{\mu'}\int \tau_r(z)dz. \tag{2.74}$$

μ' is again the sine of the incidence angle, but it is now smaller than in Eq. 2.73. α' will vary from the original α as well.

If the rings are viewed at a larger opening angle so that the front and back would both be visible, then the I/F of the front half would equal the I/F of the back half, but one would have compare the vertical thickness of the rings and the opening angle of the observation to see where the front half lies in front of part of the back half of the rings.

Recall from Section 2.1.2 that for an optically thin ring,

$$\int \tau_r(z)dz = \int \tau_v(r)dr = \mathrm{D}, \tag{2.75}$$

so

$$\mathrm{VIF} = \frac{1}{4}\frac{\varpi_0 P(\alpha')}{\mu'}\mathrm{D}, \tag{2.76}$$

which is similar to the expression for W in Eq. 2.73.

However, for a ring with some vertical extent, an observer near the ring plane will primarily be seeing the outer vertical edge of the ring. We can approximate the ring at each point as a plane slab of material tangent to the ring's actual vertical surface. The optical depth of the slab is τ_r, the radial optical depth of the ring, and the direction cosine for the observer is:

$$\mu' = \sqrt{1 - \left(\frac{r}{a_o}\right)^2}. \tag{2.77}$$

The inverse of this direction cosine is plotted in Fig. 2.5 to help visualize the profile of τ_r/μ'. When observing with a small phase angle, it is usually also a fair approximation to take $\mu_0 = \mu'$, since μ' varies from 0–90° over the ring and precise values of the incident and emission angles are not as critical as for other systems, e.g., a flat ring near RPX.

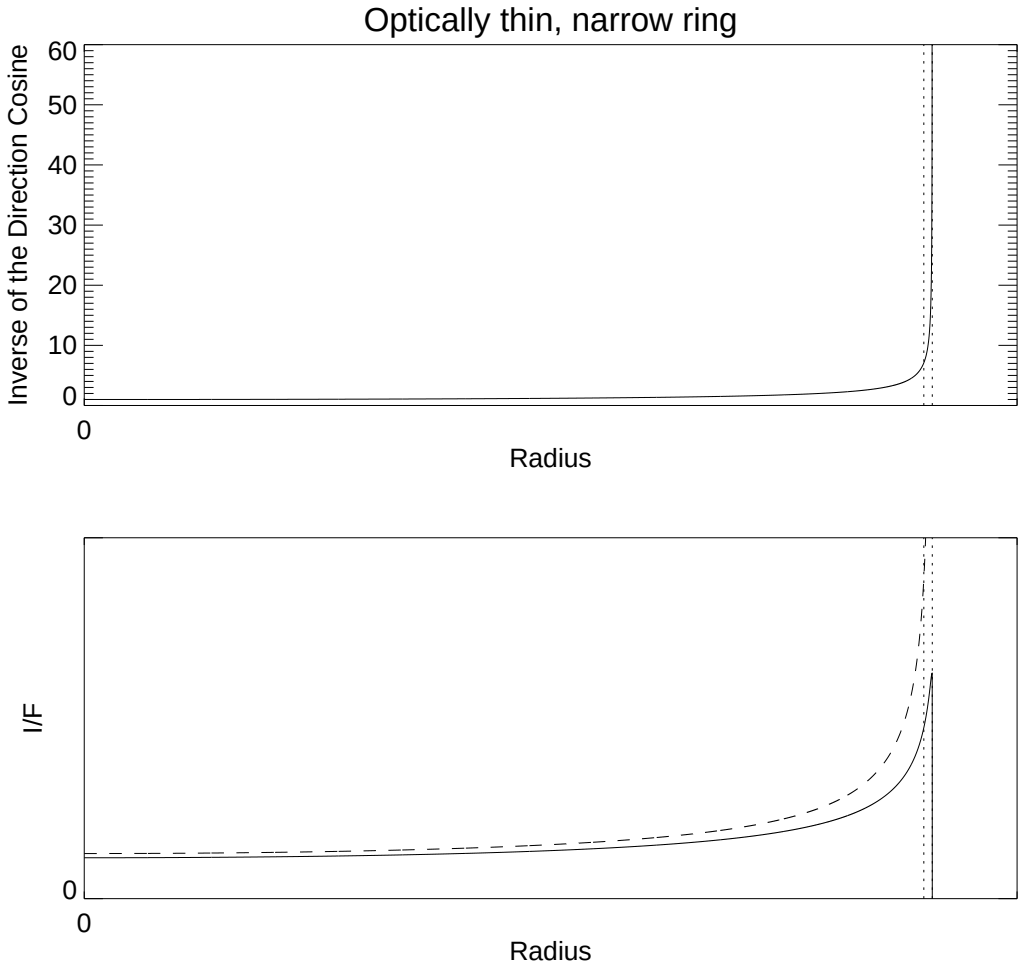

Figure 2.5: $1/\mu$ and I/F plotted vs. r for the front half of a uniform, narrow, optically thin ring. The inner and outer radii of the ring are indicated with vertical dotted lines. On the plot of I/F, the solid line was computed using Eq. 2.38 while the dashed line shows how the optically thin approximation (Eq. 2.40) is increasingly inaccurate toward the ansa. Both I/F curves were calculated for $\tau = 0.1$.

If the ring's VIF is measured at the point between the observer and the planet, $\mu' = 1$ and, and the equivalent width, W, is measured from a point of view directly above the ring, then VIF is equivalent to W, assuming the different values of α and α' for the two different observations are correctly taken into account.

This thin-slab approximation is appropriate when r is less than the inner radius of the ring, a_i. For $r > a_i$ there a much greater optical depth along the line of sight. Nonetheless, the approximation is still adequate for most narrow rings, which have $a_o - a_i \ll a_o$. Notice that μ' decreases rapidly toward the ansa ($r \approx a_o$), so that τ_r/μ' increases. This means that at the ansa, the optically thin approximation will not be valid, but also as long as $\tau_r/\mu' \approx 1$ for some $r < a_i$, the decreasing accuracy of the thin slab approximation becomes irrelevant, because the reflectance of an optically thick ring is insensitive to the exact value of the optical depth.

To calculate the reflectance profile of the entire ring as shown in Fig. 2.5, for each r, we use the full formula for the I/F of a slab in reflected light, Eq. 2.38, with μ' given by Eq. 2.77.

The plot shows the reflectance of just the front half of the ring. If this is the only ring in the system and the observation is made from the ring plane, the line of sight actually goes through both the front and back of the ring, then the total I/F can be computed by simply doubling the optical depth to account for the part of the ring that lies behind the front half. If the ring-opening angle is greater, then it must be determined where the ring overlaps and where the front and back of the ring are separated in the plane of the sky.

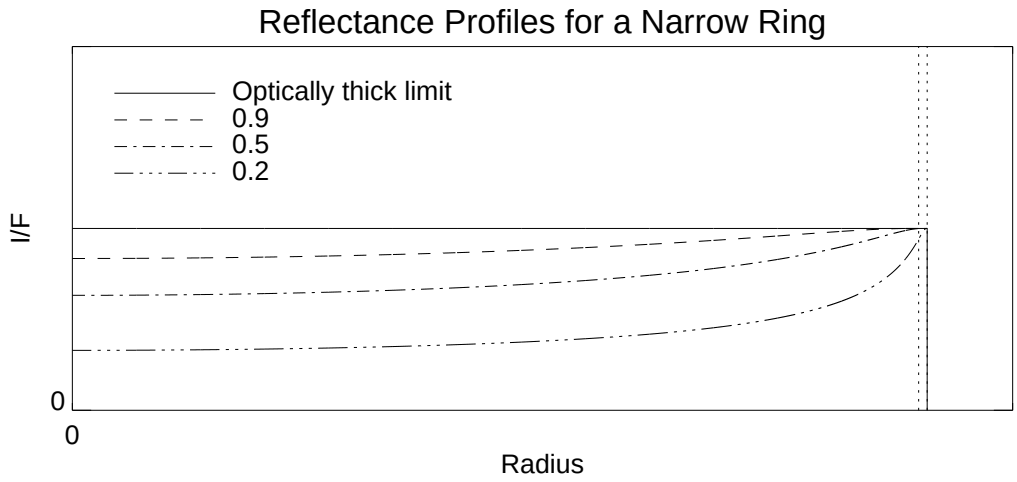

Figure 2.6: I/F(r) for a narrow ring viewed nearly edge-on. The vertical dotted lines indicate the inner and outer radii of the ring. The solid line is the reflectance profile for the optically thick limit. The broken lines were calculated from the optical depths given in the legend using the single-scattering formula for reflected light, Eq. 2.38.

2.4.3 A Narrow, Optically Thick Ring

Consider a uniform ring with narrow radial width. Let both the optical depths measured radially and perpendicular to the ring plane be >> 1. The I/F of any part of the ring can be calculated from Eq. 2.42, but care must be taken in determining the direction cosines μ and μ_0. What surface or surfaces of the ring are being observed? Assume that the ring is a toroid of rectangular cross-section, with a radial width Δa and a full height H.

If the ring is viewed edge-on, then as with the optically thin narrow ring, μ is given by Eq. 2.77. If the ring is observed from Earth, $\mu \approx \mu_0$, so

$$\mathrm{I/F} \approx \frac{1}{8}\mathrm{P}(\alpha)\varpi_0. \tag{2.78}$$

Profiles of I/F(r), calculated with Eq. 2.38 for τ_r=0.8 and 1.5, are plotted in Fig. 2.6, showing that as the radial optical depth of the ring is increased, the shape of the profile approaches the constant value of Eq. 2.78. From this point of view in the ring-plane, the VIF profile will just be

$$\mathrm{VIF} = H \cdot \mathrm{I/F}(r) = \frac{1}{8}P(\alpha)\varpi_0 H. \tag{2.79}$$

Similarly, if the observer is well above the ring plane (i.e., the ring-opening angle to the observer, B, is large), then the equivalent width can be measured. If the phase angle remains small,

$$\begin{aligned} \mathrm{W} &= \int I/F da & (2.80)\\ &\approx \frac{1}{8}P(\alpha)\varpi_0 \Delta a & (2.81)\\ &\approx \frac{\Delta a}{H} VIF. & (2.82) \end{aligned}$$

At intermediate viewing angles, the observed reflectance will be in part due to the horizontal (ring-plane) surface and in part to the vertical surface. Each surface

will have a different μ_0 and μ, and along the vertical surface, μ and μ_0 will vary, so if one computes an average reflectance based on an assumed width or height for the ring it should be interpreted carefully. Unlike the optically thin, narrow ring, any observation samples only the surface, so the assumed shape of the cross-section of the ring has a critical impact on the interpretation of VIF or W.

Chapter 3

Previous Observations and Models

The current model is intended to reproduce the brightness of Saturn's rings as observed near the Earth ring-plane crossing of 10–11 August 1995. Ring-plane crossings provide rich opportunities to investigate the ring system and, in this case, the crucial role played by the F ring allows us to probe its characteristics as well. We will begin, then, with a review of previous observations of Saturn ring-plane crossings and of the F ring itself.

3.1 Ring-Plane Crossings

The ring-opening angle of the Earth and Sun (the position of these bodies relative to Saturn's ring plane) is plotted for the 1995 RPX in Fig. 3.1. The apparent motion of the Sun is caused by Saturn's obliquity and its motion in its orbit. We can also see the effect of the Earth's motion in its orbit around the Sun. The Earth crossed the ring plane on 21 May 1995, 10 August 1995, and 11 February 1996, and the Sun crossed the ring plane on 19 November 1995.

3.1.1 Recent Ring-Plane Crossings and the Thickness of the Main Rings

The exact moment of the ring-plane crossing depends on the position of the pole of Saturn, and thus its equatorial plane, which is also to good approximation the ring plane. For the ring-plane crossings of 1966 and 1979–1980, the pole position was known precisely enough to predict the RPX to within several hours, but it

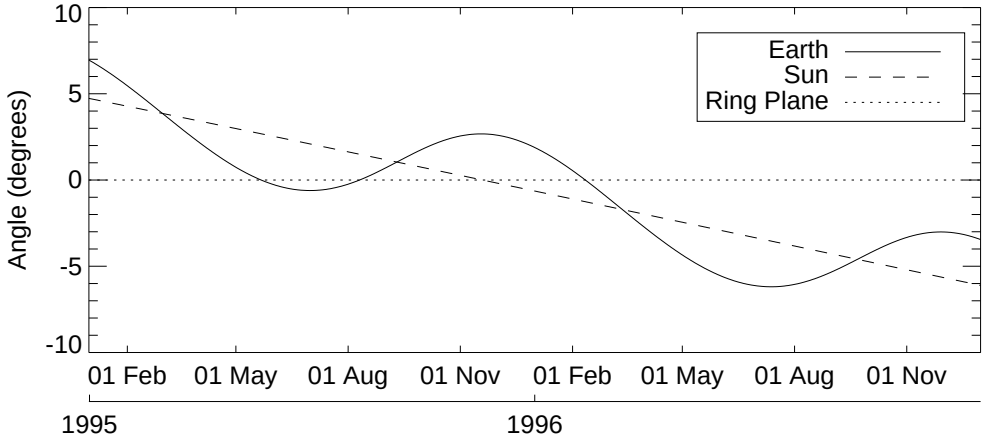

Figure 3.1: Planetocentric latitudes of the Earth and Sun during the 1995 RPX.

was not always possible to be observing at the moment of the RPX. Of course, the RPX also fell in the daytime for some observers.

In order to find the time of the RPX, the brightness of the rings is measured over a time baseline of several days around the RPX. Aside from the transition from the lit side of the rings to the dark side of the rings, the reflectance of the rings (i.e., their I/F) does not change a great deal. The ring-opening angle to the Sun, B_s changes relatively slowly. Near the Earth ring-plane crossing, the ring-opening angle, B_e is very small and varies approximately linearly with time. The projected area of the rings is proportional to $\sin B_e$, which, since B_e is small, is also linear, so the change of brightness over the days surrounding the RPX is also linear. On the dark side, the rings decrease in brightness slightly, if at all, as the RPX approaches. Once the Earth crosses over to the lit side of the rings, which have a much higher reflectance, then the brightness increases rapidly. Separate lines are fit to the ring

brightness on the dark and lit sides of the rings. The intersection of these lines then presumably marks the instant of the RPX.

At the RPX the ring brightness is also at its minimum, but does not go to zero. This residual ring brightness was generally assumed to be due to light reflected from the outer edge of the A ring or even the edge of the B ring seen through the Cassini Division (Brahic and Sicardy, 1981). The thickness of the rings was calculated by modeling the brightness as scattering from the edge of the rings

Based on observations of the 12–13 June 1966 RPX the photometric thickness of the rings was estimated from various observations and analyses to be 0.57 km (Bobrov, 1972), $0.8\ ^{+2.3}_{-0.8}$ km (Lumme and Irvine, 1979), 1.3 ± 0.3 km (Fountain and Larson, 1978), and 2.4 ± 1.3 km (Dollfus, 1979). These measurements were taken from photographic plates, and it was assumed that the ring reflectance was the same as the reflectance of Saturn. Modeling the RPX of 12 March 1980, Sicardy et al. (1982) found a thickness of $1.1\ ^{+0.9}_{-0.5}$ km by modeling the rings as a plane-parallel scattering layer of finite thickness. Bosh et al. (1997) used HST data to estimate an equivalent thickness of 1.4 ± 0.1 km of the rings from the residual brightness of the rings during the Earth ring-plane crossing of 22 May 1995, when the Earth passed from the lit to the dark side. This simple calculation assumed a geometric albedo of 1 for the rings.

Measuring the residual brightness of the rings at ring-plane crossings is not the only way to estimate the ring thickness. An occultation of the star δ Scorpii by the rings was observed using the Voyager 2 Photopolarimeter Subsystem (PPS). By measuring how quickly the transmitted flux of the occulted star changed as it crossed a sharp transition from opaque to transparent regions of the main rings, a upper limit of 200 m was placed on the thickness of the main rings. The advantage

of this method is that it is strongly localized, whereas large-scale warping of the ring-plane might affect estimates of ring thickness from edge-on views (Lane et al., 1982). Measurements of the forward-scattering of microwaves transmitted through the rings from Voyager 1 indicate a thickness of 10 m in the C ring and 20–50 m in the A ring (Zebker and Tyler, 1984).

Another approach to finding the thickness of the rings is to consider the dynamical behavior of the ring particles. Based on the damping distance of density and bending waves in the rings, other authors argue for a ring that is 30–35 m thick (Esposito et al., 1984). Goldreich and Tremaine (1978) modeled the rings as being composed of inelastically colliding spheres, and concluded that, if the rings are as old as the Solar System and have come to an equilibrium between viscous dissipation and stirring by collisions, then for the observed optical depth of the rings, the vertical thickness is less than 10 m. If instead a realistic value for the coefficient of restitution for balls of ice is assumed, the model implies that the rings are a monolayer. However, photometric models of a monolayer of particles reveal that they do not match the observed opposition surge, a sharp increase in brightness as the phase angle α approaches 0, unless the phase function used for the individual particles has a strong opposition surge (Hämeen-Anttila and Vaaraniemi, 1975).

Salo and Karjalainen (2003) combined a sophisticated dynamical model of the rings with a Monte Carlo photometric model in an attempt to explain many photometric effects observed in the rings, in particular the B ring's increased brightness at opposition (the opposition effect) and increasing brightness at larger opening angles (the tilt effect). The dynamical model sampled a small part of the rings populated with a somewhat narrower distribution of particle sizes than is usually assumed, starting at a few centimeters or meters and ranging up to 5 m. As

particles reached a steady state, the larger particles typically settled into a near-monolayer, while the smaller particles had a greater vertical distribution. This combination produced scattering effects differing significantly from a monolayer or a slab with a uniform vertical distribution of particles. The Monte Carlo technique used to determine the I/F of the rings is an improvement over previous analytical radiative transfer models because it does not require that the spacing between particles be much larger than the particle size. These higher filling factors were required to reproduce the observed the tilt effect of the B ring. The tilt and opposition effects were best reproduced by a model with a distribution of particle sizes from 10 cm to 5 m, although this rather high lower limit is inconsistent with the particle size distribution derived from the Voyager radio occultation experiment (Zebker et al., 1985).

The main ring thickness measured in the Voyager PPS occultation experiment and obtained from dynamical models of the rings is too small to account for the residual brightness of the rings at RPX. Observations of the ring-plane crossings of 1995 revealed that the recently discovered F ring is the source of this flux.

3.1.2 The Ring-Plane Crossing of 10 August 1995

Hubble Space Telescope (HST) was used to observe the Earth ring-plane on 10 August 1995 (Nicholson et al., 1996). Images were taken with the Planetary Camera (PC) and the Wide-Field Camera (WF3), the first and third chips, respectively, of the Wide-Field Planetary Camera 2 (WFPC2). The WF3 images contain both ring ansae, while PC images, which have a smaller field of view but higher resolution, cover only one ansa. See Table II of McGhee et al. (2001) for a detailed listing of the image times, targets, and exposure times in this dataset.

VIF Profiles

The projected height of the rings during the HST observations was much less than the image resolution of 0.1 arcsec≈650 km, so the rings are unresolved in the vertical dimension. These profiles were produced by rotating HST images to make the rings horizontal, summing columns of pixels perpendicular to the rings as described in Section 2.3.2, and subtracting a sky level obtained by summing columns above and below the rings in the images to remove significant scattered light from Saturn.

All of the resulting HST profiles are contaminated with light from satellites. Because their orbital motion carries the satellites a significant distance over the course of a single HST visit, it is often possible to remove much of their contribution by median filtering or averaging. The profiles extracted from WF3 and PC images have resolutions of 630 km and 290 km, respectively, and we combined all the images of each ansa from each HST orbit to produce composite profiles for the east and west ansae with a resolution of 650 km. For each data point in the final profile, we took the median value of the VIF profile from each image for the region within 325 km of r, and then we took the median of the local medians from each profile as the VIF for that point in the composite profile. If there were only two images of a given ansa in that orbit, in which case we took the *minimum* of the local medians as the value for the composite profile. This removes many of the satellites, but fails to remove all the traces of bright satellites, satellites near the ansa (where their motion in r is slower), or instances where two or more satellites were close to one another in r. Also, an excess of flux from the bright satellite Mimas in the sky subtraction resulted in dips in the 25:00 UT profiles.

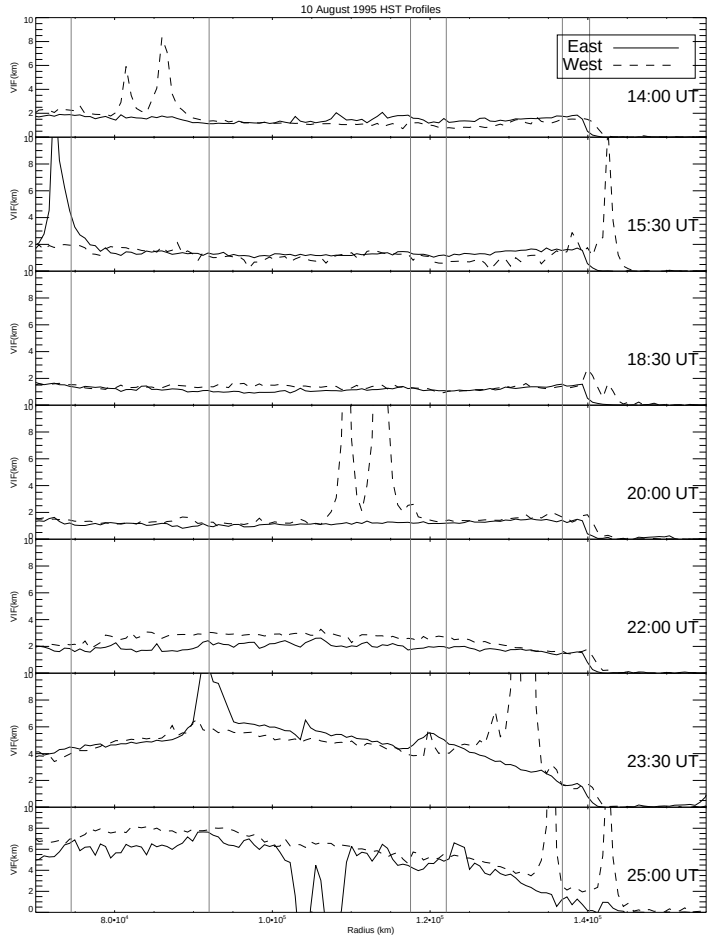

Figure 3.2: Profiles of VIF(r) extracted from images of the east and west ansae of the rings from HST images taken on 10–11 August 1995. All the profiles are plotted on the same vertical scale to show the change in the brightness of the rings over time. Fig 3.3 contains a detailed plot of the dark side profiles. The light from satellites was removed through median or minimum filtering of all the profiles from each ansa in each HST orbit, but the remnants of some satellites remain as valleys (where satellite light contaminated the sky subtraction) or peaks. The gray vertical lines indicate the inner border of the C ring, the boundary between the C and B ring, the inner and outer borders of the Cassini Division, the outer edge of the A ring, and the location of the F ring.

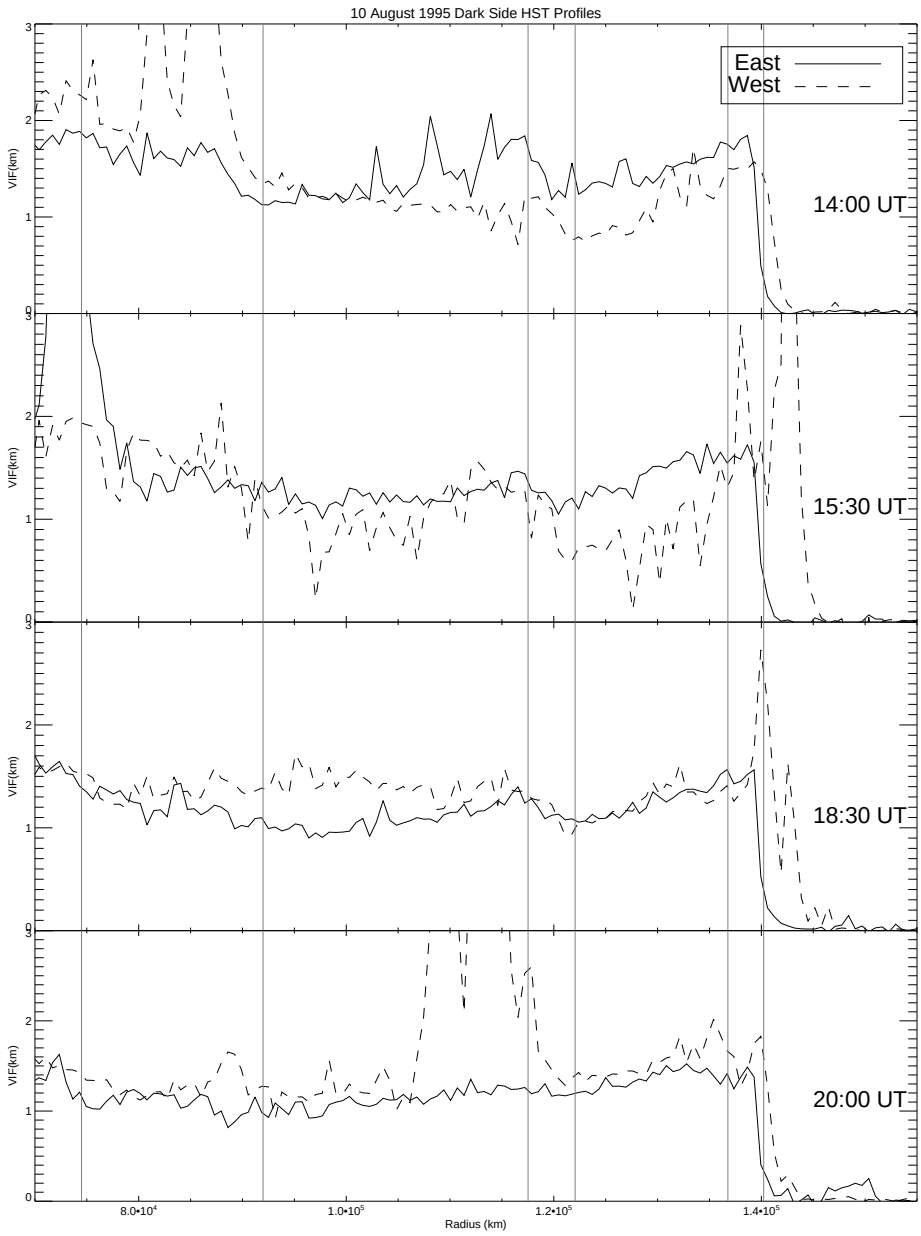

Figure 3.3: Profiles of VIF(r) for the east and west ansae extracted from HST images of the dark side of the rings taken on 10 August 1995. This is a detailed view of the same shown in Fig. 3.2.

The profiles are shown in Figs. 3.2 and 3.3. When viewed on the dark side (14:00-20:00 UT) and nearly edge on (22:00 UT), the rings are uniform in brightness out to a radius beyond the outer edge of the A ring (136,800 km) but drop off steeply at the location of the F ring (140,200 km). This implies that the edge-on brightness is dominated, not by light reflected from the vertical edge of the main rings, as had generally been assumed, but from the F ring, which is a narrow, optically thin ring that lies outside the A ring (Nicholson et al., 1996). After the ring-plane crossing, the brightness of the main rings rings increases dramatically—as does the asymmetry between the east and west ansae. The profiles are discussed in more detail in Section 5.4.

Radially Averaged VIF

The vertically integrated I/F (see Section 2.3.2) was radially averaged over a range of 80,000–120,000 km from the center of the planet. This radially averaged VIF, $\langle \mathrm{VIF} \rangle$, is plotted vs. time in Fig. 3.4. The intersection of linear fits to the $\langle \mathrm{VIF} \rangle$ of each ansa before and after the ring plane crossing was used to compute the ring-plane crossing time for each ansa.

The figure reproduced here differs slightly from the $\langle \mathrm{VIF} \rangle$ vs. time plot (Fig. 2 of Nicholson et al. (1996)) because a photometric calibration factor which differed slightly between the WF3 and PC images was not applied correctly to the data plotted in the original work, where all data were mistakenly scaled by the same factor. The data were taken with the narrowband methane filter at 890 nm, which is part of a unique "quad filter" in WFPC2 that is used only infrequently and was rather poorly calibrated at the time of the observations.

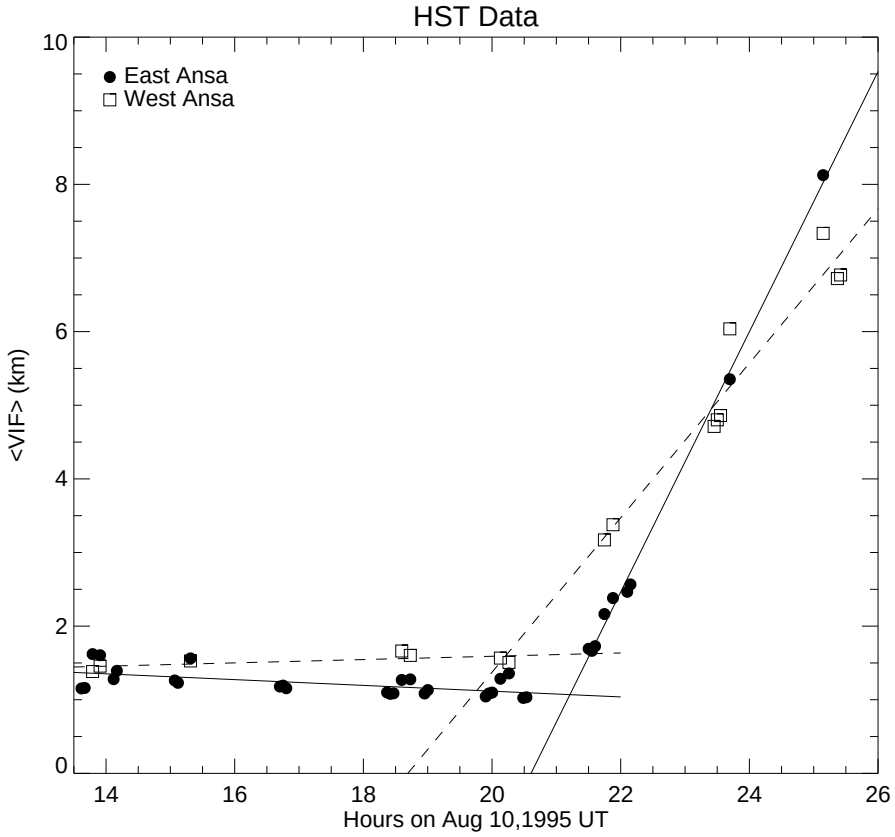

Figure 3.4: The evolution of the brightness of the rings during the Earth ring-plane crossing of 10 August 1995 as observed by HST. This plot shows data from both WF3 and PC chips, which have been correctly calibrated (cf. Fig. 2 of Nicholson et al. (1996).) The lines are linear fits to the data from the east and west ansae, before and after the ring-plane crossing. Their intersection gives the ring-plane crossing time, which we find to be 21:13±3 min. for the east ansa and 20:13±22 min for the west ansa.

Table 3.1: Average HST orbit ⟨VIF⟩ and asymmetries for 10 August 1995.

	UT Time	$\langle VIF \rangle_E$ (km)	$\langle VIF \rangle_W$ (km)	$\Delta\langle VIF \rangle$ (km)
	14:00	1.37 ± 0.19	1.42 ± 0.04	-0.05 ± 0.19
	15:30	1.35 ± 0.15	1.53	-0.18 ± 0.21
Dark	16:30	1.18 ± 0.02	—	—
	18:30	1.15 ± 0.08	1.63 ± 0.03	-0.48 ± 0.09
	20:00	1.13 ± 0.12	1.54 ± 0.03	-0.41 ± 0.12
	22:00	2.09 ± 0.36	3.27 ± 0.10	-1.18 ± 0.37
Lit	23:30	5.35	5.10 ± 0.54	0.25 ± 0.75
	25:00	8.13	6.94 ± 0.28	1.19 ± 0.40

The ring-plane crossing times computed from these incorrectly calibrated data were 20:20 UT ± 8 min for the west ansa, and 21:09 UT ± 2 min for the east ansa. With the correct photometric calibration, we find slightly different ring-plane crossing times: 21:13 UT ± 22 min for the west ansa and 20:13 UT ± 3 min for the east ansa.

Nicholson et al. (1996) also averaged over all precrossing data points and found an average dark side ⟨VIF⟩ of 1.53±0.09 km on the west ansa and 1.22±0.17 km on the east ansa. It appears that the data used in this calculation were calibrated correctly.

In Fig. 3.4, each cluster of data points is from one HST orbit. The mean values of the ⟨VIF⟩ of each ansa for each orbit are given in Table 3.1.2. The uncertainties are computed from the scatter in data points because Nicholson et al. (1996) do not quote any uncertainties for individual measurements; when only one image

was taken of one of the ansae during an orbit, no uncertainty is given here. To characterize the asymmetry in brightness between the east and west ansae of the rings, we simply compute

$$\Delta\langle \mathrm{VIF} \rangle = \langle \mathrm{VIF} \rangle_{\mathrm{E}} - \langle \mathrm{VIF} \rangle_{\mathrm{W}}. \tag{3.1}$$

In the 16:30 UT orbit, only the east ansa was imaged, so no asymmetry is given, and when the error has only been computed for one ansa, we estimate the error in the asymmetry by multiplying that error by $\sqrt{2}$.

In the observations of the dark side of the rings, the west ansa $\langle \mathrm{VIF} \rangle$ was slightly but systematically greater than the east ansa $\langle \mathrm{VIF} \rangle$, with the asymmetry increasing as the ring-plane crossing approached. It is not clear if the difference in brightness between the ansae is statistically significant in the early data.

In the first observations after the ring-plane crossing, at 22:00 UT, the west ansa is brighter than the east ansa by 44%. The sense of the asymmetry reverses around 24:00 UT, and in the last set of data, the east ansa is brighter than the west ansa by 16%.

Because the relative calibration of the WF3 and PC images remains a matter for concern, we will be comparing our model results only to results from WF3, because these images contain both ansae, and thus the relative calculation between east and west ansae is more certain. Fig. 3.5 is a plot of $\langle \mathrm{VIF} \rangle$ vs. time including only WF3 images. Computing the RPX times as before, we calculate the east ansa crossing time to be 21:13±3 min. and the west ansa crossing time to be 20:25±10 min. Table 3.1.2 gives the asymmetries calculated from the $\langle \mathrm{VIF} \rangle_E$ and $\langle \mathrm{VIF} \rangle_W$ in the WF3 images for each HST orbit.

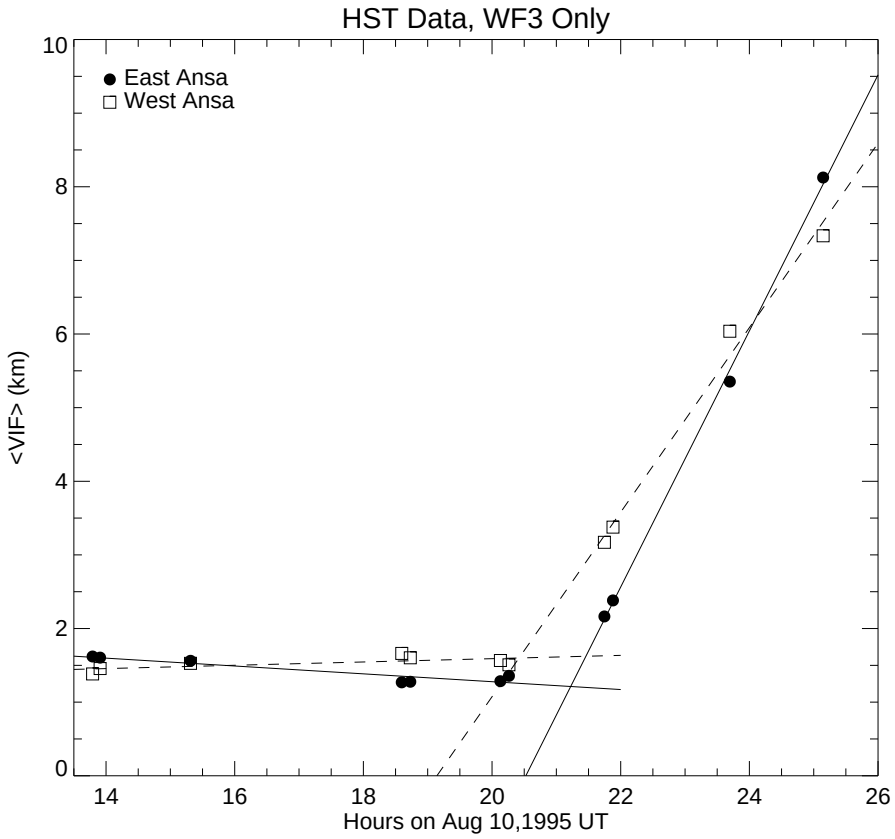

Figure 3.5: The evolution of the brightness of the rings during the Earth ring-plane crossing of 10 August 1995 as observed by HST. This plot shows data from only the WF3 chip (cf. Fig. 3.4 which contains data from both chips.) The lines are linear fits to the data. The intersection of linear fits for each ansa before and after the ring-plane crossing gives the ring-plane crossing time. Using WF3 data only, we find the RPX times to be UTC 21:13±3 min for the east ansa and UTC 20:25±10 min for the west ansa.

Table 3.2: Radially averaged VIF in km for WF3 images on 10 August 1995.

UT Time	$\langle \text{VIF} \rangle_E$ (km)	$\langle \text{VIF} \rangle_W$ (km)	$\Delta\langle \text{VIF} \rangle$ (km)
14:00	1.61	1.41	0.19
15:30	1.56	1.53	0.03
18:30	1.28	1.63	-0.35
20:00	1.32	1.54	-0.22
22:00	2.27	3.28	-1.01
23:30	5.35	6.04	-0.69
25:00	8.13	7.33	0.80

RPX Asymmetry and the F Ring

A plausible explanation for the asymmetry in brightness between the east and west ansae was suggested when the inclination of the F ring was discovered (Olkin and Bosh, 1996; Bosh et al., 2002). In most geometries, the F ring's very small inclination (0.0064°) is irrelevant. However, when the ring opening angle is on the same order as the inclination, this tilt becomes the key to understanding the brightness of the ring system.

During the solar RPX of 21 November 1995, the ring opening angle to Earth was large enough ($B_e = 2.67°$) that the rings were resolved vertically in HST observations. The F ring, which was bright in transmitted light and easily visible outside the main rings, disappeared about $\sim 35°$ to the rear of the east ansa. At the time of the observations, it was suggested that the F ring was inclined, and entered the shadow of the main rings at this point Nicholson et al. (2000),

and this was borne out when the F ring's inclination was determined from stellar occultations (Olkin and Bosh, 1996).

At the time of the 10 August 1995 RPX, the front of the F ring obscured the main rings more on one ansa than the other(Nicholson et al., 1999). We show the geometry of the F ring and the main rings in Fig. 4.1. This asymmetry is one of the few available observations that is sensitive to the vertical structure and radial optical depth of the F ring. It is the goal of the present model to characterize a vertical profile of optical depth for the F ring which can reproduce the observed difference in brightness between the east and west ansae.

3.2 The F Ring

The F ring is a challenging target for observations. It a weak back-scatterer and its proximity to the bright main rings makes it nearly impossible to detect from Earth except at a ring-plane crossing. The bulk of studies of the F ring have come from spacecraft observations, with some stellar occultations observed from spacecraft and from Earth.

3.2.1 F Ring Observations by Pioneer 11 and Voyagers 1 and 2

The F ring was discovered in 1979 in images from Pioneer 11, the first spacecraft to visit Saturn, which afforded the opportunity to observe Saturn's rings in a forward-scattering geometry (Gehrels et al., 1980). It was noted even in these low resolution images that the F ring's appearance is uneven and clumpy. During its flyby of Saturn in November 1980, Voyager 1 confirmed that there are brighter

clumps scattered around the F ring, and also revealed the eccentricity of the F ring. Higher resolution views revealed that the core of the F ring comprises one to three strands, each ∼20 km wide, which were spread over a radial range of ∼ 250 km. The strands appeared braided and knotted in some locations. This complicated structure is believed to be due to interactions with the F ring's shepherd moons, Pandora and Prometheus, which were discovered in Voyager 1 images (Smith et al., 1981). In its August 1981 flyby, Voyager 2 revealed there were as many as four strands in some locations, and that kinking and braiding was not present at all longitudes. Over the course of the encounter, it was also observed that the clumps in the F ring maintain their integrity for up to 15 orbits around Saturn (Smith et al., 1982; Showalter, 2004).

Showalter et al. (1992) conducted a photometric analysis of the Voyager F ring images and occultation data. In wide-angle camera images, the F ring typically varies in brightness by a factor of four with longitude. The phase behavior of the rings was fit by assuming two populations of ring particles: small particles with a radius comparable to the observing wavelength, which are primarily forward-scattering, and larger particles, which are primarily back-scattering. Since the smaller particles will tend to be removed from the ring on fairly short timescales (Burns et al., 1984), it is likely that the larger particles provide a source for the smaller particles. In radio occultation data, which are only sensitive to centimeter-sized and larger particles, the F ring appears as a narrow ring with a width of < 1 km, implying that larger particles are confined to to the ring's core (Marouf et al., 1986).

Showalter et al. (1992) assembled equivalent width measurements of the F ring made at many different observing geometries by Voyager 1 and 2, and found that

when the equivalent width is scaled by the emission cosine, it depends systematically upon α. However, in addition to the variation due to the phase function $P(\alpha)$, the values of μW showed a wide scatter, which implies significant longitudinal variation in ϖ_0 or D, consistent with the clumpy appearance of the F ring.

With a semimajor axis of 2.33 Saturn radii, the F ring is very close to Saturn's Roche limit for fluid bodies with a density of $\sim$1 g/cm^3. This means that within the F ring, ring particles can be bound to one another by their own gravity, but would be very close to being pulled apart by tidal forces, and thus would be easily disrupted by collisions with other ring particles.

Studying the F ring from Earth is difficult because the ring is only weakly back-scattering and it is very close to the strongly back-scattering A ring, so the light from the F ring is usually overwhelmed. An exception is during a ring-plane crossing. The brightness of the main rings is extremely small near the Earth's ring-plane crossings and also when they are observed from the unlit side of the rings. Also, near the ring-plane crossing, the F ring falls between the observer and the main rings. The vertical extent of the F ring is unknown, but in the hours near an Earth ring-plane crossing, sunlight scattered by the F ring dominates profiles of brightness as a function of radius (Nicholson et al., 1996; Poulet et al., 2000a).

During the 1995 RPX, Prometheus and Pandora were recovered for the first time since the Voyager encounters. Surprisingly, Prometheus was 19° of longitude behind its expected position in its orbit (Nicholson et al., 1996), and Pandora was ahead by a comparable amount, suggesting that both the mean motions of both satellites have changed since the Voyager era (French et al., 2003).

The structure of the F ring and its interactions with Prometheus and Pandora provide an interesting dynamical puzzle that motivates a great deal of continuing

study. Observations by the Cassini spacecraft will no doubt contribute a great deal to our future understanding of this system.

3.2.2 Optical depth profile

Stellar occultations provide an opportunity to probe the F ring's optical depth. As discussed in Section 2.1.2, the changing brightness of the star as it shines through the rings gives a profile of the optical depth of the ring along the line of sight from the observer to the star.

The earliest optical depth profile of the F ring comes from the Voyager 2 PPS occultation experiment in 1981. The star δ Scorpii passed behind the rings as viewed by the spacecraft, allowing the optical depth profile of the rings to be determined with a radial resolution of $\sim$100 m. The occultation was observed in the ultraviolet (0.264 μm). The profile showed a core $\sim$ 3 km wide with an optical depth of the order several tenths, and of the order 1 in some narrow ($<$ 0.5 km) regions. Both this core and the optically thin envelope show a complex structure (Lane et al., 1982). In this profile, the envelope extends at least 50 km radially, and the total equivalent depth of the F ring was measured to be 4.33$\pm$0.13 km (Showalter et al., 1992). The ring-opening angle to Voyager during the occultation was 28.3° (Nicholson et al., 1990) so this profile is primarily a measurement of τ_v.

Voyager 1 also transmitted radio waves through the rings which were received by Earth-based telescopes. This provided optical depth profiles at λ =3.6 cm and 13 cm with resolution comparable to the PPS resolution. In these profiles, only a compact core was seen, and the larger envelope was absent, probably due to the envelope being composed of particles with sizes much less than λ. Showalter et al. (1992) measured equivalent depths from these profiles of 0.283$\pm$0.035 and

0.153±0.066 km for λ=3.6 and 13 cm, respectively, but no measurable intensity passed through the densest part of the core, a region $\sim$ 300 m wide (Marouf et al., 1986), so these equivalent depths may be a slight underestimate.

An occultation of the star 28 Sgr was observed from Earth in 1989 at several wavelengths from several observatories (Nicholson et al., 2000). The F-ring equivalent depth measured at IRTF at $\lambda = 3.1\mu$m was 3.79±0.08 km, and at Palomar, at $\lambda = 3.9\mu$m, the equivalent depth was 3.0±0.1 km. Notably, in this occultation, the F ring was sampled at two different longitudes. Because the occultation stretched for almost four hours, most observers had technical difficulties and/or poor atmospheric conditions at various times during the observations. However, the data quality at MacDonald Observatory was good enough obtain two separate equivalent depths for the F ring at $\lambda = 2.3\mu$m, D=2.8±0.1 km at ingress and 3.6±0.1 km at egress, showing significant variation (Bosh et al., 2002).

In 1995, very close to ring-plane crossing ($B_e = -2.67°$), an occultation of the star GSC5249-01240 was observed while the Earth was on the dark side of Saturn's rings. The F ring's equivalent depth was measured to be 7.41±0.15 km in the visible by HST. Observations at the Infrared Telescope Facility on Mauna Kea at $\lambda = 2.3\mu$m yielded an equivalent depth of 5.76±0.06 km (Bosh et al., 2002).

Each case, the optical depth profile was interpreted with the assumption that the F Ring was flat, with negligible vertical extent and structure, so that the measured variation in optical depth was considered to be radial variation. However, if the F ring had some vertical extent, then this interpretation would be misleading. For a ring-opening angle to the observer B, a vertical feature of height h would be interpreted as a radial feature of width $\Delta r = h/\tan B$. For example, the core of the F ring observed in the PPS occultation was interpreted as 3 km in radial

width. However, if the F ring was assumed to be of negligible radial width (an interpretation that is, of course, defied by imagery of the ring from high ring-opening angles), one could interpret the core as being 3 km$\cdot \tan 28.3^\circ = 1.6$ km tall instead. More likely the ring is actually somewhere between these extremes. For larger ring-opening angles, a non-zero height will cause have an even greater exaggeration in the derived radial width.

However, as previously discussed in Section 2.1.2, given that the F ring is largely optically thin, the assumed geometry has little effect on the measured equivalent depth.

3.3 The Model of Poulet

In order to reproduce the observed brightness of the rings of Saturn in the near-infrared (0.89 and 2.2 μm) during the 1995 Earth ring-plane crossings, Poulet et al. (2000a) constructed a photometric model of the rings in which the F ring was the most important contributor to the brightness of the rings close to the ring-plane crossing. Poulet applied this model to observations of the dark side of the rings from the University of Hawaii 2.2-m telescope on 22–23 May, 1995, from the European Southern Observatory 3.6-m telescope at La Silla, Chile on 9–10 August, and of the lit side of the rings from the Pic du Midi 2-m telescope on 12–13 August. Observations of both the dark and lit sides of the rings from Hubble Space Telescope on August 10–11 were also analyzed, but no attempt was made to reproduce the east-west asymmetry noted in Section 3.1.2.

In Poulet's model of the main rings, sunlight reflected from any vertical surfaces or from vertical bending waves was assumed to be negligible. The brightness of

sunlight reflected from or transmitted through the main rings was modeled using the single and multiple scattering relations of Chandrasekhar (1960).

Because reflected light from the main rings is much brighter than the light from the F ring when the sunlit side of the rings is observed, brightness profiles of the lit side were modeled to find the product of the single-scattering albedo and the phase function for the main rings. From the model, Poulet extracted the product of the single-scattering albedo and phase function from the lit side profiles.

Compared to the phase function, Poulet considered the main-ring albedoes to be better constrained by Voyager observation, ground-based observations of the integrated spectrum of the main rings, and other observations made by the same author (Poulet et al., 1999). Dividing by these albedoes left the phase function for each region of the ring, which was fitted over the range of phase angles for the RPX observations (3.55–5.55°). The phase function was assumed to take a power-law form (the same as Eq. 4.35 below) with an index that characterizes the degree to which the ring particles are forward- or back-scattering. In general, the resulting index was lower than $n = 3$, the value derived from Voyager images in the visible by Doyle et al. (1989) and Dones et al. (1993), indicating a less strongly backscattering phase function for the main rings.

These single-scattering albedoes and phase functions for the main rings were then used to model the transmitted sunlight for observations of the dark side of the rings. In addition to transmitted sunlight, Poulet included reflected and transmitted saturnshine for the dark-side ring profiles, but this is insignificant compared the reflected sunlight on the lit side of the rings.

In this model, the F ring was treated as a uniform uninclined "ribbon," or a toroid of rectangular cross-section. Based on the shape of profiles made from

the images of the dark side of the rings near the RPX, where the light contributed by the main rings was minimized, Poulet derived a radial optical depth of τ_r ~0.16±0.05 from HST data, 0.19±0.05 from the Hawaii data, and 0.27±0.10 from ESO data. Poulet assumes a ring of radial width 50±5 km (Murray et al., 1997), yielding an equivalent depth D=8±3 km.

Using this optical depth, Poulet then modeled the contribution of the F ring to the brightness of the profiles. Multiple scattering was neglected. The F ring was modeled as having a two-component population of dust and large particles. The small particles have sizes comparable to the wavelength, and their phase functions are derived from Mie theory, assuming spherical particles of water ice with a power law size distribution with an index $q = -4$. The large particles were modeled as dust-covered spheres with the same power-law phase function as the main ring particles and single-scattering albedoes derived from the theory of van de Hulst (1974). The albedoes of both populations depend on the composition of the particles, and both the case of pure water ice and contaminated ice with an imaginary component of the index of refraction of 10^{-3} were tested. In addition to τ_r, the remaining free parameters in the F ring model were the physical height of the F ring, H, the fraction of dust, f, and the power-law index of the large-particle phase function, n. These three parameters contribute to just one measurable quantity, the brightness of the F ring, so they cannot be uniquely determined.

Some values of Poulet's fit parameters lead to unphysical results and were rejected. If the F ring were dominated by large, backscattering particles (i.e., $f \ll 0.5$), the ring must still be > 2 km in vertical height. Showalter et al. (1992) found that large bodies in the F ring are confined to a narrow core < 1 km in width, and it is unlikely that the core's vertical extent would be so much greater than

its radial extent. It is more plausible that the F ring's brightness is dominated by the dust component ($f > 0.5$) because this is supported by Voyager observations of the strongly forward-scattering phase function of the F ring (Showalter et al., 1992). Model results with larger values of H are more reasonable because the radial width of the outer dusty envelope of the F ring was measured to be ~ 40 km in the Voyager PPS observation of the occultation of the star δ Scorpii (Lane et al., 1982) and 50±5 km in Voyager images (Murray et al., 1997). Additionally, for $f > 0.5$ and $H < 2 - 3$ km, n must be unrealistically large.

Poulet restricted n to the range 2–4. For each n, the H required match the observed brightness can be expressed as a function of f. Assuming a uniform toroidal shape for the F ring and using a radially-averaged vertical normal optical depth $\tau_v = 0.074$ derived from a model by Showalter et al. (1992), Poulet calculated the physical width corresponding to $H(f)$ using the expression $\Delta a = H\frac{\tau_r}{\tau_v}$. By requiring this width to match the observed width of the F ring envelope, the range of physical heights of the F ring was found to be $H = 21 \pm 4$ km. The corresponding range of dust fractions is f=0.8–0.9, depending on n and whether the ice is contaminated, resulting in lower values of f, or pure, which gives higher values of f.

In order to explain the asymmetry in ring brightness observed by HST (Nicholson et al., 1996), the present work uses a similar model, but we include the obscuration of the main rings by the F ring and *vice versa* and the F ring's inclination (Bosh et al., 2002). We also use a more realistic profile of the F ring's vertical structure.

Chapter 4

A Photometric Model of the Rings of Saturn

4.1 A Brief Sketch of the Present Model

Our photometric ring model is composed of the F ring, divided into a front half and a back half, and the main rings of Saturn, including the A, B and C rings, and the Cassini Division. These components are constructed from arrays of pixels, in the case of the main rings, or cells, in the case of the F ring. For each pixel or cell, we assign an optical depth, τ, a single-scattering albedo, ϖ_0, a phase factor $P(\alpha)$ and coordinates in space and on the sky.

The ring model is constructed in image layers which each account for the light scattered by different parts of the ring system. Each image is an array $m \times n$ pixels in size. The value of each pixel in the image layer is the AIF for that position on the sky (the u-v plane, as described in Sec. 4.3.3).

Theoretically, a total model image could be constructed by summing the images of all the components. However, this image is never actually produced. Instead, as each component image is computed, a profile of vertically integrated I/F is extracted as in Eq. 2.62, where $\mathrm{AIF}_{pix} = \mathrm{I/F}_{pix} A_{pix}$, and

$$\mathrm{VIF}(u) = \frac{1}{\sigma_u} \sum_v \mathrm{AIF}_{\mathrm{pix}}(u, v), \tag{4.1}$$

where σ_u is the width of an image pixel. The u coordinate can be converted into r, the horizontal distance from the center of Saturn, measured in the plane of the sky, giving us a profile, $\mathrm{VIF}(r)$. Image layers which are not needed for further

calculations are deleted to save space in memory. A profile representing the total light scattered from the rings can be obtained by summing the profiles of the components. This is referred to as the total profile, $\mathrm{VIF}_{tot}(r)$.

A VIF profile can then be averaged radially to compute the radially averaged, vertically integrated I/F:

$$\langle \mathrm{VIF} \rangle = \frac{1}{120,000 - 80,000 \text{ km}} \int_{80{,}000 \text{ km}}^{120{,}000 \text{ km}} VIF dr \tag{4.2}$$

$$= \frac{\sigma_u}{120,000 - 80,000 \text{ km}} \sum_u VIF. \tag{4.3}$$

We average over the same range that was used to compute $\langle \mathrm{VIF} \rangle$ by Nicholson et al. (1996). Just as the total model profile is the sum of the component profiles, the total $\langle \mathrm{VIF} \rangle$ of the ring system is then the sum of the $\langle \mathrm{VIF} \rangle$s of the components.

The five component images are:

1. The sunlight reflected from the back of the F ring minus that which is blocked by the main rings (henceforth labeled BF).

2. The sunlight reflected or transmitted by the main rings (MR)

3. The light from the back of the F ring that is blocked by the front of the F ring (FBF)

4. The light from the main rings that is blocked by the front of the F ring (FBM)

5. The sunlight reflected from the front of the F ring (FF).

The AIF values of the pixels of the blocked-light images (FBF and FBM) are negative, indicating light that is absorbed or scattered by the F ring so that it does not reach the observer.

The brightness of each component is calculated using the single-scattering equations, Eqs. 2.38 and 2.39. For the main rings, the single-scattering albedo ϖ_0 has not been directly measured at the wavelength of these observations (0.89 μm). The F ring albedo and phase function are even less certain. We will determine the factor $P(\alpha)\varpi_0$ for the F ring as the model is constructed by comparing to the measured brightness of the rings on the dark side, when the brightness of the main rings is very small. For the main rings, we will begin with nominal values of $P(\alpha)\varpi_0$ calculated from a Callisto-type phase function and the albedoes of the different ring regions as measured through the Voyager clear filter, and scaled based on a spectrum which averages over the main rings. A scaling factor will then be applied to the modeled brightness of the main rings so that the total model results match the brightness measured on the lit side of the rings by HST.

For comparison with the HST observations, we model the ring brightness for the following times on 10 August 1995: 14:00, 15:30, 18:30, 20:00, 22:00, 23:30, and 25:00. All times are given in UT, and the last time is actually 1:00 UT on 11 August 1995. From 14–20 UT, the Earth is on the dark side of the main rings, and from 22–25 UT the Earth is on the lit side.

4.2 Ring Geometry

The correct orientation of the main rings and the F ring in this model is critical, first because of the rapidly changing ring-opening angle, and also because it is the inclination of the F ring that is responsible for the asymmetry of observed brightness in the HST images.

Table 4.1: Earth and Sun ring-opening angles for HST observations.

UT Date and Time		$B_e(^\circ)$	$B_s(^\circ)$
1995 Aug. 10	14:00	−0.0078	1.498
1995 Aug. 10	15:30	−0.0061	1.497
1995 Aug. 10	18:30	−0.0026	1.496
1995 Aug. 10	20:00	−0.0008	1.495
1995 Aug. 10	22:00	0.0015	1.493
1995 Aug. 10	23:30	0.0031	1.492
1995 Aug. 11	1:00	0.0050	1.492
1995 Nov. 21	14:00	2.670	−0.0290

4.2.1 Orientation of the Main Rings

For the main rings, the only important geometrical parameters are the ring-opening angles to the Sun and Earth, B_s and B_e, respectively. These were interpolated from ephemerides provided by the Planetary Data System's Rings Node (`http://pds-rings.seti.org`). Values of the ring-opening angles for the approximate times of the HST observations are shown in Table 4.1. We choose one representative time for each orbit. The right ascension and declination of Saturn (α_s, δ_s) were also obtained from this ephemeris.

4.2.2 Orientation of the F ring

Using data from several stellar occultations, Bosh et al. (2002) created a kinematic model of the F ring. The parameters of the model were the F ring's semimajor axis (a), eccentricity (e), longitude of the pericenter (ϖ), precession rate of the

Table 4.2: F ring orbital parameters from Bosh et al. (2002) for the pole of French et al. (1993).

a	140223.7 ± 2.0 km
$e \times 10^3$	2.53 ± 0.06
ϖ^a	$24.1 \pm 1.6°$
$\dot{\varpi}$	$2.7001 \pm 0.0004°$/day
i	$0.0064 \pm 0.0007°$
Ω^a	$17.3 \pm 3.9°$
$\dot{\Omega}$	$-2.6877°$/day

[a]Longitudes are measured from the intersection of the main-ring plane with the Earth's equatorial plane. The reference plane is Saturn's equator, and the reference epoch is J2000.0=JD 2451545.0.

pericenter ($\dot{\varpi}$), inclination (i), longitude of the ascending node (Ω) and regression rate of the ascending node ($\dot{\Omega}$). The F ring orbit solution is dependent on the assumed geometry of the planet, so Bosh et al. (2002) provide fits made using different orientations for the pole of Saturn. We use the fit that was computed using the Saturn pole of French et al. (1993). The orbital parameters fitted for the F ring using this pole are listed in Table 4.2.

At its highest point, the F-ring plane rises $a_f \sin i_f = 16$ km above the main-ring plane, and it dips below the ring plane by the same amount. Compared to the 140,200 km mean radius of the ring, this vertical displacement is very small, and in most geometries it is irrelevant. However, when the rings are viewed nearly edge on, the projected height of the main rings on the sky, $137{,}000 \cdot \sin B_e$ km, is comparable to 16 km, so that the F ring's inclination can have important consequences. This is the case in the observations of 10–11 August 1995. For example, in the last set of

HST images on August 11 at 1:00 UT, $B_e = 0.0050°$ so that the projected height of the main rings is only 12 km.

In particular, if the F ring's line of nodes is neither parallel nor perpendicular to the line of sight, the front of the F ring obscures one ansa of the main rings more than the other. Conversely, the main rings block more of the back of the F ring on one ansa than on the other. This can create an asymmetry in ring brightness that may account for the asymmetry observed in HST observations of the 1995 RPX by Nicholson et al. (1996).

For our model, we must thus determine the geometry of the F ring at the time of these observations, taking into account the regression of the ascending node. The longitude of the ascending node of the F ring is measured from the ascending node of Saturn's equatorial plane (i.e., the ring plane) on the Earth's equatorial plane of J2000.0.

The orientation of Saturn's equatorial plane is derived from the position of its pole, which was not available from the Rings Node ephemeris, so we compute the right ascension and declination of Saturn's pole (α_p, δ_p) using the pole and precession rate of Saturn derived by French et al. (1993) in epoch B1950 coordinates:

$$\alpha_p = 38.4128° + T\ (0.00057699°/\text{yr}) \tag{4.4}$$

$$\delta_p = 83.32329° + T\ (0.00006604°/\text{yr}) \tag{4.5}$$

where T is the time since 1980 November 12, 23:35:32 UTC. The resulting pole position is then precessed to the J2000 coordinate frame.

The inclination of the ring plane relative to the Earth's equatorial plane is

$$J = 90° - \delta_p \simeq 6.5° \tag{4.6}$$

in J2000 coordinates and the longitude of the ascending node of Saturn's ring plane on the Earth's equatorial plane as measured from the vernal equinox is

$$N = \alpha_p + 90^\circ \simeq 130.6^\circ. \tag{4.7}$$

U is defined as 180° minus the longitude of the ascending node measured in the ring plane from the instantaneous direction to Earth. U is obtained from the following equations:

$$\cos B_e \sin U = \cos J \cos \delta_s \sin(\alpha_s - N) + \sin J \sin \delta_s \tag{4.8}$$

$$\cos B_e \cos U = \cos \delta_s \cos(\alpha_s - N) \tag{4.9}$$

where α_s and δ_s are the geocentric right ascension and declination of Saturn. Both $\sin U$ and $\cos U$ must be computed to resolve the ambiguities in the arcsine and arccosine functions.

U can then be used to locate the ascending node of the Earth's equatorial plane in the ring plane, which is the reference point from which the ascending node of the F ring is measured. This allows us to determine the geometry of the rings, as shown in Fig. 4.1. Notice how the back of the F ring is obscured to a greater degree by the main rings on the west ansa before the ring-plane crossing. The F ring itself obscures the east ansa of the main rings to a greater degree than the west ansa until a time of about 23.5 UT. Shortly after this time, the Earth passed through the F ring plane, after which the F ring obscures the main rings more on the west ansa than the east ansa.

4.3 Coordinate Systems

There are three different coordinate systems used in the model. All are right-handed coordinate systems with their origins at the center of mass of Saturn.

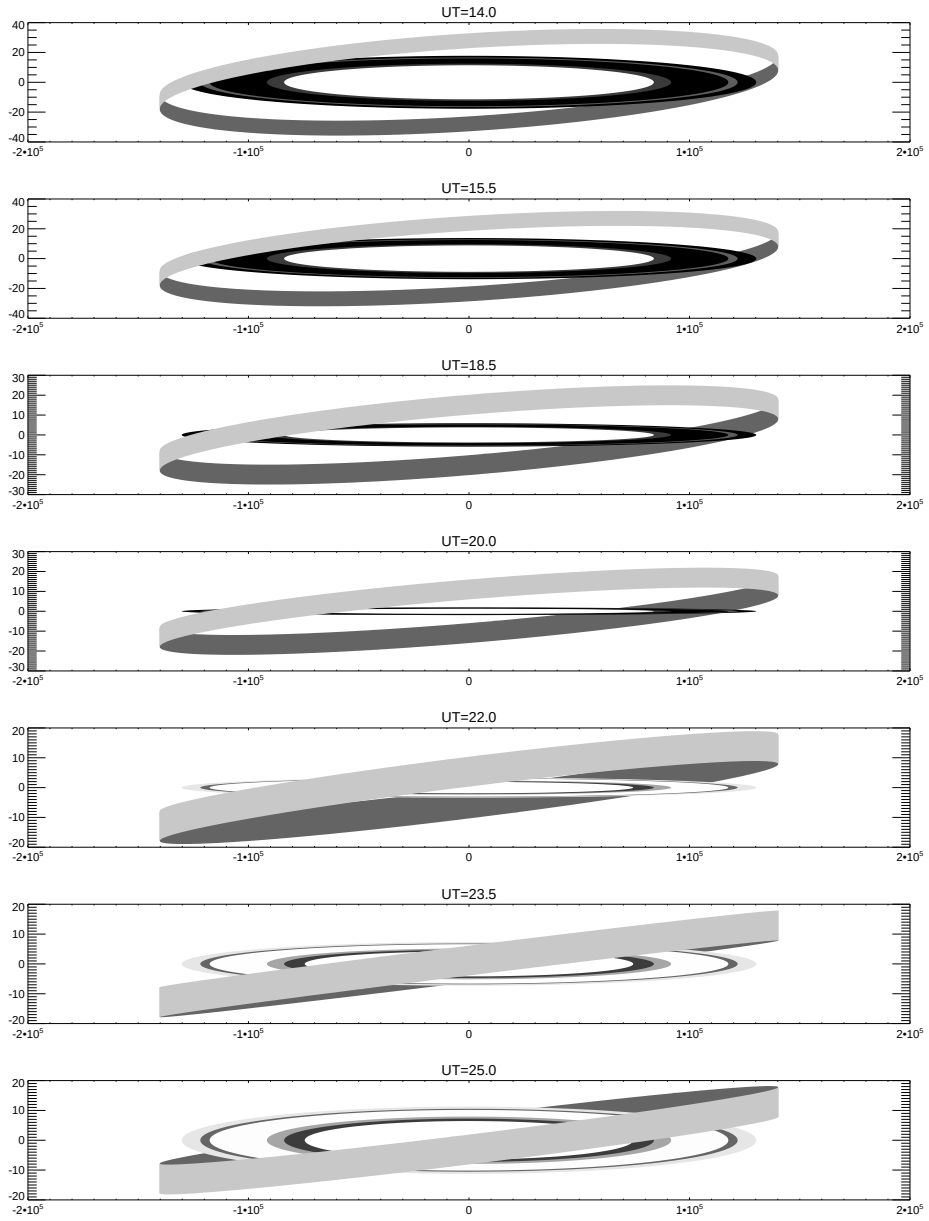

Figure 4.1: Diagrams showing the geometry of the rings at each of the HST observation times. The total vertical thickness of the F ring was arbitrarily set to 10 km. Note that the Earth crosses the plane of the main rings at ∼21:00 UT and the plane of the F ring at ∼23:30 UT. See Appendix B for more discussion of the latter.

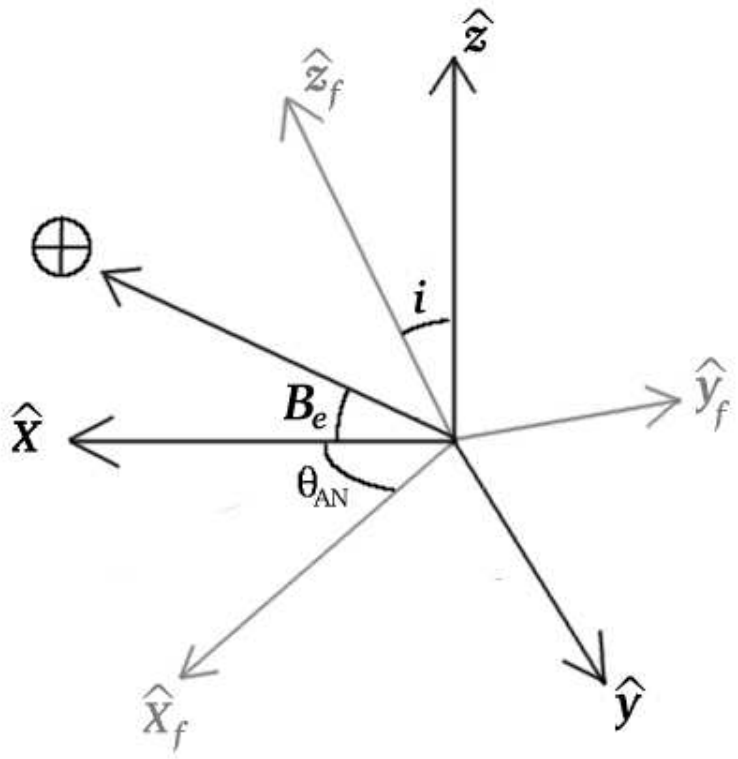

Figure 4.2: Cartesian coordinate axes for Saturn equatorial coordinates and F-ring coordinates. The ring-opening angle to Earth, B_e, shows the tilt of the ring plane, which is also Saturn's equatorial plane. Relative to Saturn equatorial coordinates (black), the F-ring coordinate axes (gray) are tilted due the inclination, i, of the F ring and rotated so that $\hat{x}_f$ axis is aligned with the ascending node of the F ring, which is located θ_{AN} away from the $\hat{x}$ axis of the Saturn equatorial system, in the ring plane. In this image, $\hat{x}$, the Earth, and $\hat{z}$ all lie in the same plane, as do $\hat{x}$, $\hat{x}_f$, and $\hat{y}$.

4.3.1 Saturn Equatorial Coordinates

In the Saturn Cartesian equatorial coordinate system, $\hat{\mathrm{x}}$ is the line-of-sight to the observer projected into the ring plane (i.e., the equatorial plane). $\hat{\mathrm{y}}$ is the intersection of the plane of the sky and the rings, pointing to the west. $\hat{\mathrm{z}}$ is Saturn's north pole.

Saturn spherical equatorial coordinates, $\mathbf{r_s} = (r_s, \theta, \phi)$ are also used. θ is the azimuthal coordinate, measured from $\hat{\mathrm{x}}$, and ϕ is the elevation above the ring plane.

To convert from Saturn Cartesian equatorial coordinates to Saturn spherical equatorial coordinates, we simply use the standard formulae:

$$r_s = \sqrt{x^2 + y^2 + z^2} \tag{4.10}$$

$$\theta = \tan^{-1}(y/x) \tag{4.11}$$

$$\phi = \tan^{-1}(\frac{z}{\sqrt{x^2 + y^2}}). \tag{4.12}$$

Similarly, to transform from spherical to Cartesian coordinates we use:

$$x = r_s \cos\theta \cos\phi \tag{4.13}$$

$$y = r_s \sin\theta \cos\phi \tag{4.14}$$

$$z = r_s \sin\phi. \tag{4.15}$$

4.3.2 F-ring Coordinates

For the F ring Cartesian coordinate system, $\hat{x}_f$ points to the F ring's ascending node with respect to the ring plane, and $\hat{z}_f$ is the normal to the F ring's orbital plane.

The longitude of the ascending node of the ring plane on the Earth's equator of J2000, measured from $\hat{x}$, is

$$\theta_{RP} = 180^\circ - U. \tag{4.16}$$

The position of the ascending node of the F ring in Saturn spherical coordinates is then:

$$\theta_{AN} = \Omega + \theta_{RP}. \tag{4.17}$$

The conversion between Saturn Cartesian coordinates and F-ring Cartesian coordinates is simply a rotation:

$$x_f = x\cos\theta_{AN} + y\sin\theta_{AN} \tag{4.18}$$

$$y_f = -x\sin\theta_{AN}\cos i + y\cos\theta_{AN}\cos i + z\sin i \tag{4.19}$$

$$z_f = x\sin\theta_{AN}\sin i - y\cos\theta_{AN}\sin i + z\cos i \tag{4.20}$$

and to convert from F-ring coordinates to Saturn Cartesian equatorial coordinates, we use:

$$x = x_f\cos\theta_{AN} - y_f\sin\theta_{AN}\cos i + z_f\sin\theta_{AN}\sin i \tag{4.21}$$

$$y = x_f\sin\theta_{AN} + y_f\cos\theta_{AN}\cos i - z_f\cos\theta_{AN}\sin i \tag{4.22}$$

$$z = y_f\sin i + z_f\cos i \tag{4.23}$$

$$\tag{4.24}$$

More commonly used are F-ring cylindrical coordinates, $\mathbf{r_f} = (r_f, \theta_f, h)$, where r_f is the semimajor axis of the F ring, a constant 140223.7 km (Bosh et al., 2002), θ_f is the angle in the F-ring plane measured from the $\hat{x_f}$ axis and h is the height above the F-ring plane.

The following standard equations are used to convert from F-ring Cartesian coordinates to F-ring cylindrical coordinates:

$$r_f = \sqrt{x_f^2 + y_f^2} \tag{4.25}$$

$$\theta_f = \tan^{-1}\left(\frac{y_f}{x_f}\right) \tag{4.26}$$

$$h = z_f \tag{4.27}$$

and from F-ring cylindrical coordinates to F-ring Cartesian coordinates:

$$x_f = r_f \cos\theta_f \tag{4.28}$$

$$y_f = r_f \sin\theta_f \tag{4.29}$$

$$z_f = h. \tag{4.30}$$

The Cartesian coordinate axes for Saturn equatorial coordinates and F-ring coordinates are shown in Fig. 4.2.

4.3.3 u-v Coordinates

This two-dimensional coordinate system lies in the sky plane. $\hat{\mathrm{v}}$ is the projection of Saturn's north pole on the plane of the sky, and $\hat{\mathrm{u}}$ is perpendicular to $\hat{\mathrm{v}}$, pointing along the western ring ansa (not toward the east, as is conventional in radio astronomy.)

To find the u-v coordinates of some point around Saturn which is specified in three dimensional Saturn Cartesian equatorial coordinates, we use the equations:

$$u = y \tag{4.31}$$

$$v = -x\sin B_e + z\cos B_e. \tag{4.32}$$

There is no corresponding inverse transformation because there is no depth information in u-v coordinates.

4.4 Construction of the Ring Models

For the main rings and the F ring, arrays of coordinates are constructed which specify the location of each pixel or cell.

4.4.1 Assembling the Main Rings

The main rings are constructed as an image array $m \times n$ pixels in size. The center of the planet is located at the center of the image. Each pixel is assigned a value of u and v as described in Sec. 4.3.3. Using these coordinates, the radial distance of each pixel from the planet's center in the ring plane is computed:

$$r_s = \sqrt{u^2 + (v/\sin B_e)^2}, \tag{4.33}$$

where B_e is the Earth ring-opening angle.

4.4.2 Assembling the F Ring

The F ring is created as a collection of two-dimensional arrays. One contains values of F-ring coordinates, and another h. The number of azimuthal elements is m_f and the number of vertical elements is n_f. The number of cells of this array, $m_f \times n_f$, is limited by the amount of computer memory required to manipulate the array. The radial component, r_f, is treated as a constant even though the F ring is eccentric and has a radial width of ≈ 50 km. The physical radial thickness of the F ring, being much smaller than the semimajor axis, has very little impact on the photometric model. (See Section 2.4.2.) The only effect of the eccentricity would be a radial displacement of $a_f \cdot e_f$ =350 km of the edge of the F ring at the ansa, which is less than 600 km, the horizontal resolution of the main-ring model. The total vertical extent of the F ring model is $h_f = 60$ km.

Once the arrays have been constructed, the cells can be positioned in space by transforming their coordinates. For each cell, cylindrical F-ring coordinates, (r_f, θ_f, h), can be transformed to Saturn spherical equatorial coordinates, (r_s, θ, ϕ), and Saturn Cartesian equatorial coordinates, (x, y, z). We also convert the coordinates of the F ring cells into u-v coordinates, though this gives only a list of (u, v) coordinates for each cell. We must then assign cell values to pixels in a two-dimensional array in u-v space if we wish to produce an image.

We split the F ring into the back and front halves by making separate lists of cells with $x < 0$ and $x > 0$ respectively, using the x coordinate from the Saturn-centered Cartesian coordinate system.

4.4.3 Pixel and Cell Size

There are four resolutions to be concerned with in this model: the azimuthal and vertical resolutions of the F-ring component and the vertical and horizontal resolutions of the u-v image. We will not vary the resolution, so the chosen values must be appropriate for all the observing times.

We wish the horizontal scale of the final image to be comparable to the HST resolution of ∼650 km. The horizontal size of the u-v image must be large enough to accommodate the rings. Extending this size doesn't have much effect on the computational requirements of the model, and we chose a generous width of 300,000 km. We chose the number of pixels in the horizontal direction to be $m = 500$, so that the horizontal size of the pixels is $\sigma_u = 600$ km.

In the HST images, the rings are unresolved vertically, since the maximum projected height of the main rings on the sky during these observations is $r_A|\sin B_e|$ ≈41 km. However, for our model we require a vertical resolution sufficient to accu-

rately model the F ring's obscuration of various main-ring features. The narrowest of the important main-ring features is the Cassini Division. Its radial width is 4537 km. In the plane of the sky, its smallest projected height will be found at the outer edge of the planet's disk, r =60,330 km (see Eqs. 2.68 and 2.69). For the smallest ring-opening angle, at 20:00 UT, the projected height of the Cassini Division on the sky at r =60,330 km is 0.07 km, so this would be the minimum desired resolution. We halve this resolution to 0.035 km. In this model, the F ring's full height is 60 km, so given the F ring's inclination the vertical size of the image must be $2 \times a_f \sin(B_e + i) + 30$ km. For the largest ring-opening angle (which, for the F ring plane, is $\approx B_e + i = 0.0078 + 0.0064 = 0.0142^\circ$) this gives a total height requirement of 129.5 km, which we round to 130 km. The required number of pixels in the vertical direction is rounded up to $n = 4000$ pixels, which gives $\sigma_v = 0.0325$ km/pix.

We would like the F ring cells to be as small as possible. However, smaller cells mean larger arrays. This increases the time it takes to run the two for-loops which are required to construct the model. The more stringent requirement is that we must have enough available memory to manipulate the large arrays. This limits the total size of the F ring array.

We have chosen the horizontal size of the F ring cells to be approximately $\frac{1}{4}$ the size of the main-ring pixels. The number of cells distributed azimuthally around the F ring is $m_f = 6000$ cells. The horizontal size of these pixels is then $2\pi a_f / m_f$ =146.6 km/cell. We would like the vertical size of the F ring cells to be $\frac{1}{4}\sigma_v$ as well, but this requires more than 7000 cells in the vertical direction, for a total of more than 42,000,000 cells, and this exceeded our memory constraints. We chose a slightly smaller number of vertical cells, $n_f = 6000$,which results in a

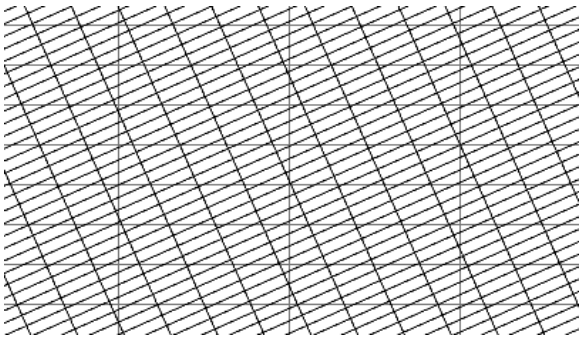

Figure 4.3: The relative size and orientation of the main ring pixels and F ring cells. The main ring pixels (horizontal grid) are σ_u=600 km wide by σ_v =0.0325 km high. The F ring cells are 146.6 km wide by 0.01 km tall, and are tilted due to the inclination of the F ring. This picture shows a region of the u-v plane ∼2000 km wide by ∼ 0.3 km tall, and the vertical scale in this diagram is exaggerated by a factor of 400. A full u-v image is 300,000 km by 130 km.

more manageable array size of 36,000,000. This gives us a a vertical cell size of 60 km/6000 = 0.01 km, or about $\frac{1}{3}\sigma_v$.

Fig. 4.3 shows the relative sizes and orientations of the main-ring pixels and the F ring cells as they appear in the model.

4.5 Optical Parameters

In addition to the coordinates described above, each cell or pixel is also assigned optical parameters that characterize the scattering properties of the material at that position in the ring.

4.5.1 The Optical Depth of the Main Rings

The normal optical depth of the main rings as a function of the distance R from the center of Saturn was measured at high radial resolution from ground-based observations of the occultation of the star 28 Sgr by Saturn's rings in 1989 (Nicholson et al., 2000). We have chosen to use the optical depth profiles derived from the data taken by the Lick 1-m Nickel reflector at a wavelength of 0.9 μm, because these observations are of consistent quality and are at nearly the same wavelength as the HST observations. A table of the derived normal optical depths at 10 km resolution was provided by Planetary Data System's Rings Node (personal communication, M. Gordon, 2002). We use only the egress data, as the ingress data are noisier due to thin clouds over the observing site.

The reflectance of the main rings in transmitted sunlight (before the RPX) or reflected sunlight (after the RPX) is computed using Eqs. 2.39 and 2.38, respectively, which are the single-scattering functions of Chandrasekhar (1960). The transmitted reflectance peaks strongly when $\mu < \tau < \mu_0$, and since at ring-plane crossing μ is very small, the computed reflectance is very sensitive to optical depths near zero. Typical noise in the Lick observations of the flux of the occulted star was $\sigma(F_{obs})/F_0$=0.025, where F_{obs} was the observed flux of the occulted star and F_0 its its unocculted flux. The optical depth is

$$\tau = -\mu \ln\left(\frac{F_{obs}}{F_0}\right), \tag{4.34}$$

where $\mu = \sin B_e = 0.429$. Thus the 2.5% noise level translates into an uncertainty in τ of 0.01. Whenever the optical depth value is less than this, it is set to zero to eliminate spurious peaks in the computed reflectance profiles. The optical depth profile for the main rings used in this model is plotted in Fig. 4.4.

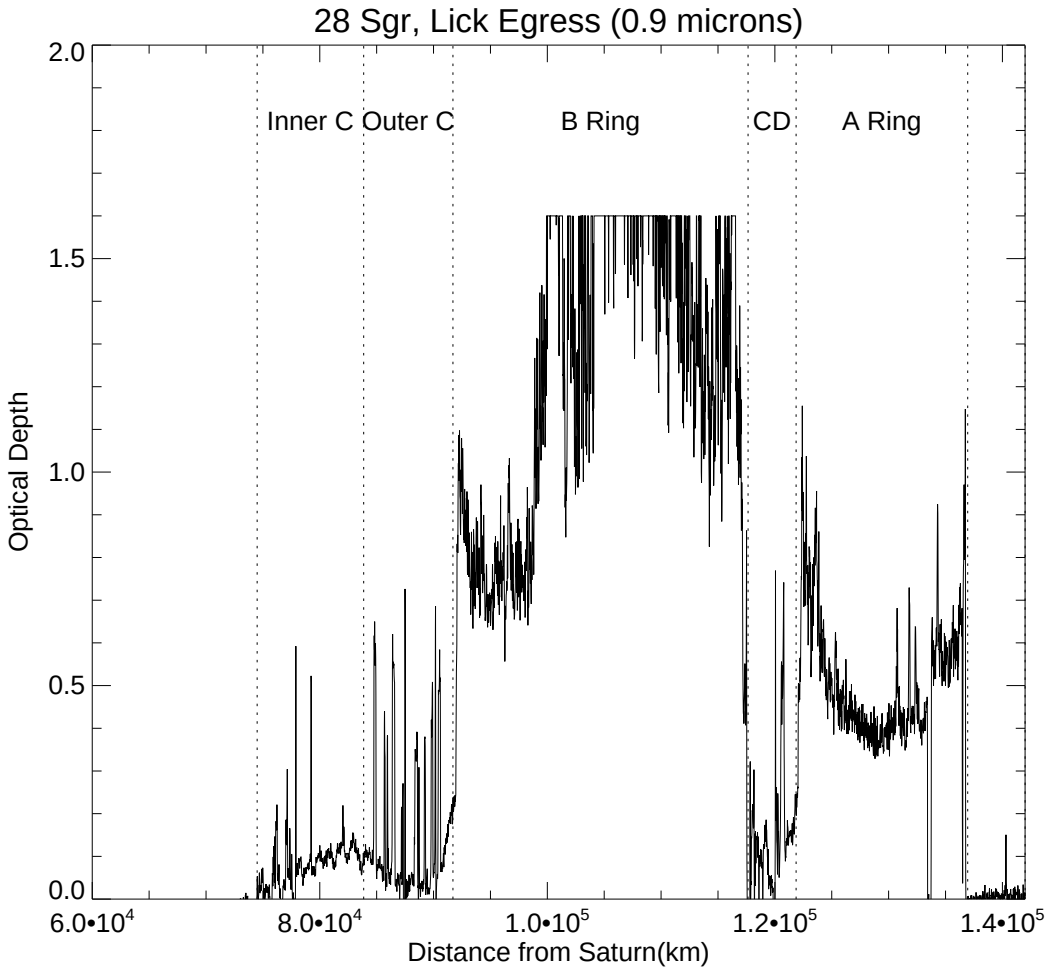

Figure 4.4: The profile of optical depths used for the main-ring model, taken from an observation of the occultation of the star 28 Sgr by the rings (Nicholson et al., 2000). In this plot is cut off at $\tau = 1.6$, which is the maximum detectable optical depth in the Lick egress data. The affected regions in the B ring are all optically thick, so the exact value of τ is not important for calculating the I/F near RPX. (See Section 2.2.2.)

Table 4.3: Single-scattering albedoes for the main rings based on 0.5-μm Voyager observations.

Ring Region	Inner Radius (kkm)	Outer Radius (kkm)	Single-Scattering Albedo[a]	Reference
C ring (inner)	74.5	83.9	0.18	Cooke (1991)
C ring (outer)	83.9	91.7	0.31	Cooke (1991)
B ring	91.7	117.6	0.66	Doyle et al. (1989)
Cassini Division	117.6	121.9	0.38	Smith et al. (1981)
A ring	121.9	136.9	0.6	Dones et al. (1993)

[a]Scaled up by a factor of 1.2 based on the ring spectrum of Karkoschka (1994) for λ=0.5 and 0.89 μm.

4.5.2 The Single-Scattering Albedoes and Phase Function of the Main Rings

The nominal single-scattering albedoes used in the main-ring model, listed in Table 4.3, are derived from Voyager clear-filter observations. For our model, which seeks to reproduce the ring brightness at 0.89 μm, we have scaled these albedoes up by a factor of 1.2, based on the full-ring spectrum of Karkoschka (1994), neglecting small differences in the spectra of the different regions of the rings.

In the Voyager observations, which span phase angles of 6°–155°, the rings obey a power-law phase function which is suitable for macroscopic particles:

$$P(\alpha) = c_n(\pi - \alpha)^n, \tag{4.35}$$

where c_n is a normalization constant. The phase function of the A ring is similar to

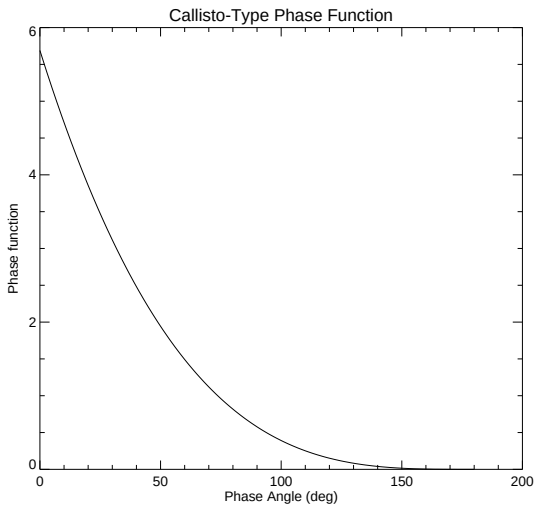

Figure 4.5: The phase function used for main-ring particles, given in Eq. 4.35, is a power-law phase function that was derived by (Dones et al., 1993) from the phase curve of the satellite Callisto.

the phase function of Callisto, with $n = 3.301$ and $c_n = 0.130$. (Dones et al., 1993) This is the phase function we adopt for the main rings. It is plotted in Fig. 4.5.

4.5.3 The Single-Scattering Albedo and Phase Function of the F ring

For the F ring, the single-scattering albedo, ϖ_0, and phase function, $P(\alpha)$, are taken to be uniform throughout the F ring. We will set $P(\alpha)\varpi_0 = 1$ until a reasonable value can be calculated by comparing the model brightness to the observed brightness on the dark side of the rings (see Sec. 4.6.4).

4.5.4 The Optical Depth of the F ring

Each cell in the F ring is assigned a *radial* optical depth according to the formula

$$\tau_r(h) = \tau_0 e^{-(h/h_0)^2}, \tag{4.36}$$

where h is the height above the F-ring plane, τ_0 is the radial optical depth at h=0, and h_0 determines the shape of the vertical profile of the optical depth. These are the two free parameters in our photometric model, and their selection is discussed in detail in Section 4.7.

All pixels in the F ring with a horizontal distance from the center of the planet $u < R_{Sat}$ =60,330 km are set to $\tau_r = 0$ to mask out the area occupied by the planet. Because F ring cells with $\tau_r = 0$ are ignored by most calculations, this results in significant savings in computational time.

4.6 Radiative Transfer

In order to calculate the brightness of the ring system, we much consider the sunlight scattered by the main rings and the F ring, as well as light from the main rings which is scattered by the F ring.

4.6.1 Sunlight Scattered by the Main Rings

A profile of I/F(R) is created by using Eq. 2.38 or 2.39 and the values in Table 4.3, the Callisto phase function which is assumed to be uniform throughout the rings, and $\tau(R)$. Because I/F depends exponentially on τ, we compute I/F(R) using the 28 Sgr optical depths at their full resolution, then smooth the resulting reflectance to the model resolution of 600 km. r_s is calculated for each pixel according to Eq. 4.33 and the pixel is assigned the appropriate I/F($R = r_s$). Multiplying by

Figure 4.6: A model image representing the brightness of the dark side of the rings of Saturn as they appeared at 14:00 UT on 10 August 1995. The horizontal scale in this image is 1200 km/pix, and the vertical scale is 0.156 km/pix. To create this figure, the model image was compressed vertically by a factor of 4.8 and horizontally by a factor of 2. However, compared to the actual appearance of the rings in the sky, the vertical scale is stretched by a factor of 7,700.

the area of a pixel projected on the sky, $A_{pix} = \sigma_u \sigma_v$, gives us the area-integrated I/F, AIF, for each u-v pixel.

Fig. 4.6 shows the relative brightness of different ring regions for the geometry of 14:00 UT on 10 August 1995. The Earth and the Sun are on opposite sides of the ring plane, so we receive only transmitted light (Eq. 2.39). There is almost no light transmitted through regions of high optical depth, such as the A and B rings. The outermost ring of light is the Cassini Division. The inner set of rings is the C ring, which shows the highest transmission in the regions of lowest optical depth. The optical depth and calculated I/F profiles of the C ring are shown in Fig. 4.7. As shown in this plot, the majority of the light transmitted by the C

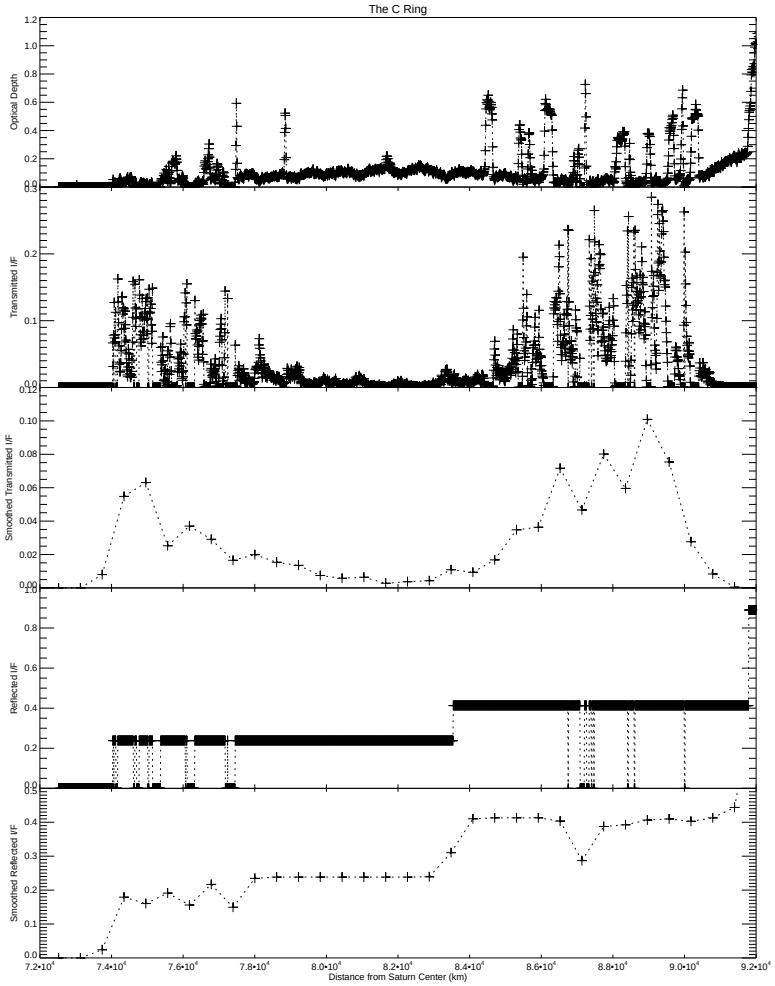

Figure 4.7: The optical depth of the C ring (a subset of the profile of optical depth plotted in Fig. 4.4), the transmitted and reflected I/F of the C ring calculated for $B_e = -0.008°$ and $B_e = +0.008°$, respectively, at the 10 km resolution of the optical depth profile, and each reflectance smoothed to the model resolution of 600 km. Each plus sign indicates one data point. Notice that the majority of the transmitted light passes through narrow regions with very low optical depth, while the reflected light isn't sensitive to τ except where it is nearly zero. The smoothed I/F(R) is used to create the main-ring images (Figs. 4.6 and 4.8).

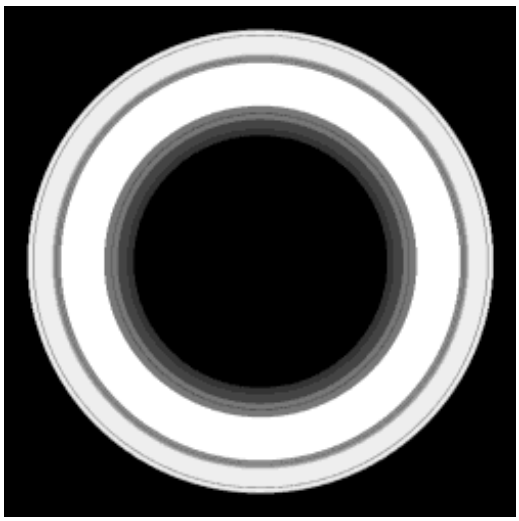

Figure 4.8: A model image representing the brightness of the lit side of the rings of Saturn as they appeared at 1:00 UT on 11 August 1995. The horizontal scale in this image is 1200 km/pix, and the vertical scale is 0.104 km/pix. To create this figure, the model image was compressed vertically by a factor of 3.2 and horizontally by a factor of 2. The vertical scale is stretched by a factor of 11,500 compared to the actual projected height of the rings on the sky.

ring passes through the many narrow regions with very low optical depth in the outer and innermost C ring. Note that the central region of the C ring, with a more slowly varying optical depth of only ~ 0.1 transmits only a small amount of light compared to the outer and inner C ring. At 14:00 UT, B_e=0.0078° and μ=0.00014, and the highest transmission occurs where $\tau = 0.00072$.

Fig. 4.8 is an image of the ring brightness for the lit side, at 25:00 UT. In reflected light (Eq. 2.38) it is the regions of higher optical depth which are brighter. The A and B rings are both optically thick in this geometry (Eq. 2.42), so the fact that the A ring is not quite as bright as the B ring can be attributed to its slightly smaller single-scattering albedo (see Table 4.3). This is true even for the C ring,

where the regions with any significant optical depth are optically thick, as seen in the plateaus in Fig 4.7. The regions with extremely low optical depth are dark, but because they are so narrow, they have little effect on the I/F of the region once it is smoothed to the model resolution. Thus the contrast between the inner and outer C ring are due to the differing albedoes, and for this resolution the C ring's variations in τ have little effect on its appearance on the lit side of the rings. The Cassini Division has an optical depth comparable to the C ring's, so that it appears as a prominent dark region between the brighter A and B rings. At the outer edge of the A ring, the dark Encke Gap is visible. This narrow region does not appear in transmitted light in Fig. 4.6 because, unlike the Cassini Division, it contains so little material that it neither reflects nor transmits a significant amount of light.

We have considered the contribution of saturnshine to the brightness of the main rings, and have determined that it is not significant for the 10–11 August observations. The calculation of saturnshine is discussed in detail in Appendix A.

Using the single-scattering albedoes and phase function above, we find that the model main-ring brightness is about twice that measured from the HST images. Because of this, we will later adjust the brightness of the rings so that the total brightness (including the light scattered by the F ring) matches the lit-side brightnesses measured by HST. This process is described in detail in Section 4.6.4

4.6.2 Sunlight Scattered by the F ring

As discussed in Section 2.4.2, the main rings are treated as thin and flat so that $\mu = \sin B_e$ for all points on the ring, but the F ring is modeled as a vertical surface, so

$$\mu \sim \mu_0 = \cos(\theta), \tag{4.37}$$

where θ denotes the longitude in Saturn spherical coordinates. (Recall that θ is measured from the $\hat{x}$ axis, which is the projection of the vector to Earth into the main-ring plane.) The I/F of the F ring due to reflected sunlight is given by Eq. 2.38, where $\tau_r(h)$ is given by Eq. 4.36.

Multiplying by the projected area of the cell, $dA = \frac{h_f}{n_f}\frac{2\pi r_f}{m_f}|\mu|$, yields the AIF of each cell. (We must take the absolute value of the cosine because the θ values for the back of the F ring are between $\pi/2$ and $3\pi/2$.)

The F ring must be collapsed from a three-dimensional model to a two-dimensional image. We first create two separate image layers, each one an $m \times n$ image array, the same size as the main-ring image, with all pixel values set to zero, to hold the back and front halves of the F ring. Each cell's position in (u, v) coordinates is calculated. The AIF of each F ring cell is then added to the appropriate pixel of the front or back u-v image. Coordinate transformations are handled by matrix multiplication which, in IDL, is very fast. However, this projection must be done with a for-loop, which is much slower than an array operation. Applied to the arrays that describe the front half of the F ring ($\frac{3\pi}{2} \leq \theta \leq \frac{\pi}{2}$), this process produces what we refer to as the FF image.

The same process is used to create an image of the sunlight reflected from the back half of the F ring. However, part of the back half of the F ring lies behind the main rings. As was shown in Section 2.1.2, the intensity of light passing through a ring of normal optical depth τ is reduced by a factor of $e^{-\tau/\mu}$, where μ is the cosine of the incidence angle. For the main rings, the ring-opening angle is very small, so $\mu = |sinB_e| \ll 1$ and $\tau/\mu \gg 1$ for all parts of the main rings including the C ring and Cassini Division, where $\tau/\mu \sim 0.02/0.008 = 2.5$. We therefore assume that the light reflected from the back half of the F ring and transmitted through the

main rings is negligible, and to remove this light from the mode, the u-v image of the back of the F ring is multiplied by a main-ring mask which sets pixels of the F ring that are behind the main rings to zero. The resulting image is referred to as the BF image.

4.6.3 Light Blocked by the Front Half of the F ring

Light from the back of the F ring and from the main rings will be attenuated as it passes through the front of the F ring. According to Eq. 2.18, intensity of the light will be reduced by a factor of $e^{-\tau_r(h)/\mu(\theta)}$, where τ_r is the optical depth normal to the vertical surface of the F ring.

Because (u, v) coordinates have already been computed for each F ring cell, we know what pixel lies behind each cell of the front of the F ring. F ring cells are smaller than u-v pixels, and we simply use the (u,v) coordinate of the center of each cell to determine what pixel is behind it. The I/F of the pixel behind each F-ring cell is multiplied by the factor $1 - e^{-\tau_r/\mu}$ to find the $\mathrm{I/F}_b$ that is blocked by the F ring.

The projected area of the F-ring cell is multiplied by this $\mathrm{I/F}_b$ to find the AIF_b absorbed or scattered by the cell. We create another u-v image, also $m \times n$ pixels in size, which we refer to as a *blocked-light image*, with all the pixel values set to zero initially. The AIF_b for each cell in the front of the F ring is then *subtracted* from the u-v pixel upon which the center of the cell falls.

We apply this process separately to the back half of the F ring (already masked by the main rings) and the main rings, obtaining two separate images: the blocked light from the back of the main rings (FBF) and the blocked light from the main rings (FBM).

These images, along with the image of the sunlight scattered from the back of the F ring masked by the main rings(BF), the image of the sunlight scattered by the main rings (MR), and the image of the sunlight scattered by the front of the F ring (BF) are the five component images that make up the photometric model of the ring system. The images could be summed to produce an image of the ring system, but, because images are discarded when they are no longer needed to save memory during a model run, such images are never actually produced.

4.6.4 Rescaling Ring Brightness

To begin a complete model run, each of the components is computed for the dark-side observation times (14:00–20:00 UT). During these times, the brightness contributed by the main ring is much less than the brightness contributed by the F ring, so the profile of the total ring brightness is approximately

$$\mathrm{VIF}_{tot} \approx \mathrm{VIF}_{BF} + \mathrm{VIF}_{FBF} + \mathrm{VIF}_{FF}, \tag{4.38}$$

and also

$$\langle \mathrm{VIF} \rangle_{tot} \approx \langle \mathrm{VIF} \rangle_{BF} + \langle \mathrm{VIF} \rangle_{FBF} + \langle \mathrm{VIF} \rangle_{FF}. \tag{4.39}$$

However, at this point we have not computed the true brightness of the F ring, because we set $P(\alpha)\varpi_0 = 1$. Let these initial model VIFs be represented by VIF$'$. The same factor of $P(\alpha)\varpi_0$ is present in the I/F of sunlight reflected by the front and the back of the F ring. The light from the back of the F ring that is blocked by the front of the F ring also contains the same factor. It is thus present also in the VIF and $\langle \mathrm{VIF} \rangle$ for each of these components. The model values therefore can be scaled by a factor p_f such that

$$\langle \mathrm{VIF} \rangle_{HST} = p_f \langle \mathrm{VIF}' \rangle_{tot}, \tag{4.40}$$

where $\langle \mathrm{VIF} \rangle_{HST}$ is the radially averaged vertically integrated I/F measured for this time from the HST observations.

For orbits with multiple WF3 images, we average together the data points to obtain a single $\langle \mathrm{VIF} \rangle_{HST}$ for each time. Then for each time, we can compute the F ring scaling factor,

$$p_f = \langle \mathrm{VIF} \rangle_{HST} / \langle \mathrm{VIF}' \rangle_{tot}, \tag{4.41}$$

and then average p_f over all the dark-side times.

Each VIF'_{BF}, VIF'_{FBF}, and VIF'_{FF} that has already been computed is multiplied by this average p_f to obtain the final model profiles VIF_{BF}, VIF_{FBF}, and VIF_{FF}. As we go on to model the lit side (22:00–25:00 UT), the average p_f will be used as $P(\alpha)\varpi_0$ for the F ring when computing the I/F.

The brightness of the lit side of the rings includes significant contributions from both the F ring and the main rings. We have determined an empirical value of $P(\alpha)\varpi_0$ for the F ring, but for the main rings, the albedo remains uncertain. We use the nominal values of $P(\alpha)\varpi_0$ described in Section 4.5.2 to compute VIF$'$ for the main ring components, but these must also be corrected by some factor p_m. The total model brightness on the lit side of the rings is then:

$$\mathrm{VIF}_{tot} = \mathrm{VIF}_{BF} + p_m \mathrm{VIF}'_{MR} + \mathrm{VIF}_{FBF} + p_m \mathrm{VIF}'_{FBM} + \mathrm{VIF}_{FF}. \tag{4.42}$$

In order for the model brightness to match the HST brightness,
$\langle \mathrm{VIF} \rangle_{tot} = \langle \mathrm{VIF} \rangle_{HST}$ and

$$p_m = \frac{\langle \mathrm{VIF} \rangle_{HST} - (\langle \mathrm{VIF} \rangle_{BF} + \langle \mathrm{VIF} \rangle_{FBF} + \langle \mathrm{VIF} \rangle_{FF})}{\langle \mathrm{VIF}' \rangle_{MR} + \langle \mathrm{VIF}' \rangle_{FBM}}. \tag{4.43}$$

This factor, averaged over all the lit-side times, is then applied to all VIF'_{MR} and VIF'_{FBM}, including those for the dark-side times.

The factor p_m preserves the main ring profile's shape, which depends on the optical depth profile of the rings and the relative albedoes of the different regions, but allows us to correct empirically for uncertainties in the main ring single-scattering albedoes in the near infrared. The factor p_m also absorbs in a crude way any divergence of the ring's scattering behavior from single-scattering. This would occur, for example, if there were significant multiple scattering, or a dense distribution of the ring particles in space that leads to shadowing of particles.

The F ring's optical depth is low so single-scattering is a much safer assumption. As a result, p_f should give a reasonable measure of the value of $P(\alpha)\varpi_0$ required, with the given parameters h_0 and τ_0, to match the observed brightness of the F ring.

4.7 Principal Model Parameters

Besides the scaling factors p_f and p_m, which are calculated in the course of the model run, there are two fundamental parameters which may be varied in this model: τ_0 and h_0, which characterize the F ring's vertical optical depth profile, as given by Eq. 4.36. The full-width at half maximum of the vertical profile is given by $2\sqrt{\ln 2}\ h_0 = 1.665\ h_0$, and τ_0 is the radial optical depth of the F ring at the F-ring midplane ($h = 0$). In addition to these two parameters, it is also convenient to consider the model ring's equivalent depth, D. For our optical depth profile,

$$\begin{aligned} \mathrm{D} &= \int_{-30\ \mathrm{km}}^{30\ \mathrm{km}} \tau_r(h)dh & (4.44)\\ &= \int_{-30\ \mathrm{km}}^{30\ \mathrm{km}} \tau_0 e^{(h/h_0)^2} dh & (4.45)\\ &= \sqrt{\pi}\ \tau_0\ h_0\ \mathrm{erf}\left(\frac{30\mathrm{km}}{h_0}\right), & (4.46) \end{aligned}$$

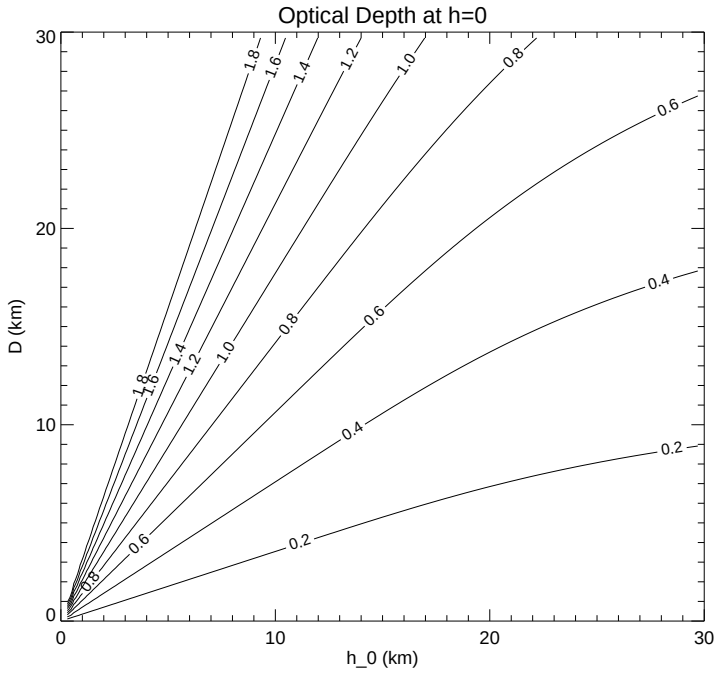

Figure 4.9: τ_0 for a range of values of h_0 and equivalent depth.

where erf(x) is the error function. Thus, given two of the parameters h_0, τ_0, or D, the third can be easily computed. A contour plot of the values of τ_0 for a range of D and h_0 is shown in Fig 4.9. If the optical depth profile extended to infinity, instead of being cut off at $h = \pm 30$ km, the equivalent depth would be $\sqrt{\pi}\tau_0 h_0$.

This model makes the simplifying assumption that $P(\alpha)$ and ϖ_0 are uniform in the F ring, i.e., that the F ring is made of the same type of material throughout. It is then reasonable in this context to take the mass absorption constant, κ, to be uniform also. Thus the variation in $\tau_r(h)$ comes only from the variation of the mass density. We also assume that $\rho(h)$ is azimuthally symmetric, which probably a poor assumption, given the observed clumpiness of the F ring. From Eq. 2.26, then,

$$D = \int_{-30\mathrm{km}}^{30\mathrm{km}} \tau_r(h) dh \tag{4.47}$$

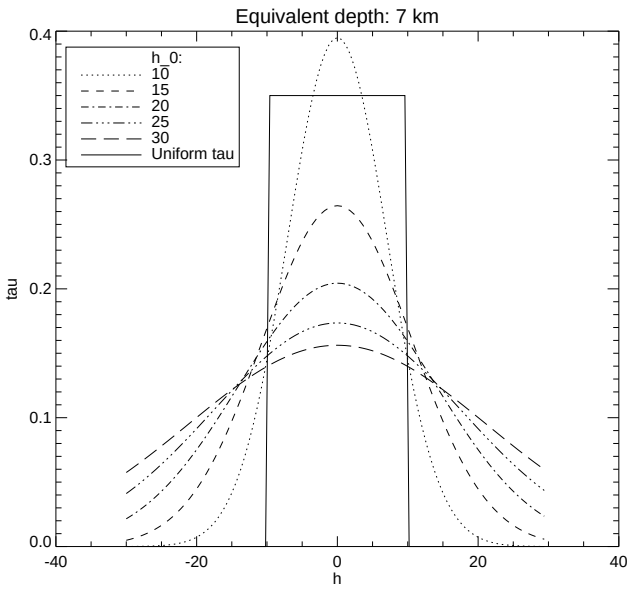

Figure 4.10: Models of the vertical radial depth of the F with varying values of h_0, where τ_0 has been chosen so that each profile has an equivalent depth of 7 km when integrated over the range h=-30 to +30 km. Also shown is a flat profile with the same equivalent depth, similar to the ring of Poulet et al. (2000a).

$$= \kappa \int_{-30\text{km}}^{30\text{km}} \rho(h) dh \tag{4.48}$$

$$= \kappa\sigma \tag{4.49}$$

where σ is the mass per unit arclength of the F ring. Thus we will use D to represent the total amount of matter in the F ring, while h_0 describes its vertical distribution.

Several gaussians of equal equivalent depth are shown in Fig 4.10. Notice that the profiles are cut off at $|h|$=30 km. The larger h_0 is, the flatter the profile, until we approach Poulet's uniform ribbon but with greater vertical cutoffs than Poulet's model ring, which was only 21.4 km tall in its entirety.

The choice of model parameters is constrained somewhat by the known characteristics of the F ring. In occultation events, the equivalent depth has been measured to be between ∼3 and 8 km at infrared wavelengths. These observations were described in Section 3.2.2. The best-fitting model of Poulet et al. (2000a) had an equivalent depth of 8±3 km. There are no direct constraints on h_0 from previous observations, either Voyager imaging or stellar occultations, but a plausible assumption is that the FWHM vertical thickness is no greater than the radial width of the F ring's core, or 20–50 km (Lane et al., 1982; Showalter et al., 1992; Bosh et al., 2002), i.e., $h_0 \lesssim 50\text{km}/1.665 = 30km$. From Fig. 4.9 we can then see that the maximum radial optical depth, τ_0, could range from ~ 0.1 to over 2.

Chapter 5

Application of the Model

Having explained the construction of the photometric model in Chapter 4, we now will interpret the model results by comparing them to the HST observations of the ring-plane crossing of 10 August 1995.

5.1 Products of the Model

In order to determine the F ring model parameters that best reproduce the observed brightness of the rings, we make quantitative and qualitative comparisons to the HST observations by examinging profiles of vertically integrated I/F, averaging these profiles radially to characterize the overall brightness of the rings, and calculating asymmetries between these brightnesses on the east and west ansae. We also calculate a χ^2 statistic in order to represent the degree of agreement between the model asymmetries and the HST asymmetries.

5.1.1 Profiles: VIF(r)

The most basic output of the model is the profile of VIF as a function of horizontal distance from the center of Saturn computed for the time of each set of HST images. The shapes of the profiles can be directly compared to profiles extracted from HST images, revealing the sources of the asymmetry in brightness observed in the HST data, as well as differences between the model and data which may suggest improvements that could be incorporated into a future model.

5.1.2 Brightness Variation with Time: ⟨VIF⟩ vs. t

The total brightness of each ansa of the rings is characterized by averaging the brightness profiles, VIF(r), over the radial range r =80,000–120,000 km (Nicholson et al., 1996). The observed brightness of the rings as a function of time was one of the most important results of the HST observations of the ring-plane crossing. We have reproduced this plot and corrected a calibration error in Figs. 3.4 and 3.5. We also produce similar plots for our model results for comparison with the HST data.

5.1.3 Asymmetries: Δ⟨VIF⟩

Because we chose the factor p_f for the F ring to match the observed ⟨VIF⟩ on the dark side and p_m for the main rings to match the observed ⟨VIF⟩ on the lit side, the overall model brightness will of course be similar to the HST measurements. The models will instead be judged on how well they reproduce the asymmetry between the east and west ansae.

To characterize the asymmetry we compute the difference between the radially averaged VIF of the east and west ansae,

$$\Delta\langle \mathrm{VIF} \rangle = \langle \mathrm{VIF} \rangle_E - \langle \mathrm{VIF} \rangle_W, \tag{5.1}$$

for each time for the model. For comparison with the model results, we also compute $\Delta\langle \mathrm{VIF} \rangle_{HST}$ for each WF3 image, or the average of the two WF3 images when there are two in a given HST orbit.

We can compare the model asymmetries visually with the HST asymmetries by plotting $\Delta\langle \mathrm{VIF} \rangle$ and $\Delta\langle \mathrm{VIF} \rangle_{HST}$ vs. time. Several different models that use

different optical parameters for the F ring can be plotted on the same graph for comparison with each other and with the HST asymmetries.

5.1.4 Overall model fit: χ^2

To judge the model overall, we compute an unweighted chi-square statistic:

$$\chi^2 = \sum_t (\Delta\langle \mathrm{VIF}\rangle_t - \Delta\langle \mathrm{VIF}\rangle_{HST,t})^2, \tag{5.2}$$

summing over each of the model times. There is one data point per HST orbit, and all data points are weighted equally. The smaller the value of χ^2, the better the model fits the data. In general we choose to compute χ^2 over only the data points on the lit side, because the HST asymmetries on the dark side are small, and the model turns out to reproduce them poorly.

5.2 Ring Albedo Scaling Factors

As previously discussed in Section 4.6.4, the factor $p_f = P(\alpha)\varpi_0$ for the F ring is chosen so that the $\langle \mathrm{VIF}\rangle$ averaged over all dark-side data points matches the average of all the HST dark-side $\langle \mathrm{VIF}\rangle$s while the main-ring scaling factor p_m is chosen so as to match the average lit-side $\langle \mathrm{VIF}\rangle$. Figure 5.1 shows the resulting values of p_f and p_m for a range of values of h_0 and D.

5.2.1 F Ring Albedo

The smaller the F ring's equivalent depth, the less material is present in the ring and the greater p_f must be for the F ring to reflect enough sunlight to match the HST dark-side observations. This is illustrated in Fig. 5.2, which shows two vertical reflectance profiles, I/F(h), calculated by Eq. 2.38 using gaussian optical

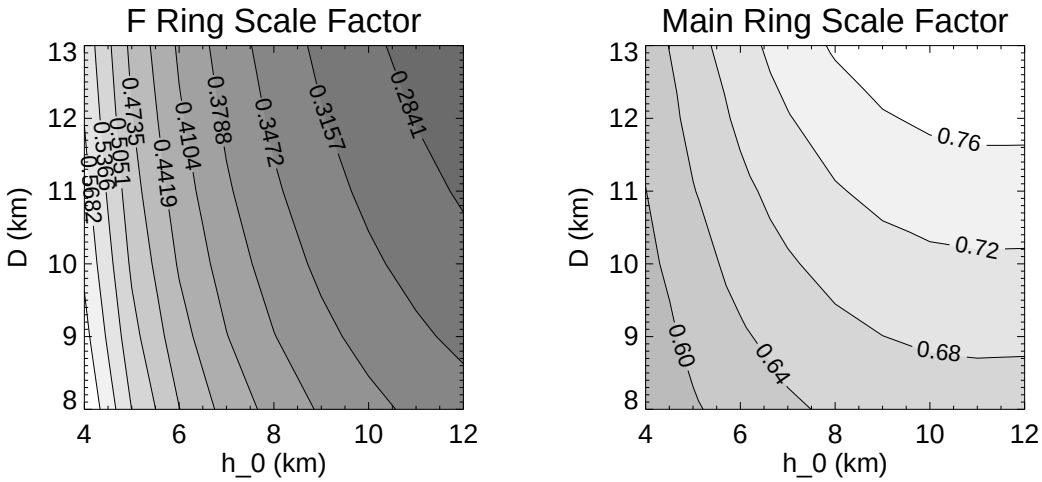

Figure 5.1: Scaling factors for the F ring and main rings from the photometric model. The F-ring factor is $p_f = P(\alpha)\varpi_0$, while for the main-ring the scaling factor, p_m is applied to the $P(\alpha)\varpi_0$ computed using the Callisto-type phase function (Eq. 4.35), the Voyager albedoes (Table 4.3), and the spectrum of Karkoschka (1994).

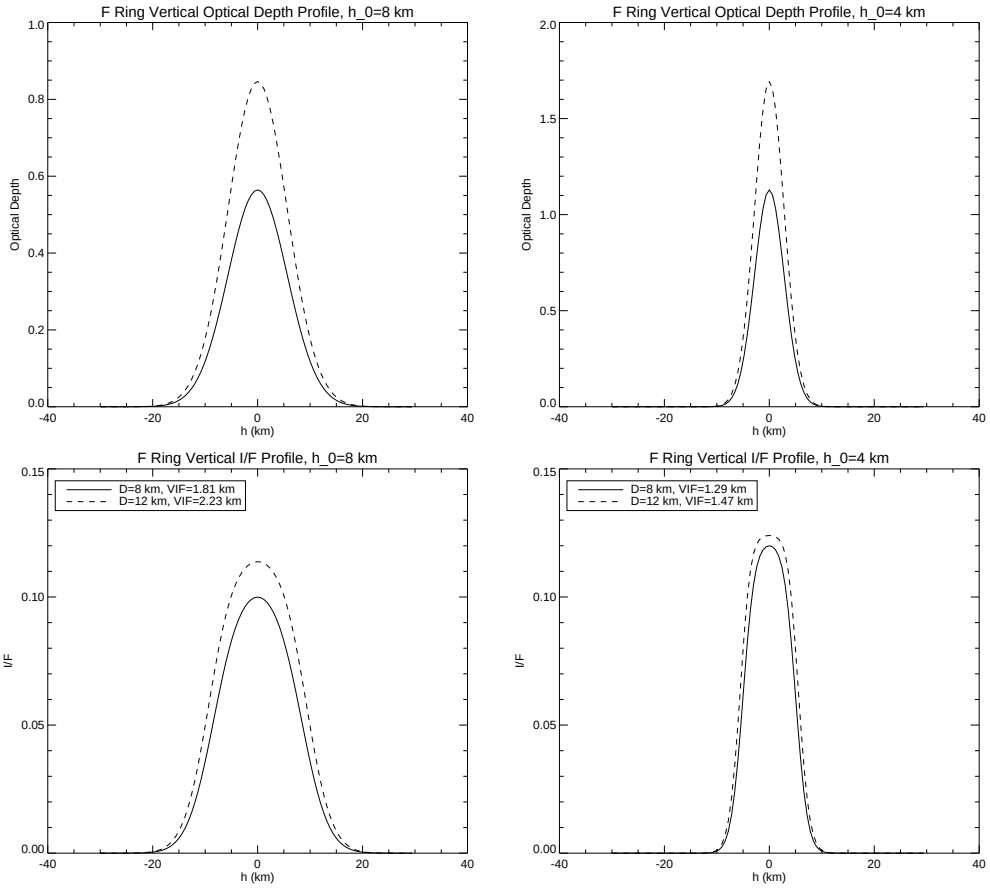

Figure 5.2: Profiles of $\tau_r(h)$ and I/F(h) for the F ring. The reflectance was calculated for r=100,000 km with $p_f = 1$. The VIF of each I/F profile is given in the legend.

depth profiles (Eq. 4.36) for $h_0 = 8$ km and D=8 and 12 km. For these calculations, we chose r=100,000 km ($\mu = \cos 45.4°$) and set $p_f = P(\alpha)\varpi_0 = 1$. We integrated over each profile to find its VIF=$\int I/F dh$. Clearly if both profiles are scaled to match the same VIF$_{HST}$, the profile with the smaller equivalent depth will require a greater p_f, and we would expect p_f to vary inversely with D. This is the general trend shown in Fig. 5.1 for larger values of h_0.

However, for smaller values of h_0, p_f has a much weaker dependence on D in Fig. 5.1. This is because, for a given equivalent depth, a smaller h_0 means that the F ring's mass is more concentrated near the F-ring plane (h=0), where τ can approach or exceed unity. The central part of the F ring thus approaches the optically thick limit, and increasing τ_0 results in only an incremental increase in I/F(0). This is shown in the second set of profiles in Fig 5.2 which have $h_0 = 4$ km, but with the same equivalent depths. Note the relatively flatter peak of the I/F profile for D=12 km, and the more modest increase in VIF between the profiles compared to that for the profiles with $h_0 = 8$ km.

In Fig. 5.3 we also compare vertical I/F profiles for D=10 km and h_0=6 and 10 km. The profile with the larger h_0, and thus the smaller τ_0, yields a larger unscaled VIF, requiring a smaller p_f to match VIF$_{HST}$. We would expect, then, a slight decrease in p_f for larger values of h_0 in the model.

Instead, with increasing h_0, p_f decreases markedly in Fig. 5.1. This is due to the blocking of the back of the F ring by the main rings, which significantly reduces the brightness of the back of the F ring. The smaller the value of h_0, the more F ring material is concentrated behind the main rings on the west ansa, and the more dramatic the blocking effect. Fig 5.4 shows the difference between the model brightness of the front of the F ring ($\langle \text{VIF} \rangle_{FF}$) and the brightness of the back of

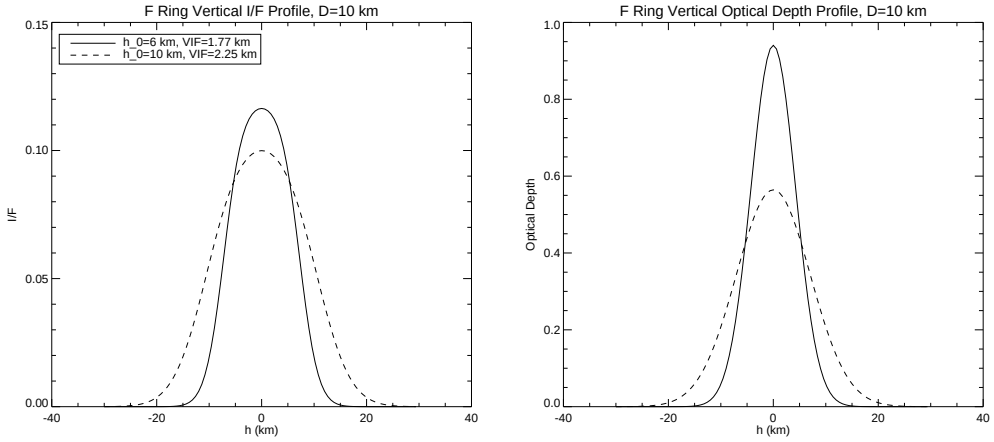

Figure 5.3: Profiles of I/F(h) and $\tau_r(h)$ for model F rings with differing h_0. The reflectance profiles are calculated for r=100,000 km with $p_f = 1$. The VIF of each I/F profile is given in the legend.

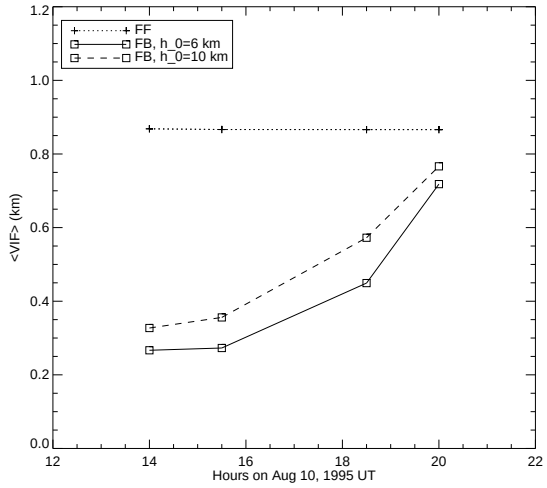

Figure 5.4: Model results showing $\langle \mathrm{VIF} \rangle_{FB}$ for the west ansa before the ring-plane crossing. For h_0=6 km, the F ring mass is more concentrated in the central region, leading to a greater degree of blocking by the main rings on the west ansa than when the mass is more evenly distributed, as for h_0=10 km. Both values of h_0 essentially have the same $\langle \mathrm{VIF} \rangle_{FF}$ for each time.

the F ring blocked by the main rings ($\langle \mathrm{VIF} \rangle_{FB}$) on the west ansa for D=10 km and h_0=6 and 10 km. (The brightness of the back of the F ring on the east ansa is almost equal to the brightness of the front of the F ring because there is very little blocking by the east ansa of the main rings, and the brightness of the front of the F ring on the east and west ansae for both values of h_0 is similar.) We can see that a smaller h_0 leads to a greater degree of light blocked by the main rings, requiring a larger p_f to achieve the average HST dark-side brightness.

For the wide array of values of h_0 and D tested in our model, p_f ranges from 0.23–0.84, with the $p_f = 0.36$ for our best-fit model. Poulet et al. (2000a) do not quote values for $P(\alpha)\varpi_0$, but based on their plotted results, we estimate that the fitted value for the final model was $\sim$0.6. However, the treatment of the geometry of the F ring in the Poulet model was very elementary, and the derived brightness of the rings assumed that the back of the F ring lay entirely behind the front, effectively doubling the radial optical depth of the ring. By contrast, the geometry of our model shows that, especially before the ring-plane crossing, significant parts of the back of the F ring are unobstructed by the front of the F ring, so instead of doubling the optical depth, we effectively double the projected height of the ring. Both the current model and the Poulet model seek to reproduce the VIF of the F ring in the same dark-side HST observations. Because the effective height of the F ring is doubled in our model, we find that F ring only needs to have approximately half the reflectivity.

5.2.2 Main Ring Albedo

The main-ring brightness is scaled by the factor p_m to match $\langle \mathrm{VIF} \rangle_{HST}$ on the lit side. We note that p_f has already been set to give the F ring a total average

dark-side brightness of $\langle \mathrm{VIF} \rangle \approx 1.4$ km. The contribution of sunlight reflected from the F ring on the lit side of the rings remains similar and is about equal to of the contribution from the main rings at 22:00 UT.

As the main-ring brightness increases, the front of the F ring blocks a significant amount of light from the main rings. The greater the blocking by the F ring, the larger p_m must be so that the total brightness of the rings matches the HST value. Increasing D increases the amount of blocking by the F ring by increasing its overall optical depth.

Again, however, h_0 has a surprisingly large influence on the F ring's photometric behavior due to the effect of saturation as τ_0 approaches unity. A smaller h_0 confines more F-ring material to an optically thick core, which results in only a modest increase in the blocking by the front of the F ring as D increases. Larger values of h_0 mean that the material is spread further over the optically thin outer envelope, where the increase in τ with increasing D will lead to a significant increase in the amount of main ring light blocked by the front of the F ring.

Thus p_m increases with both h_0 and D as shown in Fig. 5.1. We find that for our best-fitting model, the main rings are about 70% as bright as predicted by single scattering using the nominal photometric parameters discussed in Section 4.5.2.

Figure 5.5: Model profiles of VIF(r) and corresponding diagrams of the ring geometry. The F ring is depicted in the diagrams as a 10 km-high "ribbon", whereas its full height in the photometric model is 60 km. The total brightness is plotted as a solid gray line. The dash-dot line shows the brightness of the main rings (MR). The dashed line represents the brightness of the back of the F ring, with light blocked by the main rings removed (FB). The dotted line is the profile of sunlight reflected from the front of the F ring (FF). The solid black line represents the blocking by the front of the F ring of the main rings and the back of the F ring (FBF+FBM) and has negative values. The profiles were created with our best-fitting F ring model parameters, h_0=8 km and D=10 km.

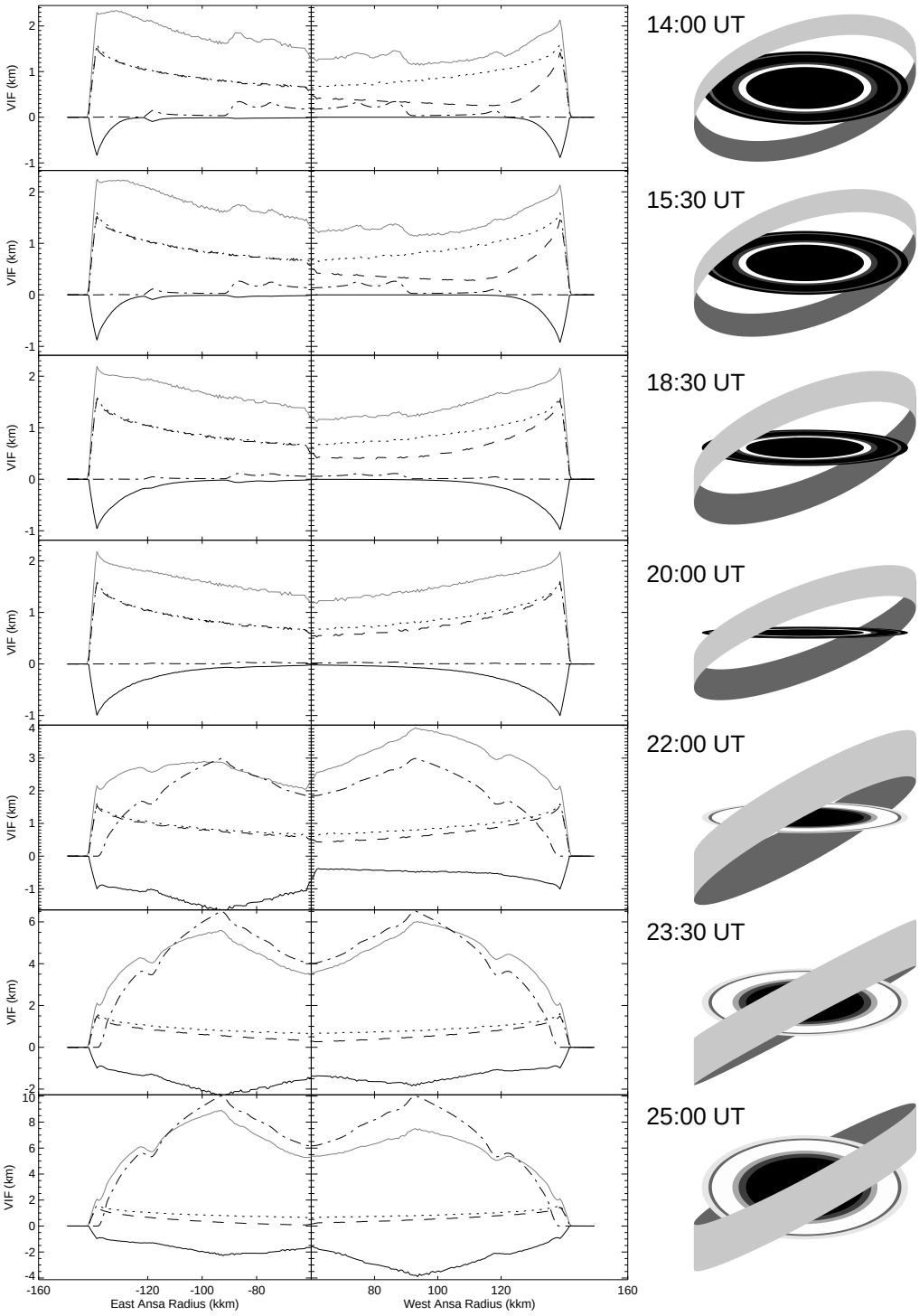
VIF (km)
East Ansa Radius (kkm)
West Ansa Radius (kkm)
14:00 UT
15:30 UT
18:30 UT
20:00 UT
22:00 UT
23:30 UT
25:00 UT

5.3 The Model Profiles in Detail

The most fundamental of the model results are profiles of VIF(r). Not only can the total model profile be compared with the HST data, but we also have profiles extracted from the different component images in the photometric model to illustrate the role of the main rings and F ring in producing the total profile. These component and total profiles are shown along with diagrams depicting the geometry of the rings in Fig. 5.5.

Before the ring-plane crossing at ∼21:00 UT, the sunlight reflected from the F ring dominates the total profile of VIF, contributing VIF∼1.5 km for each ansa, while the sunlight transmitted through the main rings is much weaker. At 14:00 and 15:30 UT, the transmitted light from the C ring contributes a measurable VIF of ∼0.2 km and is visible interior to 90,000 km, while the Cassini Division is marginally detectable at VIF∼0.1 km near 120,000 km. As the RPX approaches, however, the main-ring brightness wanes with the decreasing ring-opening angle to Earth.

The profile representing blocking by the front of the F ring is the sum of the blocked light from the back of the F ring and the blocked light from the main rings and, as in the image components used to construct the model, the values of this profile are negative. On the dark side, most of the blocking by the front of the F ring is of the reflected sunlight from the back of the F ring. This blocking is symmetric east-to-west, and increases as the optical depth along the line of sight increases toward both ansae of the F ring.

As can be observed in the diagram of the rings, the brightest part of the dark side of the main rings, the C ring, is not obscured by the densest part of the F ring before the RPX, but the Cassini Division is obscured by the F ring on the east

ansa. (Note that, whereas the F ring in the photometric model is 60 km in total height, the F ring in the diagram is depicted with a height of only 10 km so that the main rings can be more plainly seen. This narrow band also serves to indicate the position of the densest part of the F ring.)

The major source of asymmetry in the model profiles before the ring-plane crossing is the blocking of the back of the F ring by the west ansa of the main rings. On the east ansa of the dark-side profiles, the profiles of reflected sunlight from the front and back of the F ring are roughly equal, but on the west ansa, the main rings block a significant amount of light from the back of the F ring. The blocking of the back of the F ring by the front of the F ring, by contrast, is nearly symmetric at all times. Our model thus predicts that the total VIF of the rings will be slightly higher on the east ansa prior to RPX.

After the RPX, the brightness of the main rings grows rapidly. So too does the amount of blocking by the front of the F ring. At 22:00 UT, just $\sim$1 hour after the main ring plane crossing, sunlight reflected from the main rings is already comparable in brightness to that reflected from the F ring, and as B_e increases, so does the VIF; by 23:30 UT the light from the main rings dominates the system's brightness. Notice that the F ring's brightness is almost independent of the ring-opening angle.

The asymmetry in the model brightness after the RPX results arises from the differences in the blocking of the sunlit side of the main rings by the front of the F ring. At 22:00 UT, the east ansa of the main rings is obscured by the F ring, particularly the brightest part of the rings, the B ring, while on the west ansa, there is little blocking. At 23:30 UT, near the F-ring-plane crossing, the F ring obscures both ansae to a similar extent. Then at 25:00 UT, the F ring, while still significantly blocking the east ansa, blocks even more light from the west ansa.

Our model can thus potentially account for the reversal of east-west asymmetry noted after the RPX in Figs. 3.4 and 5.7.

5.4 Comparing Model Profiles and HST Profiles

By comparing the model profiles of VIF as a function of horizontal distance from the center of Saturn with profiles extracted from the HST images, we can isolate the regions of the rings responsible for the observed asymmetries. Profiles of VIF(r) from the photometric model with the best χ^2, ($h_0 = 8$ km, D=10 km, see Section 5.6 below) are over-plotted on the average HST profiles in Fig. 5.6. Comparing the shapes of the profiles is more important than comparing their overall brightness, because while the best fit for the model is chosen based on the $\langle$VIF$\rangle$ measured from the WF3 images only, as described in Section 3.1.2, the HST composite profiles were assembled from profiles of both WF3 and PC images which were extracted by McGhee (2000).

Despite its simplicity, our model does a fair job of reproducing the general shape of the HST profiles. Both observed and model profiles of the dark side of the rings are flat, with a slight increase in brightness at the ansa. The shape of the lit-side model profiles are a particularly good match to the HST data. The main rings have been modeled quite accurately, and the light reflected from the F ring at the ansa is quite well reproduced.

However, the asymmetries observed in the brightness of the east and west ansae on the dark side of the rings are overestimated by our model. Also, in the HST profiles we find several features which are not accounted for by the model. All the features discussed below are present in all the profiles that were combined to produce the composite HST profiles, rather than reflecting an anomaly in a single

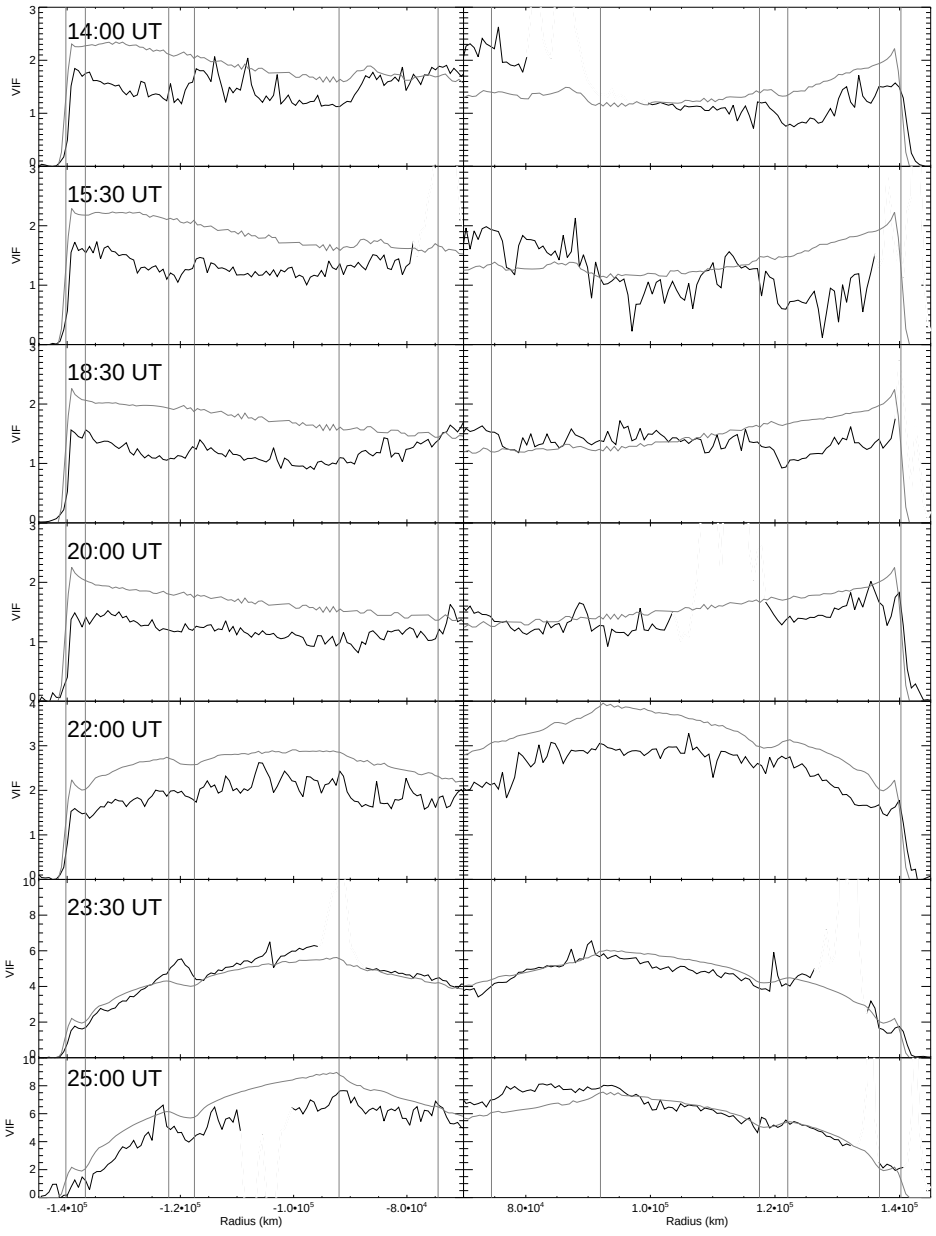

Figure 5.6: Profiles of VIF(r) from the HST data (black line) and from the model (gray line) for the best-fit parameters D=10 km, h_0=8 km. The vertical lines indicate the boundaries of the different ring regions as in Fig. 3.2. Unlike Fig. 3.2, in this figure we have removed the regions in the HST profiles that are contaminated by light from satellites.

image. They are also not due to satellites, which have been largely removed by median-filtering (see Section 3.1.2). (Portions of the profiles where satellites were not removed effectively by filtering have been blanked out in Fig 5.6.) Most of these features are probably a result of azimuthal variation (e.g., clumpiness) in the F ring (which is not included in our F ring model), although we have found it difficult to track these features with the orbital motion of the F ring due to interference from the known moons of Saturn which heavily contaminate the profiles.

5.4.1 Dark-Side Profiles

The model profiles are a fair match to the magnitude of brightness and the generally flat shape of the HST profiles on the dark side of the rings (i.e., 14:00–20:00 UT), and show that the light from the main rings is a trivial contribution, with light transmitted by the C ring dropping below detectability as the ring-opening angle decreases.

On both ansae, the model profiles slope upward toward the ansa with a shape typical of the narrow, optically thin ring discussed in Section 2.4.2. However, the HST profiles are more flat. This may indicate that the brightness of the F ring in this geometry is dominated by a vertically thin, optically thick core, which, seen edge-on would have a flat profile. For an optically thick region, the I/F would not increase toward the ansa because τ/μ would always be at or near 1, so the reflectance would be in the optically thick limit, Eq. 2.42, all the way out to the ansa. If it is azimuthally symmetric, the ring's I/F and height would be independent of r, so VIF(r) would be flat. This is consistent with the F ring's suspected radial structure, with an optically thick core of larger particles (see

Section 3.2.2) and the fact that the larger particles would be backscattering, and would thus reflect a considerable amount of sunlight.

There is poorer agreement in terms of the asymmetry between the ansae, as is also seen in the values of $\langle \mathrm{VIF} \rangle$ (see Fig. 5.7). In the model, the dark-side asymmetry is due to blocking of the back of the F ring on the west ansa by the main rings, which can be seen in the profiles as a depression of the VIF of the F ring on the west ansa. This blocking decreases as the ring-opening angle decreases and is essentially zero at 20:00 UT. In the HST images, this trend is not observed. The asymmetry between the ansae is smaller, and the west ansa is slightly brighter than the east ansa at 18:30 and 20:00 UT.

In the HST profiles, the C ring is visible at 14:00 and 15:30, a feature which is reproduced by our model, as well. (This is shown more clearly in Fig. 5.5.) The C ring's brightness decreases with the ring-opening angle, and it is visible in neither the HST nor the model profiles for 18:30 and 20:00 UT. In many of the HST dark-side profiles there also seems to be a small feature at the radius of the Cassini Division. In the model profiles, the Cassini Division is barely discernible on the west ansa, and there is almost no trace of it on the east ansa where the F ring blocks most of the light from the Cassini Division. It is possible that we underestimate the brightness of the transmitted light through the Cassini Division, but the level of noise in the HST profiles makes a positive identification of this feature uncertain.

In the HST profiles, which are also shown in Fig. 3.3, there is an asymmetry at 15:30 UT, due to a dip of about 0.6 km in the VIF of the west ansa at around $r \sim$130,000 km. In the 14:00 UT profile, a similar but smaller dip may be due to the presence of Mimas in this region. However, there are no large satellites present at this radius in the 15:30 UT profile. The 15:30 UT west ansa profile is

particularly noisy, however, because it is the mean of only two profiles, because a median filtered requires three or more profiles.

The dip is outside the C ring and Cassini Division, in the part of the profile where the A ring will dominate in the lit-side profiles, but of course at this time the A ring contributes no measurable brightness. This dip could be due to a region of lower optical depth in the F ring, which would cause it to reflect less sunlight. However, such a feature should orbit with the F ring, and it would have had to originate at $r \sim 70,000$ km at 14:00 UT in order to arrive at $r \sim 127,000$ km at 15:30 UT if it were on the front half of the F ring. If it were on the back half of the F ring, it would have traveled from its location at 15:30 UT to the inner edge of the C ring at 20:00 UT, but there is no trace of it in that profile.

Luckily, the dip lies mostly outside the region over which the VIF is averaged to find $\langle \text{VIF} \rangle$, so as we evaluate the model by its agreement to $\Delta\langle \text{VIF} \rangle$, this is irrelevant. Instead, it is fairly subtle differences in brightness at smaller radii that result in the very small asymmetries measured in the HST data for these times.

At 18:30 UT, there is an asymmetry of VIF$\sim$0.3 km in the region from 85,000–110,000 km, where either the east ansa brightness is depressed or the west ansa brightness is enhanced, or both. Again, since this region is largely outside the C ring, and the narrow Cassini Division is highly unlikely to contribute any appreciable brightness, the variation seems likely to be due to azimuthal variation in the F ring. The F-ring clumps 1995 S7 and S9 are present in this region (McGhee et al., 2001) but would not necessarily be expected to contribute a broad enhancement to the ring brightness. The difference is subtle, and it is not clear whether it is the east ansa or the west ansa that is anomalous, so we do not attempt to track the orbital motion of any putative F ring features in this case.

In the 20:00 UT profile, the two ansae are roughly symmetric in both the HST data and the model.

It is to be expected that the model, with its azimuthally symmetric F ring, is unable to reproduce some of the asymmetries observed on the dark side of the rings. The HST profiles do not clearly show the expected asymmetry due to the blocking of the back of the F ring by the main rings. This blocking, $\lesssim 0.5$ km of the total VIF, may just be lost in the "noise" of the F ring's azimuthal variation.

5.4.2 Lit-Side Profiles

After ∼21:00 UT, sunlight reflected from the main rings dominates the ring brightness, and the asymmetry is primarily due to blocking of their light by the front of the F ring. With a few small exceptions, the model matches the shape of the HST profiles well.

At 22:00 UT, the model profiles show that the west ansa is brighter than the east ansa, because the dense central region of the F ring lies right across the east ansa but falls north of the west ansa (see Fig. 5.5). The overall VIF of the HST profiles is ∼0.5 km less than the predicted values at this time but this is mostly because the bulk of the HST images were taken a few minutes before 22:00 UT, the time chosen to represent this HST orbit in the model, and the main rings are opening rapidly (see Fig. 3.4). The overall asymmetry and shape of the profiles are reproduced well. This includes the maximum in VIF at the inner boundary of the B ring, a slight dip at the Cassini Division, and the small peak at the radius of the F ring on both ansae. The east ansa is flatter than the west ansa because of the blocking of the B-ring region at this time (see Fig. 5.5). There were no bright satellites present in these images, making this the cleanest set of lit-side profiles.

The model fit for 23:30 UT, near the time of the F-ring-plane crossing, is also quite a good match to the HST data.

At 25:00 UT, considering the noisiness of the east ansa profile, which is made from the mean of only two profiles and contaminated by a bright satellite, the agreement in the general shape of the profile is fair. The agreement between the model and the profile on the west ansa is very good, except in the inner C ring, where the HST VIF is $\sim$ 1 km greater than the model. If this is an enhancement in the brightness of the F ring, then one would expect it to be a prominent feature in the other profiles. If it were on the back half of the F ring, it would be visible as an enhancement at the end of the east ansa in the images at 22:00 UT and 23:30 UT. If it were on the front half of the F ring, it would have been on the east ansa and visible in the profiles from 18:30–22:00 UT. Its absence in the dark-side profiles rules out this hypothesis, because the F-ring brightness is largely unaffected by the ring-opening angle, and a $\sim$0.5 km feature would stand out distinctly in the dark-side profiles.

It is more likely that this increased brightness is due to a region of *low* optical depth in the F ring, allowing more light from the main rings to shine through. To estimate the decrease in optical depth that would be necessary to produce this feature, recall that the profile of brightness for the model can be expressed as the sum of the profiles of the model components:

$$\mathrm{VIF}_M = \mathrm{VIF}_{MR} + \mathrm{VIF}_{FB} + \mathrm{VIF}_{FF} + \mathrm{VIF}_{FBF} + \mathrm{VIF}_{FBM}. \tag{5.3}$$

Let us assume that there is some average optical depth, τ_M, that can represent the overall degree of blocking by the F ring, so that

$$\mathrm{VIF}_{FBF} \approx -(1 - e^{-\tau_M})\mathrm{VIF}_{FF} \tag{5.4}$$

and

$$\mathrm{VIF}_{FBM} \approx -(1 - e^{-\tau_M})\mathrm{VIF}_{MR}. \tag{5.5}$$

(See Section 4.6.3.) Using a single τ_M is a poor approximation, because the optical depth of the F ring varies with height and the optical depth of the portion of the F ring that obscures the main rings will be different from the portion that is blocking the back of the F ring, so this calculation should only be taken as a crude estimate. Applying these approximations, we have

$$\mathrm{VIF}_M \approx \mathrm{VIF}_{MR}e^{-\tau_M} + \mathrm{VIF}_{FB}e^{-\tau_M} + \mathrm{VIF}_{FF}. \tag{5.6}$$

Solving for the optical depth,

$$\tau_M = \ln\left(\frac{\mathrm{VIF}_{MR} + \mathrm{VIF}_{FB}}{\mathrm{VIF}_M - \mathrm{VIF}_{FF}}\right). \tag{5.7}$$

For the component model profiles at r=80,000 km, VIF_{MR}=8 km, VIF_{FB}=0.3 km, VIF_{FF}=0.7 km, VIF_M=6.3 km, so the average line-of-sight optical depth for the model is characterized by the figure τ_M=0.39. This is a reasonable value, given that the maximum radial optical depth in the F ring is $\tau_0 = 0.71$ for this set of model parameters.

The F ring is mostly optically thin, so for $\tau_M \ll 1$, we can also rewrite Eq. 5.6 as

$$\mathrm{VIF}_M \approx \mathrm{VIF}_{MR}(1 - \tau_M) + \mathrm{VIF}_{FB}(1 - \tau_M) + \mathrm{VIF}_{FF}. \tag{5.8}$$

Because the model profile is a good match to the HST profile outside of the C ring region, the model components VIF_{MR} and VIF_{FB} are probably a good representation of the actual brightness of the rings. However, we suspect that the *true* optical depth of the part of the F ring that falls in front of the C ring region is lower than the optical depth of the model F ring. We represent this actual optical

depth as an average line-of-sight F-ring optical depth τ_H which we estimate from the HST profile. This optical depth will influence not only the blocking by the front of the F ring, but also its brightness in reflected light. We can again exploit the fact that the F Ring is largely optically thin and use the approximation in Eq. 2.40 and express the brightness of the front of the F ring for the HST profile as

$$\mathrm{VIF}'_{FF} \approx \frac{\tau_H}{\tau_M}\mathrm{VIF}_{FF}. \tag{5.9}$$

Just as the model profile was approximated as Eq. 5.8, the HST profile is approximately:

$$\mathrm{VIF}_H \approx \mathrm{VIF}_{MR}(1-\tau_H) + \mathrm{VIF}_{FB}(1-\tau_H) + \frac{\tau_H}{\tau_M}\mathrm{VIF}_{FF}. \tag{5.10}$$

Then subtracting Eqs. 5.10 and 5.8, the difference between the HST profile and the model profile is

$$\mathrm{VIF}_H - \mathrm{VIF}_M \approx (\tau_M - \tau_H)(\mathrm{VIF}_{MR} + \mathrm{VIF}_{FB} - \frac{1}{\tau_M}\mathrm{VIF}_{FF}). \tag{5.11}$$

Solving this expression for the HST general optical depth gives:

$$\tau_H \approx \tau_M - \frac{\mathrm{VIF}_H - \mathrm{VIF}_M}{\mathrm{VIF}_{MR} + \mathrm{VIF}_{FB} - \frac{1}{\tau_M}\mathrm{VIF}_{FF}}. \tag{5.12}$$

At r =80,0000 km,VIF_H=7 km, so τ_H ≈0.28. This shows that the feature in the C ring at 25:00 UT can be produced by a region of the F ring whose optical depth is approximately 70% of the F ring average, which is well within the observed range of azimuthal variation in the F ring (Showalter et al., 1992).

Unfortunately, due to the noise in the profiles and the presence of contaminating satellites, we were unable to definitively identify this feature in any other profiles, but neither can we definitively rule out its presence. While we do not purport to have proved the existence of this particular region of low optical depth in the F ring,

this calculation may serve as a rough estimate of the sort of large-scale variation in τ that might appear in the F ring and its effect on the observed profiles.

5.5 The Change in Ring Brightness over Time

To find $\langle \mathrm{VIF} \rangle$, we average the model $\mathrm{VIF}(r)$ over the range r =80,000–120,000 km, choosing the same range as was used by Nicholson et al. (1996) so that the results are directly comparable. Fig. 5.7 shows typical model along with the $\langle \mathrm{VIF} \rangle$ from each ansa of each WF3 HST image. To eliminate any potential problems stemming from the relative calibration of images from the two chips, the PC data are not considered in this discussion.

Before the ring-plane crossing, the average model brightness of all dark-side data points (including the east and west ansae) matches the average HST brightness becasuse we scale the albedo of the model F ring. However, it is clear that the asymmetry in the model data does not match the asymmetry in the HST data. In the dark-side model data, the east ansa is consistently brighter than the west ansa, due to blocking of the back of the F ring by the west ansa of the main rings. As the ring-opening angle decreases with time, the projected area of the main rings decreases, and thus the blocking of the west ansa of the F ring decreases. By contrast, in the HST data, at 14:00 UT, the magnitude of the model asymmetry is somewhat larger than the HST asymmetry. At 15:30 UT the HST asymmetry decreases to nearly zero. After this, at 18:30 UT and 20:00 UT, the asymmetries are very small, and their sense is reversed, with the west ansa brighter than the east ansa. It is apparent that the mechanism responsible for the model asymmetries on dark side is not the cause of the actual observed asymmetry.

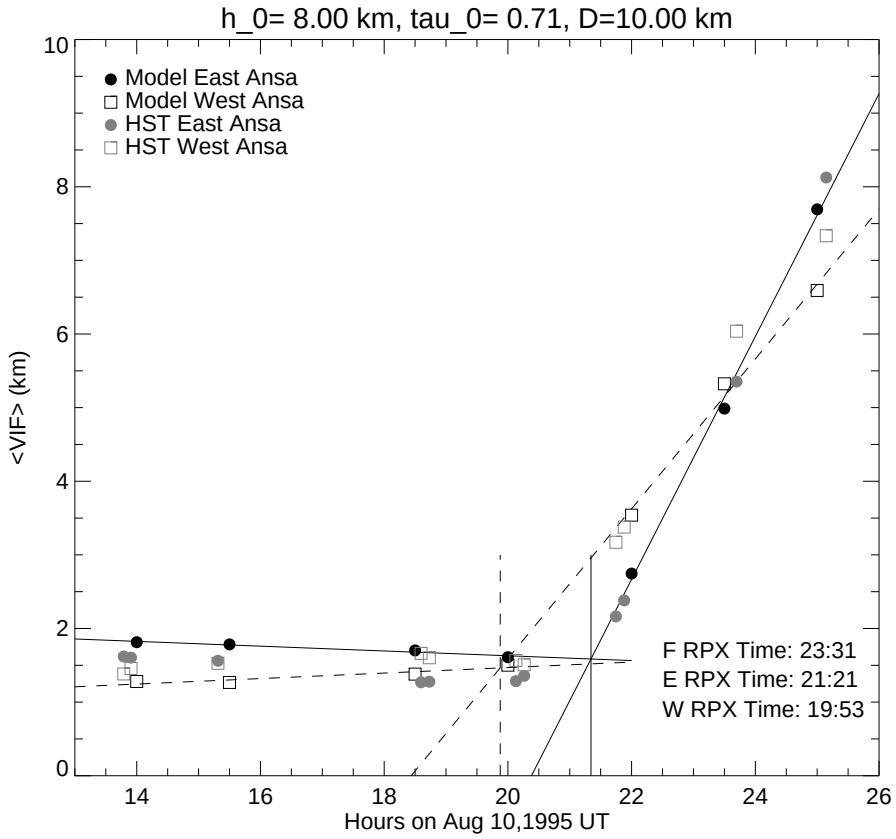

Figure 5.7: ⟨VIF⟩ as a function of time, showing the model results (black) and the HST data (gray). The intersections of separate linear fits to the model brightness before and after the RPX are used to calculate a RPX time for each ansa, and the intersection of the east and west ansa fits on the lit side gives the FRPX time (see Appendix B.)

On the lit side, however, the model provides a good match to the HST data. At 22:00 UT, the west ansa is brighter than the east ansa in both the model and the data, and by about the same amount. At 23:30 UT, the west ansa is still brighter, but the amount of the asymmetry has decreased. At 25:00 UT, the east ansa is brighter than the west ansa, and the asymmetry is large once again.

Following Nicholson et al. (1996), we do a linear fit to the data from each ansa, fitting the data before and after the RPX separately. The intersection of these fits gives a separate main ring RPX time for each ansa. We find a ring-plane crossing time of 19:53 UT for the west ansa and 21:21 UT for the east ansa. As discussed previously in Section 3.1.2, from the WF3 HST data, we find a west-ansa crossing time of 20:25±10 min and an east-ansa crossing time of 21:13±3 min. The model RPX times differ significantly from the HST times due to the failure of the model to reproduce the change in brightness with time of the rings before the ring-plane crossing.

We also compute the intersection of the east and west ansa lit-side linear fits to find the crossing time for the F ring plane as discussed in Appendix B.

5.6 Best-Fit Parameters and Their Uncertainties

For each pair of model parameters that was tested, the results of the photometric model were judged by computing an unweighted χ^2,

$$\chi^2 = \sum_t (\Delta\langle \mathrm{VIF} \rangle_t - \Delta\langle \mathrm{VIF} \rangle_{HST,t})^2, \tag{5.13}$$

where the sum is taken over only the lit-side model times. A contour plot showing the values of χ^2 that result from models with a range of h_0 and D is shown

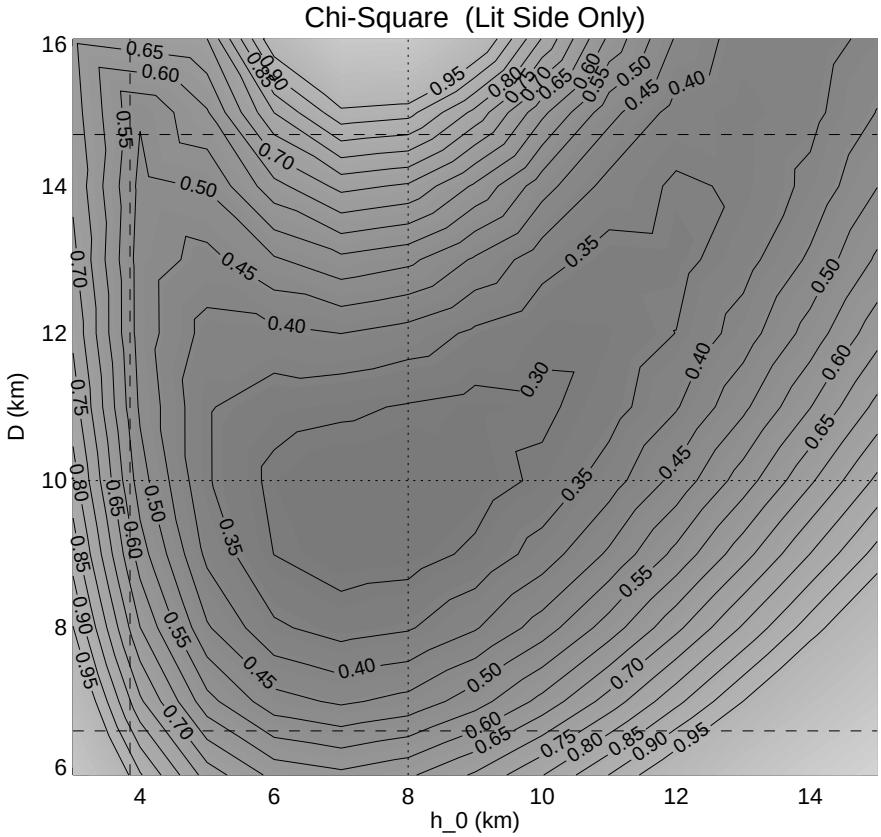

Figure 5.8: Unweighted χ^2 values for a range of values of model parameters h_0 and D. The dotted lines indicate the position of the best fit, for $h_0 = 8$ km and $D = 10$ km. The dashed lines show the projection of the 1-σ contour, where χ^2=0.5, onto the h_0 and D axes. Because this contour does not close at the upper right, we use the bounds at the left-hand side to characterize the uncertainty in the model parameters.

in Fig. 5.8. The minimum unweighted chi-square is $\chi^2_{min} = 0.26$ km^2, which is obtained for $h_0 = 8$ km and $D = 10$ km.

It would be preferable to use a weighted chi-square that takes into account the standard deviations for each data point, σ_t:

$$\chi^2_w = \sum \left(\frac{\Delta\langle \mathrm{VIF} \rangle_t - \Delta\langle \mathrm{VIF} \rangle_{HST,t}}{\sigma_t} \right)^2 \tag{5.14}$$

(Press et al., 1992). However, Nicholson et al. (1996) do not quote standard deviations for their $\langle$VIF$\rangle$s. Uncertainties for the HST asymmetries based on the scatter of the HST measurements for each orbit are given in Table 3.1.2, but it must be stressed that these include both WF3 and PC images, whereas $\Delta\langle \mathrm{VIF} \rangle_{HST}$ is computed from WF3 images only. However, these errors can serve as an indicator of the general level of uncertainty in the HST measurements, which is dominated by systematic errors associated with the effects of superimposed satellites and F-ring clumps, rather than statistical (i.e., photon) noise.

Lacking rigorous standard deviations for the data, we can assume that a typical uncertainty in the HST asymmetries is represented by σ, so that

$$\chi^2_w = \frac{1}{\sigma^2} \sum_t (\Delta\langle \mathrm{VIF} \rangle_t - \Delta\langle \mathrm{VIF} \rangle_{HST,t})^2, \tag{5.15}$$

or

$$\chi^2_w = \frac{\chi^2}{\sigma^2}. \tag{5.16}$$

The minimum of a weighted chi-square for a reasonable model fit should be approximately equal to the degrees of freedom, so in this case, because we use the three lit-side data points to determine the two model parameters, we should have $\chi^2_{w,min} = 1$ (Press et al., 1992). This suggests that $\sigma = \sqrt{\frac{\chi^2_{min}}{1}} = 0.5$ km, which is in good agreement with the estimated HST uncertainties in Table 3.1.2. As a test, we also computed a weighted χ^2 statistic by using the standard deviations

for each HST data point in Eq. 5.14. The results are not very different from the unweighted χ^2, yielding the same best-fit parameters, and contours of $\chi^2_w\sigma^2$ were very similar to contours of χ^2. Therefore we take 0.5 km to be a good estimate for σ in order to find the uncertainties in our fitted parameters. For a fit with one degree of freedom, one standard deviation in a single parameter is determined by projecting the region where $\chi^2_w - \chi^2_{w,min} = 1$ onto the axis of that parameter (Press et al., 1992). But, again, for one degree of freedom, $\chi^2_{w,min} = 1$, so this is simply $\chi^2_w = 2$, and using Eq. 5.16,

$$\chi^2 = 2\sigma^2 = 0.5. \tag{5.17}$$

Fig 5.8 shows how we project the boundaries of the region where $\chi^2 = 0.5$ onto each parameter's axis. Unfortunately, solutions with $\chi^2 \sim 0.5$ exist in a large region of parameter space for large values of D and h_0. In this area, the ring is nearly flat, with FWHM $\gtrsim$ 30 km, the half-width of the F-ring model itself, and there is little to differentiate between the models as h_0 and D increase. To estimate the uncertainties of the parameters, then, we ignore this region and use the left-hand side of the $\chi^2 = 0.5$ contour. This gives us one-sigma uncertainties of $\sigma_{h_0} = 4$ km and $\sigma_D = 4$ km.

5.7 Agreement between the Model and the Data at Different Times

As shown in Fig. 5.9, the model best reproduces the observed asymmetry with different sets of parameters at different times. The ultimate choice of the best fit is a compromise between the data points at 22:00 and 23:30 UT, which are better fit by values of D$\gtrsim$10 km and h_0 $\sim$6–10 km, and the best fit for 25:00 UT, which

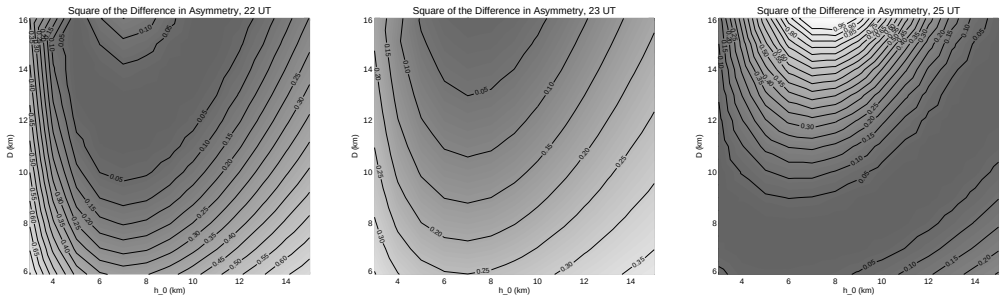

Figure 5.9: The square of the difference between the model asymmetry and HST asymmetry for each lit-side observation time.

strongly argues for D$\sim$ 7.5 km, at least for the lower values of h_0 that provide the best fit for the 22:00 and 23:00 UT points. However, the model can essentially match the 25:00 UT data point for any D$>$ 6 km, requiring larger values of h_0 as D increases.

For every value of h_0 that was tried, including the three values of h_0 shown in Fig. 5.10, increasing D while holding h_0 constant resulted in increased magnitude of asymmetry for each of the lit-side data points. This is what we intuitively expect, because the asymmetry is caused by the asymmetrical blocking of the main rings by the F ring due to the F ring's geometry. Increasing the amount of material in the F ring increases the amount of blocking, which increases the model asymmetry for all data points.

Notice in this plot that at 22:00 and 23:30 UT, the magnitude of the observed asymmetry is less than the model asymmetry for almost all parameter choices. This explains why the contribution to the χ^2 for these data points (i.e., the square of the difference between the model asymmetry and the observed asymmetry) decreases for larger D. At 25:00 UT, though, the model asymmetry is actually greater than the observed asymmetry for larger values of D, leading to an increase in that point's contribution to the χ^2 as D increases. We also approach this situation

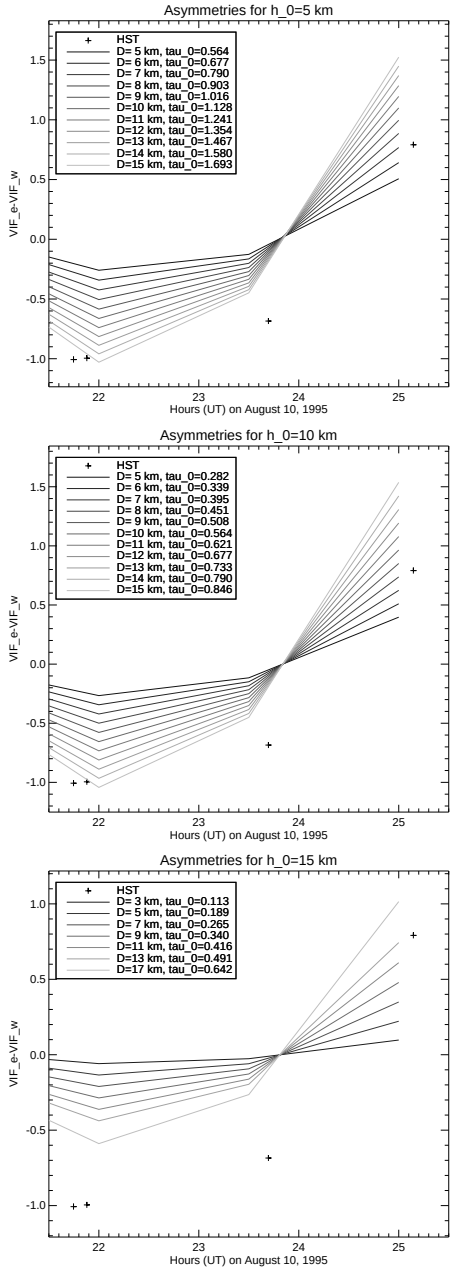

Figure 5.10: $\Delta\langle \mathrm{VIF} \rangle$ vs. t on the lit side of the rings. Each plot shows model results for a single h_0 and a range of equivalent depths. Note that the magnitude of the asymmetry at each time increases monotonically with increasing equivalent depth, D.

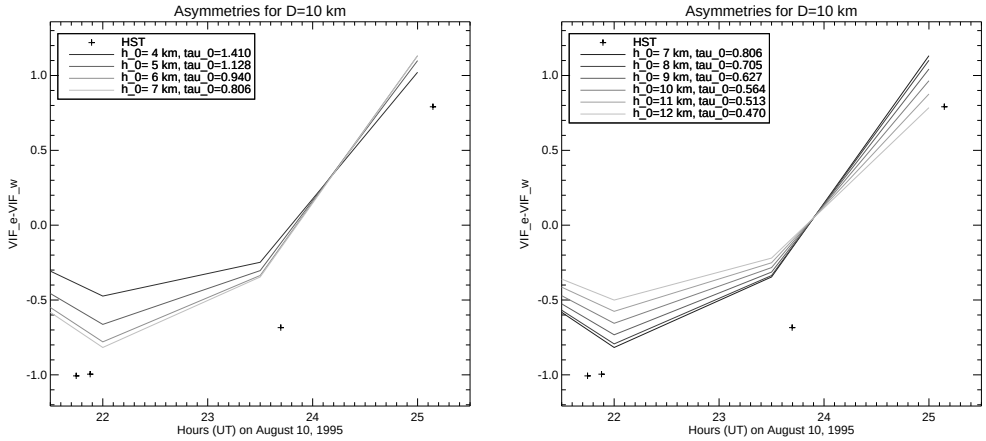

Figure 5.11: $\Delta\langle\mathrm{VIF}\rangle$ vs. t on the lit side of the rings for D=10 km. The plot to the left shows series of values of $h_0 \leq 7$ km, while on the right, $h_0 \geq 7$ km.

for the asymmetry at 22:00 UT for the very largest values of D that were tested (D>14 km) and h_0=5–10 km.

The explanation for the variation of χ^2 with h_0 is less intuitively obvious. The first plot in Fig. 5.11 shows that for $h_0 \lesssim 7$ km, increasing h_0 increases the magnitude of the asymmetry. However, the right-hand plot shows that for values of $h_0 \gtrsim 7$ km, increasing h_0 decreases the magnitude of the asymmetry. The maximum asymmetry for a given D occurs around $h_0 \sim$7 km for each time.

Considering how the different components of the model vary as h_0 varies, the greatest change in the asymmetry occurs in the blocking of light from the main rings by the F ring. For all times this asymmetry is largest in magnitude at $h_0 \sim$7 km. There is some change in the asymmetry with h_0 due to the back of the F ring being blocked by the main rings, but this asymmetry increases steadily with time over the times of the lit-side observations.

Fig. 5.12 shows profiles of VIF(r) for the FBM component, i.e., the blocking of the main ring's light by the front of the F ring, for 22:00 UT. The values plotted are negative, so a more negative value indicates more blocking. The greatest amount of

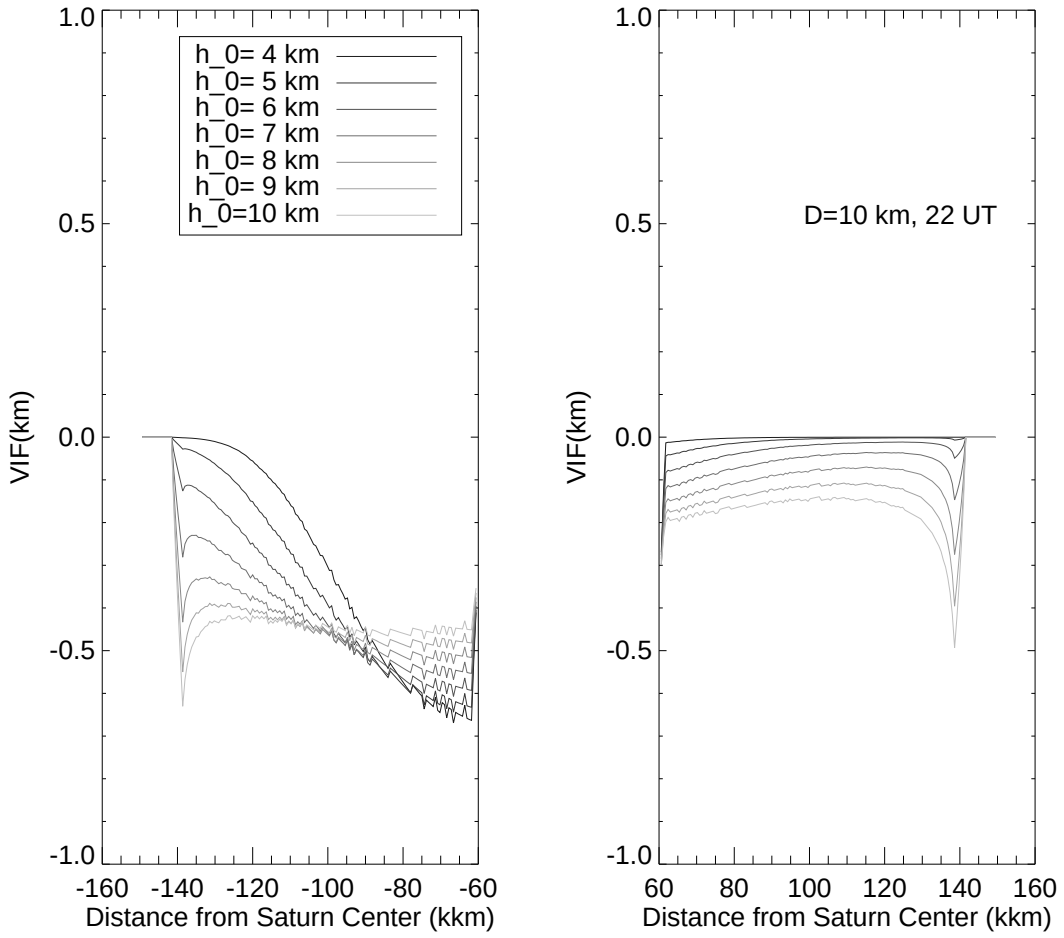

Figure 5.12: Profiles of VIF(r) for the blocking of light from the main rings by the front of the F ring (the FBM model component), with D=10 km at 22:00 UT for a range of h_0.

blocking occurs where the central core of the F ring cuts across the main rings (see Fig. 5.5), in this case in the C ring region on the east ansa. We can see that this maximum blocking is reduced as h_0 increases, because this leads to a less centrally condensed F ring, decreasing the optical depth of the central region. Conversely, the blocking east of $r = -90,000$ km, where the central core does not lie directly in front of the main rings, increases as h_0 increases, because more F-ring material is distributed in the outer wings. In other words, for a given equivalent depth, for larger h_0, the vertical profile of the F ring's optical depth is flatter with r, and the blocking across the east ansa is more uniform. For smaller values of h_0, the amount of blocking averaged over the range 80,000–120,000 km increases rapidly as h_0 increases, because material is moved out of the optically-thick core. For larger values of h_0, however, the core is less optically thick, and increasing h_0 leads to a more modest increase in the overall blocking.

On the west ansa, the core of the F ring does not fall across the main rings at all, but as the outer southern edge of the F ring, which does graze the main rings, increases in optical depth, the amount of blocking rises steadily with h_0.

It is the difference of the blocking that leads to an asymmetry. For smaller h_0, too much of the F ring's material is concentrated in the opaque core in front of the relatively dim C ring, and there is not enough blocking on the east ansa to create a large asymmetry. For very large h_0, the F ring obscures both ansae more evenly, leading again to a smaller asymmetry. Thus, there is an intermediate value of h_0 that maximizes the east-west asymmetry.

At the other times, the asymmetry varies with h_0 in a similar manner. The difference between the blocking of the ansae typically maximized somewhere in the range $h_0 \sim$5–10 km for each time.

For each HST data point, then, there is a "U"-shaped path through the parameter space (Fig. 5.9) that provides good matches to the model asymmetry. Below the "U", the model asymmetries are too small, and above the "U" they are too large. Around h_0 ∼7 km, the model asymmetry is greatest for a given D; thus the region at the base of the "U" is the minimum D that will match the observed asymmetry. It is the overlap of these regions where we find the best overall fit to the model.

5.8 Conclusions

We find the best fit to the observed ring asymmetry and brightness is achieved with an F ring model with an equivalent depth of D=10±4 km and a scale height of h_0=8±4 km, i.e., a full-width at half maximum of 13±7 km.

In order to fit the dark-side brightness of the rings, we find $p_f = P(\alpha) = 0.4 \pm 0.2$. This agrees with the model results of Poulet et al. (2000a), who found $p_f \sim 0.6$ but had assumed that only the front of the F ring was visible.

Although the observed asymmetries before the ring-plane crossing are not well reproduced by the model, these asymmetries are much smaller than those seen on the lit side, with $\Delta\langle\mathrm{VIF}\rangle \lesssim 0.5$ km. The observed dark-side asymmetries appear to be attributable to longitudinal variations in the F ring rather than to blocking of the back of the F ring by the main rings, which is the major source of asymmetry in the dark-side brightnesses in our model.

The observed dark-side profiles of VIF(r), which are flatter than the profiles produced by our model, might be better fit by an F ring with a more compact, optically thick core and a more diffuse envelope, but this is a scenario best explored in future models.

The lit-side asymmetries are reproduced well by our model, including a reversal in the sense of the asymmetry around 0:30 UT on 11 August 1995. We find that these asymmetries are due to blocking of light from the main rings by the front of F ring. The magnitudes of the asymmetries in the model results are very sensitive to the choices of D and h_0 for the F-ring model.

The best-fit equivalent depth of this model, D=10±4 km, agrees with the equivalent depth of 8±3 km that Poulet et al. (2000a) found for a vertically uniform F ring model that reproduces the dark-side brightness observed by various instruments in the near infrared during the 10 August 1995 ring-plane crossing.

These equivalent depths, obtained from photometric models of the ring system seen edge-on in 1995, are both greater than the equivalent depths derived from profiles of optical depth of the F ring obtained from occultations in the 1980s. The equivalent depth measured by Voyager 1 at $\lambda = 0.26$ μm from an occultation of the star δ Sco in 1981 was only 4.33±0.13 km (Showalter et al., 1992). This was a single measurement at one longitude. An occultations of the star 28 Sgr in 1989 yielded equivalent depth measurements at four different longitudes of 3.79±0.08 km, 3.0±0.1 km, 2.8±0.1 km, and 3.6±0.1 km at wavelengths in the near infrared from 2.2–3.9 μm (Nicholson et al., 2000), all apparently inconsistent with the equivalent depths derived from photometric models.

In 1995, the equivalent depth derived from an occultation of the star GSC5249-01240, measured at B=$\sim$ 3°, was substantially larger than the earlier measurements, with D=7.41±0.15 km obtained from HST data at λ=0.27–0.74 μm and 5.76±0.06 km from IRTF at $\lambda = 2.3$ μm (Bosh et al., 2002). Also, eight recent Cassini measurements of the F ring's optical depths from stellar occultations with B=3.45° and 32.16° gave a mean equivalent depth of 9±2 km at $\lambda = 3$ μm (per-

sonal communication, P. Nicholson), which agrees with the results of Poulet et al. (2000a) and the present model.

It is well-known that the characteristics of the F ring are not uniform longitudinally due to complex dynamical interactions with its shepherding satellites, Pandora and Prometheus. A severe limitation of the occultation data is that they sample the F ring at only one longitude, or two if both the ingress and egress can be captured. An event such as the 28 Sgr occultation, viewed from Earth by many observers, offers only a slight variation in the longitudes sampled. By contrast, the Cassini occultations consist of repeated observations at longitudes distributed around the F ring. The range of equivalent depths measured, from 6–14 km, demonstrates the variablity of the F ring with longitude. The wide range of equivalent depths measured in occultations and the paucity of these measurements make it difficult to draw firm conclusions in comparison with the photometric models, which assume a longitudally uniform equivalent depth.

There are also some hints that the F ring's behavior is also not uniform over decadal timescales. For example, during the 1995 ring-plane crossing, McGhee et al. (2001) discovered substantial clumps in or near the F ring with brightnesses equivalent to some of the small satellites that were seen in Voyager images, yet only much smaller clumps were observed during the Voyager encounters (Showalter, 2004). In the first year of its mission, the Cassini spacecraft has observed very little clump activity in the F ring (personal communication, P. Nicholson).

Our model optical depth profile has a vertical FWHM of 13±7 km. Because of the low ring-opening angle, the results of our model have nothing to say about the radial distribution of material in the F ring. In contrast, there is some ambiguity in the interpretation of occultation measurements of the FWHM of the F ring's

optical depth profile by Bosh et al. (2002). For example, a radial FWHM of 43.4±1.0 km is derived from the HST observations of the occultation of the star GSC5249-01240, and a FWHM of 44.7±0.7 km is measured in an IRTF observation at a slightly different longitude. However, this assumes that the F ring is flat in its ring plane. Because the ring opening angle was only $\sim 3.0°$, this could also correspond to a vertical thickness of just $44 \text{ km} \cdot \sin 3.0° = 2$ km. More likely, this measured FWHM has both a radial contribution and a vertical contribution. If a vertical FWHM of 13 km was observed from a ring-opening angle of 3°, and the F ring were interpreted as flat, its radial FWHM would be 250 km. Care should be taken in comparing these figures, though, because we assume a gaussian profile of vertical F-ring optical depth, while Bosh et al. (2002) fit their data with a Lorentzian function. Their observed profile of optical depth has a full radial width of several hundred kilometers.

The stellar occulation observed by the Voyager 2 PPS at $\lambda = 0.26$ μm had a ring-opening angle of 28°. The full radial width of the F ring was measured as at least 50 km (Lane et al., 1982). This could also be interpreted as a vertical height of 30 km, though, as before, it is more likely interpretation is a radial width of less than 50 km and a full height of less than 30 km.

Appendix A

Saturnshine

Sunlight scattered by Saturn is a significant source of illumination for the main rings for some geometries, especially on the dark side of the rings when the ring-opening angle is large.

Understanding this contribution to the I/F can be confusing because it is not due to the rings being inherently more reflective, but rather to an additional source of light that makes the total intensity of light scattered by the rings greater than if the rings were only receiving direct sunlight. Recall that when we measure I/F in an image, we are really measuring the intensity of light scattered by the rings, then scaling by the incident flux of direct sunlight. Since direct sunlight is not the only source of incident light in this situation, the observed I/F is greater than the simple reflectance of the rings.

For each point on the main rings, we compute the additional I/F due to saturnshine. We must first determine the geometry of each point on Saturn relative to the Sun and that ring point, and use a reflectance model for Saturn to determine how much light is scattered by that point on the planet toward the ring point. The single-scattering reflectivity for that point on the rings then determines how much saturnshine is scattered toward Earth. We sum over all points on Saturn to find the total I/F due to saturnshine for that point, and then repeat the process for each point on the rings to construct a two-dimensional image of the saturnshine's contribution to the I/F of the main rings.

A.1 Geometry for Saturnshine

For each point on Saturn we must determine the cosine of the incidence angle for incoming sunlight ($\mu_0 = \cos i$), the cosine of the emission angle for light scattered by Saturn to the point in question on the rings ($\mu = \cos \epsilon$), the distance between the point on the planet and point on the rings (d), the incidence cosine of light from Saturn at the point on the rings ($\mu_0' = \cos i'$), and the phase angle (α_{ss}) between the point on Saturn, the point on the rings, and the Earth.

Let the center of Saturn be the point A, and let B be a point on Saturn's surface. The position of B is specified using its latitude, ϕ_s, and longitude, θ_s. Unlike our previous coordinate systems, where θ is measured from the subearth point, in this case θ_s is measured from the subsolar point. Further, we make the approximation that the subsolar point is on the equator of Saturn (i.e., B_s is taken to be zero) which is satisfactory for times near the ring-plane crossings. For simplicity, we also ignore the oblateness of Saturn and take the planet to be spherical, with all points on Saturn's surface located at a distance $r_s = 60,300$ km from the center of the planet.

The cosine of the incidence angle depends only on the position of the point on the surface of Saturn, as shown in Fig. A.1. Using the law of cosines for spherical triangles (or Napier's rules for right spherical triangles):

$$\mu_0 = \cos i = \cos \theta_s \cos \phi_s. \tag{A.1}$$

The position of a point on the rings, C, is specified by r_r, its distance from the center of the planet, and θ_r, the azimuthal angle, which, like θ_s is measured from the subsolar point. The geometry is shown in Fig. A.2. The angle labeled β is

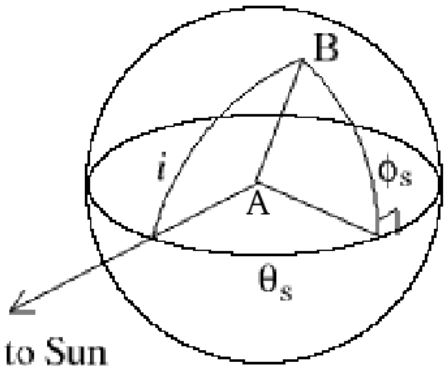

Figure A.1: Geometry for the incidence angle at the point B on the surface of Saturn. Point A marks the center of the planet.

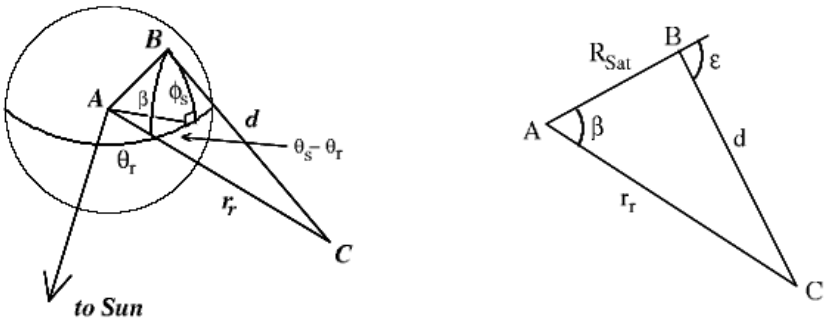

Figure A.2: Geometry for the emission angle from point B on Saturn to point C in the rings.

given by the law of cosines for spherical triangles:

$$\cos(\beta) = \cos(\theta_r - \theta_s)\cos\phi_s. \tag{A.2}$$

Taking the triangle ABC, shown in Fig. A.2, we can use the law of cosines for plane triangles to find the distance d between the point on Saturn and the ring particle,

$$d = \sqrt{R_s^2 + r_r^2 - 2R_s r_r \cos\beta}, \tag{A.3}$$

where R_s is the radius of Saturn.

Finally, from the same triangle, the plane law of cosines gives us the value of the emission angle, ϵ.

$$\mu = \cos\epsilon = \frac{r_r^2 - R_s^2 - d^2}{2R_s d}. \tag{A.4}$$

Notice that, while μ is defined to be positive in Section 2.2.1, this expression can yield a negative number for μ for values of $d > \sqrt{r_r^2 - R_s^2}$. Such points on Saturn are not visible to the ring particle, and we will be excluding them from the calculation.

The incidence angle for light from Saturn striking the rings is i', the angle between the line BC and a normal to the ring-plane at point C in Fig. A.2. Let this normal have the same height above the ring plane as the point B, $R_s \sin\phi_s$. Then the normal and a line from the top of the normal to B form a right angle, and the line BC, which has a length of d, is the hypotenuse of a right triangle. The cosine of the incidence angle is then:

$$\mu_0' = \frac{|R_s \sin\phi_s|}{d}. \tag{A.5}$$

where we take the absolute value to ensure that μ_0 is always positive, as described in Section 2.2.1.

The phase angle for light from Saturn incident on a ring particle and then reflected toward Earth is labeled α_{ss} to distinguish it from the Earth-Saturn-Sun phase angle.

Using the coordinate system that has been defined for the saturnshine calculation (Fig. A.2), with the $\hat{x}$ axis in the equatorial plane at the subsolar longitude, and the $\hat{z}$ axis aligned with Saturn's north pole, we can find Cartesian coordinates for the position of the ring particle, C,

$$\mathbf{r_r} = (r_r \cos\theta_r, r_r \sin\theta_r, 0), \tag{A.6}$$

and for the point on Saturn, B,

$$\mathbf{r_s} = (R_s \cos\theta_s \cos\phi_s, R_s \sin\theta_s \cos\phi_s, R_s \sin\phi_s). \tag{A.7}$$

The vector CB from the point on the rings to the point on Saturn is then:

$$\mathbf{r} = \mathbf{r_s} - \mathbf{r_r} = (R_s \cos\theta_s \cos\phi_s - r_r \cos\theta_r, R_s \sin\theta_s \cos\phi_s - r_r \sin\theta_r, R_s \cos\theta_s). \tag{A.8}$$

and this vector has the length d as computed in Eq. A.3.

Next we will need the phase angle between Saturn, the point on the rings, and the Earth, which is the angle between the vector $\mathbf{r}$ and a vector that points toward Earth. In Saturn spherical equatorial coordinates, the unit vector in the direction of Earth is:

$$\mathbf{r_e} = (\cos\theta_e \cos\phi_e, \sin\theta_e \cos\phi_e, \sin\phi_e). \tag{A.9}$$

ϕ_e is just the ring-opening angle, B_e. The cosine of the angle between $\mathbf{r}$ and $\mathbf{r_e}$ is given by the dot product of the vectors:

$$\cos\alpha_{ss} = \frac{R_s[\cos(\theta_s - \theta_e)\cos\phi_s \cos B_e + \cos\theta_s \sin B_e] - r_r \cos(\theta_r - \theta_e)}{d}. \tag{A.10}$$

Thus, for any point on the rings, we can calculate μ, μ_0, d, μ_0', and α_{ss} for all points on Saturn.

A.2 Light Scattered by the Disk of Saturn

For our calculation of sunlight scattered by the planet, we construct a two-dimensional array of θ_s and ϕ_s which specifies the locations of area elements dA on Saturn. The spacing between the values of θ_s and ϕ_s are $d\theta_s$ and $d\phi_s$ respectively.

This array is limited to $|\theta_s| < 90°$, the illuminated part of the planet. Also, regions where the emission angle is greater than 90° ($\mu < 0$) are beyond the limb of the planet and are set to $(I/F)_s = 0$. Because reflected and transmitted saturnshine are calculated separately, only one hemisphere of the planet needs to be considered. Because the ring-opening angles to Earth and the Sun are both very small, we can ignore the shadow of the rings on the planet, and because the phase angle α_{ss} (Eq. A.10) is symmetric in the northern and southern hemispheres, we simply chose latitudes $0° < \phi_s < 90°$ for all calculations.

The reflectance for a point on Saturn is typically modeled using a Minnaert law:

$$(I/F)_s = (k + \frac{1}{2}) p \mu_0^k \mu^{k-1}, \tag{A.11}$$

where p is the planet's geometric albedo (Veverka et al., 1986). Dones et al. (1993) measured Saturn's brightness in Voyager clear-filter images at a wide variety of phase angles and found that the best-fitting value for the index was $k = 0.67$, with $r_n = 0.36$.

Notice that a special case of this Minnaert law is the Lambert scattering case (Eq. 2.37) which corresponds to $k = 1$ and $p = \frac{2}{3}$. Poulet et al. (2000a) chose $k = 1$ with $p = 0.1$. It is reasonable that their model planet's albedo was significantly less than unity (the albedo of a true Lambert scatterer), because they modeled data at 2.2μm, deep in a methane absorption band.

Because the Lambert form requires significantly less computation time, and we found that using $k = 0.67$ did not result in significantly different results, we use $k = 1$ in our model, and take the reflectance of Saturn to be:

$$I/F_s = 1.5p\mu_0. \tag{A.12}$$

We assume that the disk of Saturn is of uniform albedo, though it actually exhibits some latitudinal variation. The full-disk reflectance spectrum of Saturn at near-infrared wavelengths has been measured by Karkoschka (1994, 1998). The HST 0.89-μmfilter has a central wavelength of 0.88912 μm and a FWHM of 0.00937 μm. The average of Saturn's albedo over the range 0.88–0.90 μm is $p = 0.08$. The uncertainty in the albedo is ± 0.01 (Karkoschka, 1994), though systematic errors in the albedo deep in methane bands may be greater (Karkoschka, 1998).

Consider a flux of sunlight $\pi F_\odot$ incident on an area element dA at the location (θ_s,ϕ_s) on Saturn. Let the size of the element be:

$$dA = R_s^2 \cos(\phi_s) d\theta_s d\phi_s. \tag{A.13}$$

The intensity of light scattered by the element dA in the direction μ is then

$$I_{ss} = (I/F)_s(\mu_0, \mu)F_\odot = \frac{3}{2}\ p\ \mu_0\ F_\odot. \tag{A.14}$$

A.3 Saturnshine Scattered by the Main Rings

Once the light is scattered by Saturn, it passes through a vacuum, so the intensity is conserved. It is then incident at a point on the rings.

The reflectance of the rings is given by the single-scattering formulae of Chandrasekhar (1960) (Eqs. 2.39 and 2.38), but now the source of the incident light is

not the Sun, but Saturn, so we use α_{ss} for the phase angle, and the incidence cosine is μ_0' from Eq. A.5. The emission cosine to Earth is $\mu' = |\sin B_e|$. For saturnshine reflected by the rings,

$$(I/F)_r = \frac{1}{4} P(\alpha_{ss}) \varpi_0 \frac{\mu_0'}{\mu' + \mu_0'} \left(1 - e^{-\tau(1/\mu' + 1/\mu_0')}\right). \tag{A.15}$$

while for transmitted saturnshine,

$$(I/F)_r = \frac{1}{4} P(\alpha_{ss}) \varpi_0 \frac{\mu_0'}{\mu' - \mu_0'} \left(e^{-\tau/\mu'} - e^{-\tau/\mu_0'}\right). \tag{A.16}$$

As is the case for the rest of the ring model, we use the phase function of Dones et al. (1993), given in Eq. 4.35, and the single-scattering albedo and optical depth profiles discussed in Section 4.5.2.

In Eqs. A.15 and A.16, as always, the incident flux πF is defined per unit area normal to the beam. The flux incident on the rings from the area dA on the planet is:

$$dF_{ss} = I_{ss} d\Omega, \tag{A.17}$$

where I_{ss} is the intensity of saturnshine scattered by the solid angle $d\Omega$ on Saturn. The solid angle of dA on Saturn as viewed from a point on the rings is:

$$d\Omega = \mu \frac{dA}{d^2} = \frac{\mu R_s^2 \cos(\phi_s) d\theta_s d\phi_s}{d^2}. \tag{A.18}$$

The intensity of saturnshine from dA which is scattered toward the observer by the rings is:

$$dI = (I/F)_r(\mu_0', \mu', \alpha_{ss}) \frac{dF_{ss}}{\pi}. \tag{A.19}$$

Substituting Eq. A.17:

$$dI = \frac{1}{\pi} (I/F)_r I_{ss} d\Omega. \tag{A.20}$$

Substituting Eq. A.14:

$$dI = \frac{F_\odot}{\pi} (I/F)_r (I/F)_s d\Omega. \tag{A.21}$$

The intensity scattered by this point on the rings due to saturnshine from the entire planet is found by integrating over the entire portion of the planet that is visible to the ring particle and also illuminated by the Sun:

$$I = \frac{F_\odot}{\pi} \int (I/F)_r (I/F)_s d\Omega. \tag{A.22}$$

The contribution to the ring's I/F due to saturnshine is:

$$I/F_\odot = \frac{1}{\pi} \int (I/F)_r (I/F)_s d\Omega. \tag{A.23}$$

or, assuming Lambert scattering for the disk of Saturn, and substituting Eq. A.18, we find for reflected saturnshine:

$$I/F_\odot = \frac{1.5\ p}{4\pi} \varpi_0 R_s^2 \int\int \frac{P(\alpha_{ss})}{d^2} \frac{\mu_0 \mu \mu_0'}{\mu' + \mu_0'} \left(1 - e^{-\tau(1/\mu' + 1/\mu_0')}\right) \cos(\phi_s) d\theta_s d\phi_s, \tag{A.24}$$

while for transmitted saturnshine:

$$I/F_\odot = \frac{1.5\ p}{4\pi} \varpi_0 R_s^2 \int\int \frac{P(\alpha_{ss})}{d^2} \frac{\mu_0 \mu \mu_0'}{\mu' - \mu_0'} \left(e^{-\tau/\mu'} - e^{-\tau/\mu_0'}\right) \cos(\phi_s) d\theta_s d\phi. \tag{A.25}$$

The limits of integration are $-90° < \theta_s < 90°$ and $0 < \phi_s < 90°$, and the part of the planet where $\mu < 0$ has $(I/F)_s$ set to zero so that it is not included in the integral.

A.4 Saturnshine in HST data from 21 November 1995

On 21 November 1995, the ring-opening angle to Earth was $B_e = 2.67°$ and the ring-opening angle to the Sun was $B_s = -0.029°$, so the Earth was on the dark side of the rings. (See Table 4.1.) Nicholson et al. (1996) report HST observations of Saturn's rings at this time, including radial scans of the rings' I/F (not VIF). These scans are dominated by sunlight transmitted through the C ring, Cassini

Division, Encke Gap,and F ring, but also show non-zero values for the I/F in the A ring and B ring. The latter decrease with increasing distance from the planet and are higher on the west ansa than on the east ansa. The brightness of the A and B rings was not explained at the time, though it was suggested that it was due to saturnshine, and that the asymmetry in brightness may have been caused by the relatively large phase angle, $\alpha = 5.58°$.

Using our model and including both transmitted and reflected saturnshine, we are able to reproduce the observed profile of I/F. The non-zero phase angle during these observations does indeed cause a significant asymmetry in the brightness of transmitted and reflected saturnshine between the east and west ansae, and saturnshine appears to be the explanation for the asymmetry observed in the HST images on this date. Our model I/F profile, taken along $\theta = \pm 90°$ and smoothed to HST resolution (600 km), is shown in Fig. A.3.

The most important contribution to the I/F profile is transmitted sunlight, which is strongest in regions with low optical depth: the C ring, the Cassini Division, the Encke Gap and the Keeler Gap (visible at the outer edge of the A ring). The profile of reflected sunlight is symmetric between the east and west ansae.

Significant amounts of saturnshine are also transmitted though the same regions. Also, the inner B ring and the A ring transmit more saturnshine than sunlight. This can be understood by comparing Eqs. 2.39 and A.25 and realizing that while the incidence angle of sunlight on the rings (μ_0) and the emission angle to Earth (μ in Eq. 2.39 and μ' in Eq. A.25) are both much less than τ in both the A and B ring, the incidence angles of saturnshine from the planet can be much higher, so that μ_0' can approach the value of typical optical depths in the A ring and the inner B ring of $\sim 0.4 - 0.8$ (Nicholson et al., 2000). The brightness of

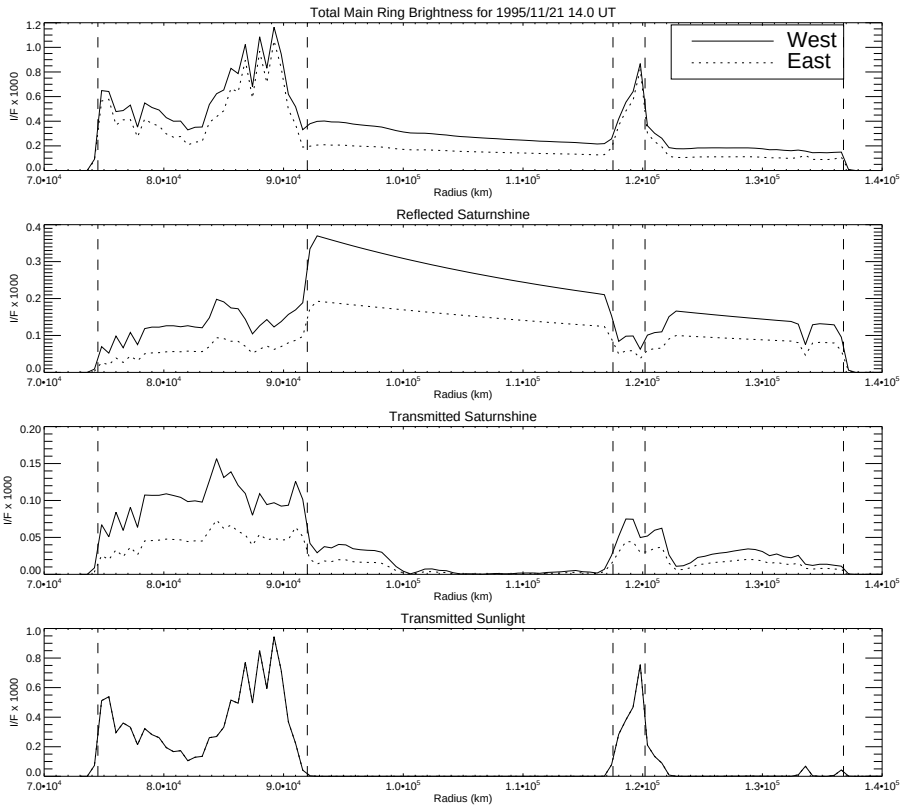

Figure A.3: Profiles of I/F $\times$ 1000 vs. radius for 21 November 1995, showing, from bottom to top, transmitted sunlight, transmitted saturnshine from the southern hemisphere of Saturn, reflected Saturnshine from the northern hemisphere of Saturn, and the sum of these three components. The solid and dotted lines are the I/F profiles for the west and east ansae, respectively, and the dashed lines indicate the boundaries of the C ring, B ring, and A ring. The F ring is not included. Cf. Fig. 4 of Nicholson et al. (1996).

transmitted saturnshine is greater on the west ansa than on the east ansa because the Sun is to the west; as a result, ring particles on the eastern ansa see less of the illuminated hemisphere of the planet, and see it at a higher phase angle.

This asymmetry is also apparent in the profile of reflected saturnshine. In this case it is the A ring and the B ring that scatter the most saturnshine. As can be seen in Eq. A.24, it is the very small emission angle to Earth which dominates the exponential factor so that in the A and B ring, $\tau/\mu' \gg 1$, which is the optically thick limit described by Eq. 2.42. As a result, the reflected light profile in these regions is insensitive to τ, and drops off smoothly as the distance from the planet increases.

The main ring albedoes need to be scaled down by a factor of 0.55 in order to obtain the best fit to the observed HST profiles from November 1995. This is comparable to the scaling factor p_m used to adjust the main-ring brightness in the full photometric model to match the August RPX data. (See Sec. 4.6.4.)

A.5 Saturnshine for the August ring-plane crossing

For any given point on the rings, we would expect the I/F due to both reflected and transmitted saturnshine to be very similar in the August data, except for the effect of the lower Earth-Sun phase angle of 3.58°.

The I/F due to saturnshine for one point on the rings is given in Eq. A.23, where the integral is taken over the planet. While the position of the Sun does change slightly, the incidence angle of sunlight for each point on the planet will change very little, so $(I/F)_s$ will be very similar in both observations.

For optically thick regions of the ring, the reflectance of the rings can be simplified to Eq. 2.42. Using the incidence cosines that we have defined for saturnshine:

$$(I/F)_r \approx 1/4 P(\alpha_{ss}) \varpi_0 \frac{1}{\frac{\mu'}{\mu'_0} + 1}. \tag{A.26}$$

For most points on Saturn, $\mu'_0 \gg \mu'$, so the ring reflectance can be further simplified to $(I/F)_r \approx 1/4 P(\alpha) \varpi_0$, which has no dependence on μ'. Thus the saturnshine reflected from the rings will vary little between August and November.

For transmitted light, because the ring-opening angle is small, $\tau/\mu' \gg 1$, and for most parts of the planet, $\mu'_0 \gg \mu'$, so Eq. A.16 can be simplified to

$$(I/F)_r \approx \frac{1}{4} P(\alpha_{ss}) \varpi_0 e^{-\tau/\mu'_0}. \tag{A.27}$$

Again, there is very little dependence on variables which change significantly between August and November.

Now consider the sunlight transmitted through the rings. For August, $\mu_0 \gg \mu$, so Eq. 2.39 becomes

$$\mathrm{I/F} = \frac{1}{4} P(\alpha) \varpi_0 e^{-\tau/\mu_0}. \tag{A.28}$$

On the other hand, for November, $\mu_0 \ll \mu$, so Eq. 2.39 can be simplified to

$$\mathrm{I/F} = \frac{1}{4} P(\alpha) \varpi_0 \frac{\mu_0/\mu}{e}^{-\tau/\mu}. \tag{A.29}$$

and the factor μ_0/μ means that the transmitted sunlight is much less in November.

Model results agree with these analytical approximations, as can be seen by comparing Fig. A.3 with Fig. A.4. In August, the Sun was to the east of the Earth, and it is the eastern ansa of the rings that is brighter. The phase angle in August is $\alpha = 3.6°$, compared to 5.6° in November, so the asymmetry in the saturnshine brightness is less pronounced than in the November model. This profile shows that in for 10 August, saturnshine is unimportant compared to directly scattered

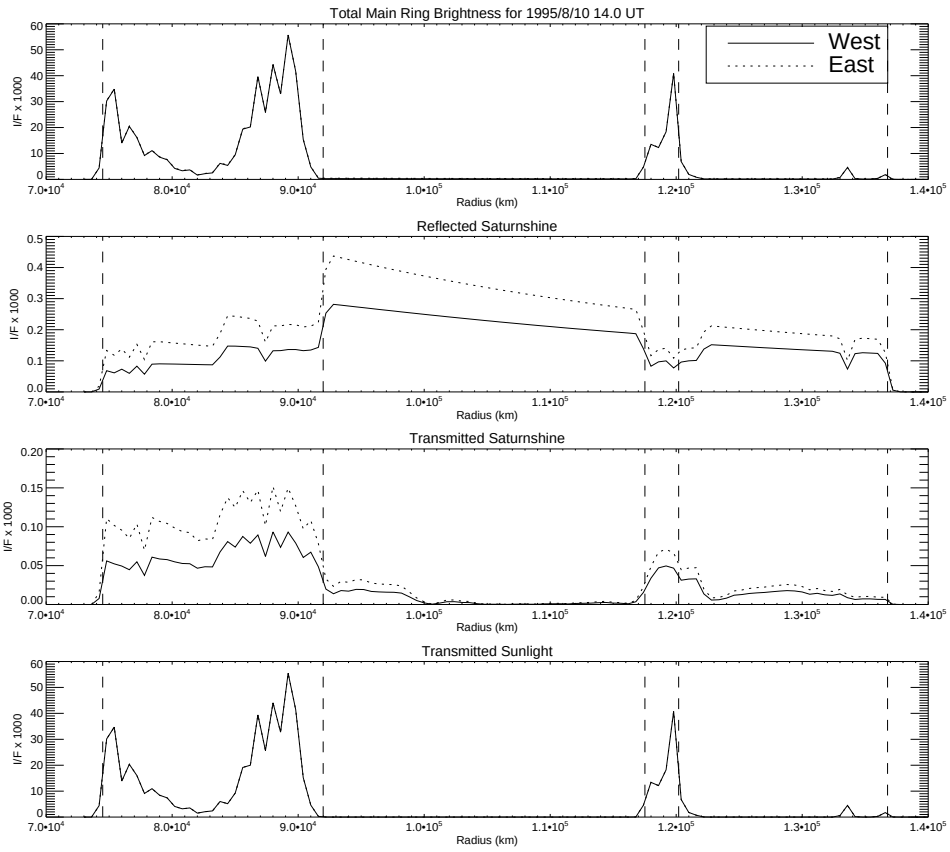

Figure A.4: Profiles of I/F × 1000 vs. radius for 14:00 UT on 8 August 1995, showing, from bottom to top, the contributions of transmitted sunlight, transmitted saturnshine, and reflected saturnshine on the east and west ansae, as well as the total VIF. Notice that saturnshine levels are very similar to the November 21 model (Fig. A.3) but the intensity of transmitted sunlight through the C ring and Cassini Division is much greater due to the higher incidence angle.

sunlight, even on the dark side of the rings, so saturnshine is not included in the main rings model.

Appendix B

Uncertainty in the F ring's Node and Inclination

One of the notable features in the plot of ⟨VIF⟩ vs. time is the point on the lit side when the linear fits to the brightness of the east ansa and west ansa intersect. (See, e.g., Fig. 5.7). At this point the sense of the asymmetry reverses, from the west ansa being brighter to the east ansa being brighter. According to our model, this occurs when the Earth crosses through the F ring's orbital plane, as shown in Fig. 4.1. When the Earth crosses the plane of the main rings, the main rings are seen edge-on, and during the F-ring-plane crossing (FRPX) the F ring is seen edge-on. During the August 1995 FRPX, the ascending node of the F ring on Saturn's equator coincidentally falls between Saturn and the Earth. However, even if the node is in a different location, because the F-ring plane includes both the center of Saturn and the line of sight to Earth during the FRPX, the edge-on F ring will appear to cut through the center of Saturn. Thus it obscures, and is obscured by, the main rings to an equal extent on both ansae, and (for this azimuthally symmetric F ring model, at least) there should be no difference in brightness between the ansae.

From the HST data, if we fit both PC and WF3 data, the FRPX time is 23:24 UT. Using just the WF3 data, we compute an FRPX time of 24:09 UT (which is actually 0:09 UT on 11 August.) Note that the difference is 45 minutes, which we take as an indication of the experimental uncertainty in the FRPX time.

Unlike the crossing times for the main rings, in our model the time of the F-ring-plane crossing, as determined from the intersection of the linear fits, shows little

dependence on the choice of photometric parameters of the F ring. It does depend on the orientation of the F-ring plane, which is determined by the inclination and the ascending node. To find the effect on the model results of small changes in the orbital elements of the F ring, we made several models with values for the inclination and the longitude of the ascending node increased and decreased by the standard errors given by Bosh et al. (2002). All these runs were conducted with $h_0 = 10$ km and $D = 5$ km.

For nominal values of the inclination and the longitude of the ascending node ($i = 0.0064°$ and $\Omega = 17.3°$) we find a predicted FRPX time of 23:29 UT. Increasing the longitude of the ascending node, which moves the node to the west on the sky, causes an earlier FRPX. For the nominal inclination ($i = 0.0064°$) and $\Omega = 13.4°$, the FRPX time is 24:06 UT on 10 August 1995, and for $\Omega = 21.2°$ the FRPX time is 23:21 UT. Increasing the inclination of the F ring has the effect of delaying the FRPX time. With the nominal value for the longitude of the ascending node and an inclination $i = 0.0057°$, the FRPX time was computed to be 23:20 UT, and for $i = 0.0071°$, the FRPX time was 24:09 UT.

Thus varying the inclination and longitude of the node within the quoted errors can change the time of the FRPX by up to 40 min, which is comparable to the uncertainty in the FRPX time that is measured from linear fits to the HST data.

Varying i and Ω also affected the model asymmetries, and changed the main ring crossing times, which are measured from the intersection of the linear fits to the dark side data and the lit side data for each ansa. However, this change was less than 2 min. The changes in the asymmetries resulted in changes in χ^2 values of up to 17%, much less than the 1-σ level of expected statistical variations (see Section 5.6).

Based on this experiment, we use the best fit F-ring orbit of Bosh et al. (2002) to determine the geometry for our model. Our model results show that a change in i or Ω greater than the uncertainty would lead to a significantly poorer fit to the HST data, but we do not have enough sensitivity to the node or inclination in these data to improve on the fit of Bosh et al. (2002).

BIBLIOGRAPHY

Alexander, A. F. O., 1962. The planet Saturn: a history of observation, theory, and discovery. New York, Macmillan, 1962.

Barbara, J. M., Esposito, L. W., Nov. 2002. Moonlet collisions and the effects of tidally modified accretion in Saturn's F ring. Icarus 160, 161–171.

Bobrov, M. S., Apr. 1972. Thickness of Saturn's rings from observations in 1966. Astronomicheskij Zhurnal 49, 427.

Bosh, A. S., Olkin, C. B., French, R. G., Nicholson, P. D., May 2002. Saturn's F ring: Kinematics and particle sizes from stellar occultation studies. Icarus 157, 57–75.

Bosh, A. S., Rivkin, A. S., Percival, J. W., Taylor, M., van Citters, G. W., Oct. 1997. NOTE: Saturn ring-plane crossing, May 1995: Pole precession and ring thickness. Icarus 129, 555–561.

Brahic, A., Sicardy, B., Feb. 1981. Apparent thickness of Saturn's rings. Nature 289, 447–450.

Burns, J. A., Showalter, M. R., Morfill, G. E., 1984. The ethereal rings of Jupiter and Saturn. In: Greenberg, R., Brahic, A. (Eds.), IAU Colloq. 75: Planetary Rings. pp. 200–272.

Chandrasekhar, S., 1960. Radiative Transfer. New York : Dover.

Cooke, M. L., 1991. Saturn's Rings: Photometric Studies of the C Ring and Radial Variation in the Keeler Gap. Ph.D. thesis, Cornell University.

Cuzzi, J. N., Burns, J. A., May 1988. Charged particle depletion surrounding Saturn's F ring—Evidence for a moonlet belt? Icarus 74, 284–324.

Cuzzi, J. N., Burns, J. A., Durisen, R. H., Hamill, P. M., Sep. 1979a. The vertical structure and thickness of Saturn's rings. Nature 281, 202–204.

Cuzzi, J. N., Durisen, R. H., Burns, J. A., Hamill, P., Apr. 1979b. The vertical structure and thickness of Saturn's rings. Icarus 38, 54–68.

Dollfus, A., May 1979. Photometric determination of the Saturn rings' thickness. Astronomy and Astrophysics 75, 204–206.

Dones, L., Cuzzi, J. N., Showalter, M. R., Sep. 1993. Voyager photometry of Saturn's A ring. Icarus 105, 184–215.

Doyle, L. R., Dones, L., Cuzzi, J. N., Jul. 1989. Radiative transfer modeling of Saturn's outer B ring. Icarus 80, 104–135.

Esposito, L. W., Cuzzi, J. N., Holberg, J. B., Marouf, E. A., Tyler, G. L., Porco, C. C., 1984. Saturn's rings—Structure, dynamics, and particle properties. In: Gehrels, T., Matthews, M. (Eds.), Saturn. Tucson: University of Arizona Press, pp. 463–545.

Fountain, J. W., Larson, S. M., Oct. 1978. Saturn's ring and nearby faint satellites. Icarus 36, 92–106.

French, R. G., McGhee, C. A., Dones, L., Lissauer, J. J., Mar. 2003. Saturn's wayward shepherds: The peregrinations of Prometheus and Pandora. Icarus 162, 143–170.

French, R. G., Nicholson, P. D., Cooke, M. L., Elliot, J. L., Matthews, K., Perkovic, O., Tollestrup, E., Harvey, P., Chanover, N. J., Clark, M. A., Dunham, E. W., Forrest, W., Harrington, J., Pipher, J., Brahic, A., Grenier, I., Roques, F., Arndt, M., Jun. 1993. Geometry of the Saturn system from the 3 July 1989 occultation of 28 SGR and Voyager observations. Icarus 103, 163–214.

Gehrels, T., Baker, L. R., Beshore, E., Blenman, C., Burke, J. J., Castillo, N. D., Dacosta, B., Degewij, J., Doose, L. R., Fountain, J. W., Gotobed, J., Kenknight, C. E., Kingston, R., McLaughlin, G., McMillan, R., Murphy, R., Smith, P. H., Stoll, C. P., Strickland, R. N., Tomasko, M. G., Wijesinghe, M. P., Coffeen, D. L., Esposito, L. W., Jan. 1980. Imaging photopolarimeter on Pioneer Saturn. Science 207, 434–439.

Goldreich, P., Tremaine, S. D., May 1978. The velocity dispersion in Saturn's rings. Icarus 34, 227–239.

Hämeen-Anttila, K. A., Vaaraniemi, P., Jul. 1975. A theoretical photometric function of Saturn's rings. Icarus 25, 470–478.

Karkoschka, E., Sep. 1994. Spectrophotometry of the jovian planets and Titan at 300- to 1000-nm wavelength: The methane spectrum. Icarus 111, 174–192.

Karkoschka, E., May 1998. Methane, ammonia, and temperature measurements of the jovian planets and Titan from CCD-spectrophotometry. Icarus 133, 134–146.

Lane, A. L., Hord, C. W., West, R. A., Esposito, L. W., Coffeen, D. L., Sato, M., Simmons, K. E., Pomphrey, R. B., Morris, R. B., Jan. 1982. Photopolarimetry from Voyager 2—Preliminary results on Saturn, Titan, and the rings. Science 215, 537–543.

Lumme, K., Irvine, W. M., Jan. 1979. Low tilt angle photometry and the thickness of Saturn's rings. Astronomy and Astrophysics 71, 123–130.

Marouf, E. A., Tyler, G. L., Rosen, P. A., Oct. 1986. Profiling Saturn's rings by radio occultation. Icarus 68, 120–166.

McGhee, C. A., 2000. Comet Shoemaker-Levy's 1994 collision with Jupiter and Saturn's 1995 ring plane crossings. Ph.D. thesis, Cornell University.

McGhee, C. A., Nicholson, P. D., French, R. G., Hall, K. J., Aug. 2001. HST observations of saturnian satellites during the 1995 ring plane crossings. Icarus 152, 282–315.

Murray, C. D., Chavez, C., Beurle, K., Cooper, N., Evans, M. W., Burns, J. A., Porco, C. C., Oct. 2005. How Prometheus creates structure in Saturn's F ring. Nature 437, 1326–1329.

Murray, C. D., Gordon, M. K., Giuliatti Winter, S. M., Oct. 1997. Unraveling the strands of Saturn's F ring. Icarus 129, 304–316.

Nicholson, P. D., Cooke, M. L., Pelton, E., Oct. 1990. An absolute radius scale for Saturn's rings. Astrophysical Journal 100, 1339–1362.

Nicholson, P. D., French, R. G., Bosh, A. S., Sep. 1999. The F ring: Saturn's crooked halo? AAS/Division of Dynamical Astronomy Meeting 31, #09.04.

Nicholson, P. D., French, R. G., Tollestrup, E., Cuzzi, J. N., Harrington, J., Matthews, K., Perkovic, O., Stover, R. J., Jun. 2000. Saturn's rings I. Optical depth profiles from the 28 Sgr occultation. Icarus 145, 474–501.

Nicholson, P. D., Showalter, M. R., Dones, L., French, R. G., Larson, S. M., Lissauer, J. J., McGhee, C. A., Sicardy, B., Seitzer, P., Danielson, G. E., 1996. Observations of Saturn's ring-plane crossing in August and November. Science 272, 509–516.

Olkin, C. B., Bosh, A. S., Sep. 1996. The inclination of Saturn's F ring. Bulletin of the American Astronomical Society 28, 1125.

Poulet, F., Karoschka, E., Sicardy, B., Oct. 1999. Spectrophotometry of Saturn's small satellites and rings from Hubble Space Telescope images. Journal of Geophysical Research 104, 24095–24110.

Poulet, F., Sicardy, B., Dumas, C., Jorda, L., Tiphène, D., May 2000a. The crossings of Saturn ring plane by the Earth in 1995: Ring thickness. Icarus 145, 147–165.

Poulet, F., Sicardy, B., Nicholson, P. D., Karkoschka, E., Caldwell, J., Mar. 2000b. Saturn's ring-plane crossings of August and November 1995: A model for the new F-ring objects. Icarus 144, 135–148.

Press, W. H., Teukolsky, S. A., Vetterling, W. T., Flannery, B. P., 1992. Numerical Recipes in FORTRAN. The Art of Scientific Computing, 2nd Edition. Cambridge: University Press.

Salo, H., Karjalainen, R., Aug. 2003. Photometric modeling of Saturn's rings I. Monte Carlo method and the effect of nonzero volume filling factor. Icarus 164, 428–460.

Showalter, M. R., Nov. 1998. Detection of centimeter-sized meteoroid impact events in Saturn's F ring. Science 282, 1099–1102.

Showalter, M. R., Oct. 2004. Disentangling Saturn's F ring. I. Clump orbits and lifetimes. Icarus 171, 356–371.

Showalter, M. R., Burns, J. A., Dec. 1982. A numerical study of Saturn's F-ring. Icarus 52, 526–544.

Showalter, M. R., Pollack, J. B., Ockert, M. E., Doyle, L. R., Dalton, J. B., Dec. 1992. A photometric study of Saturn's F ring. Icarus 100, 394–411.

Sicardy, B., Lecacheux, J., Laques, P., Despiau, R., Auge, A., Apr. 1982. Apparent thickness and scattering properties of Saturn's rings from March 1980 observations. Astronomy and Astrophysics 108, 296–305.

Smith, B. A., Soderblom, L., Batson, R. M., Bridges, P. M., Inge, J. L., Masursky, H., Shoemaker, E., Beebe, R. F., Boyce, J., Briggs, G., Bunker, A., Collins, S. A., Hansen, C., Johnson, T. V., Mitchell, J. L., Terrile, R. J., Cook, A. F., Cuzzi, J. N., Pollack, J. B., Danielson, G. E., Ingersoll, A. P., Davies, M. E., Hunt, G. E., Morrison, D., Owen, T., Sagan, C., Veverka, J., Strom, R., Suomi, V. E., Jan. 1982. A new look at the Saturn system—The Voyager 2 images. Science 215, 504–537.

Smith, B. A., Soderblom, L., Beebe, R. F., Boyce, J. M., Briggs, G., Bunker, A., Collins, S. A., Hansen, C., Johnson, T. V., Mitchell, J. L., Terrile, R. J., Carr, M. H., Cook, A. F., Cuzzi, J. N., Pollack, J. B., Danielson, G. E., Ingersoll, A. P., Davies, M. E., Hunt, G. E., Masursky, H., Shoemaker, E. M., Morrison, D., Owen, T., Sagan, C., Veverka, J., Strom, R., Suomi, V. E., Apr. 1981. Encounter with Saturn—Voyager 1 imaging science results. Science 212, 163–191.

van de Hulst, H. C., Oct. 1974. The spherical albedo of a planet covered with a homogeneous cloud layer. Astronomy and Astrophysics 35, 209–214.

Verbanac, G., de Pater, I., Showalter, M. R., Lissauer, J. J., Mar. 2005. Keck infrared observations of Saturn's main rings bracketing Earth's August 1995 ring plane crossing. Icarus 174, 241–252.

Veverka, J., Thomas, P., Johnson, T. V., Matson, D., Housen, K., 1986. The physical characteristics of satellite surfaces. In: Burns, J. A., Matthews, M. S. (Eds.), Satellites. Tucson : University of Arizona Press, pp. 342–402.

Zebker, H. A., Marouf, E. A., Tyler, G. L., Dec. 1985. Saturn's rings–Particle size distributions for thin layer model. Icarus 64, 531–548.

Zebker, H. A., Tyler, G. L., Jan. 1984. Thickness of Saturn's rings inferred from Voyager 1 observations of microwave scatter. Science 223, 396–398.